Search for Neutrinos from the Direction of the Galactic Center with the IceCube Neutrino Telescope

Der Fakultät für Mathematik, Informatik und Naturwissenschaften der RWTH Aachen University vorgelegte Dissertation zur Erlangung des akademischen Grades eines Doktors der Naturwissenschaften

von

Diplom-Physiker Jan-Patrick Hülß

aus Wuppertal.

Abstract

The IceCube telescope located at the geographic South Pole is designed to detect neutrinos. Usually, IceCube uses the Earth as shield against the background of atmospheric muon events. This restricts the field of view to the Northern hemisphere. At high energies (PeV scale) the background fades away and the observation of the Southern sky is possible, too. At lower energies, neutrino induced events from the Southern sky can be identified if the interaction vertex is within the detector volume. For the reconstruction and identification of the interaction vertex new algorithms are developed in this thesis. The reconstruction algorithms are based on the spatial distribution of the hits in the detector. These algorithms are utilized for a search for a neutrino signal from the direction of the Galactic Center with IceCube in the 40 string configuration. In this region neutrinos could be produced in interactions of accelerated Cosmic Ray protons or by the annihilation or decay of Dark Matter particles from the Galactic halo. The analysis observes no significant neutrino signal from the direction of the Galactic Center and limits are set to constrain the neutrino flux and the properties of Dark Matter. Finally, an outlook to the full IceCube Detector including DeepCore is presented. It is expected that the sensitivity will increase significantly.

Contents

List of Figures

List of Tables

1 Introduction

Observing Nature and learning about its laws has always fascinated mankind. Curiosity and an exploratory urge have led to today's status of technology and our view of the universe. Beside ancient observations, astronomy got into focus with the work of N. Copernicus (1473-1543), G. Galilei (1564-1642) and J. Kepler (1571-1630). A new epoch of astronomy began after their pioneering observations.
Today optical astronomy is a well established tool for observing extraterrestrial objects. Among others, the position and motion of celestial objects is measured and the spectral analysis of the arriving light is used for further investigations. Moreover, the observations reach deep into the universe and besides stars also galaxies are observed and explored.
In 1912 V. Hess discovered in balloon flights [Hes12] that the amount of ionizing radiation increases with altitude. This radiation is caused by interactions of the so-called 'Cosmic Rays' with the Earth's atmosphere. These discoveries opened a new window to the Universe. During the twentieth century new detection methods were developed to measure the Cosmic Rays and their properties and to learn about their origin. Concurrently, the Standard Model of Particle Physics developed. Both fields contributed to the development of the other. Today we know that the radiation which reaches the Earth from outer space is composed of different stable particles of the Standard Model: the optically visible photons and many other stable particles and nucleons, among them also neutrinos.
The field of Astroparticle Physics investigates all different kinds of Cosmic Ray particles which reach the Earth. This multi messenger approach is important to determine which celestial objects and phenomena are the sources of the Cosmic Rays and to learn about the acceleration mechanism. In addition, it is important to observe the whole energy range from the Cosmic Microwave Background ($10^{-4}\,\mathrm{eV}$) to the GZK Cut-Off ($10^{20}\,\mathrm{eV}$) in order to explore the energy distribution, the composition and the origin of Cosmic Rays.
At the highest energies ($> 10^{18}\,\mathrm{eV}$) the Cosmic Rays are expected to have an extra-galactic origin. Candidate sources are active galactic nuclei or so-called gamma ray bursts. Below $10^{15}\,\mathrm{eV}$ the Cosmic Rays are expected to originate from smaller objects like supernovae, black holes or micro-quasars. These objects can be observed in the Milky Way. Between these energies is a transition region. The lowest energetic Cosmic Rays ($< 10^{10}\,\mathrm{eV}$) originate mostly from the Sun.
Neutrino astronomy concentrates on the neutrinos as 'cosmic messengers'. They traverse the Universe almost unhindered even over large distances: Neutrinos point back to their origin and thus allow the identification of their source. Up to now, extraterrestrial neutrinos have only been observed from the Sun and the supernova 1987A [B^+88],[H^+88],[A^+87a].
At various locations on Earth neutrino detectors have been built. IceCube is a $1\,\mathrm{km}^3$ neutrino detector located at the geographic South Pole. This detector is sensitive to neutrinos with energies above $10^{11}\,\mathrm{eV}$. The basic idea is to observe neutrinos traversing the Earth. No other Standard Model particle can traverse the Earth. Therefore, the primary field of view of the IceCube detector is the Northern Sky. From the Southern Sky muons produced in the atmosphere can reach the detector and cause background events. Their energy spectrum is steeper than the spectrum expected for neutrinos. Thus, the Southern Sky becomes accessible at higher energies, too.
The so-called DeepCore enhancement is built in the lower center of IceCube to improve the sensitivity for the lower energetic neutrino events lowering the threshold to $10\,\mathrm{GeV}$. In

addition, observations of the Southern Sky at lower energies become possible by using the outer parts of IceCube as active veto against Cosmic Ray muons which enter the detector. Neutrino events can pass this veto and start in the central region of the detector. The increased field of view enables IceCube to observe neutrinos from the central region of the Milky Way, where many galactic source candidates are located.
The analysis presented in this work is a first approach to test the detection capabilities of IceCube for neutrinos from the Southern Sky. For this analysis data taken between spring 2008 and summer 2009 are used. At that time DeepCore had not yet been deployed and only half the IceCube detector was available. The recorded data is used to perform a benchmark analysis to test and show the capabilities of the detector and particularly the active veto.
Therefore, new algorithms are developed to reconstruct and identify neutrino induced events. These algorithms are based on the hit topology of detected signals in the detector. As a benchmark source the Galactic Center is chosen. In this region there are several source candidates: e.g. the central super-massive black hole. In addition, this analysis searches for neutrinos from annihilating or decaying Dark Matter particles. Models for the halo of our Galaxy predict a high density of these particles close to the Galactic Center.

2 Neutrino Astronomy

The motivation to use neutrinos as messenger particles for astronomical objects is strongly connected with the wide field of particle astronomy. This scientific branch uses particles hitting the earth from outer space as probes of physical processes in the high energy universe. These so called cosmic rays were first observed by V. Hess in 1912 [Hes12]. Even with today's detection techniques, the origin of these cosmic rays remains mostly unknown: neither the sources nor the production mechanism are known. Common theories explaining the origin of cosmic rays also predict neutrinos from these sources.
This chapter begins with an overview on cosmic ray astronomy and discusses possible sources of cosmic rays focusing on neutrino production. The acceleration of charged particles in sources is discussed as well as the production of neutrinos in the annihilation of massive particles, e.g. remnants from the big bang.

2.1 Cosmic Rays

In 1912 V. Hess discovered during balloon flights that radiation increases with altitude [Hes12]. He concluded that this radiation originates from particles hitting the atmosphere from outer space, so-called cosmic rays. This discovery initiated a long period of measuring and investigating the new particles. Now, almost 100 years after the first discovery, several questions are answered but many others are still open.
The investigation of the cosmic rays led to discoveries of several new particles (e.g. [And33]) and contributed to our understanding of the Standard Model of particle physics. In addition to the gained knowledge in particle physics also the origin of cosmic rays is of interest. Over the last decades several experiments measured the energy distribution and the composition of the particles arriving at the Earth. Today, the energy spectrum is known from about $10^9\,\mathrm{eV}$ up to about $10^{20}\,\mathrm{eV}$ (figure 1). It is well described by a power law $dN/dE \propto E^{-\gamma}$ with small changes in the spectral index γ. At the so called knee ($\sim 3 \cdot 10^{15}\,\mathrm{eV}$) the spectral index γ steepens from about 2.7 below to about 3 above; at the ankle ($\sim 3 \cdot 10^{18}\,\mathrm{eV}$) it flattens again.
At low energies about 90% of the cosmic rays are protons, about 9% are helium nuclei and about 1% are electrons. Heavier nuclei are laso found in small fractions. The composition differs with the particle energy. The total amount of particles is dominated by the low energetic cosmic rays due to the steep decrease of the flux with energy.
The changes in the energy spectrum and the composition of the cosmic rays are believed to be generated by a change of the sources. Up to $10^{10}\,\mathrm{eV}$ the cosmic rays originate from the sun. The solar wind shields off other contributions. Above this energy and up to a value of $3 \cdot 10^{15}\,\mathrm{eV}$ (knee) the dominant component is likely to originate from galactic sources. The shape of the energy spectrum at the knee is determined by the cut-off energies which depend on the charge of the accelerated particles. In this energy range the composition changes towards heavier elements. At the highest energies, the particles are believed to have an extra-galactic origin. The Pierre Auger experiment found a correlation with the nearby active galactic nuclei [Pie07] and supports this prediction.
Above about $5 \cdot 10^{19}\,\mathrm{eV}$ the so called GZK cut-off is predicted [ZK66][Gre66]. Protons at these energies interact with the cosmic microwave background producing a Δ^+ resonance. This resonance mostly decays into a pion and a nucleon. If the nucleon is a proton, it has

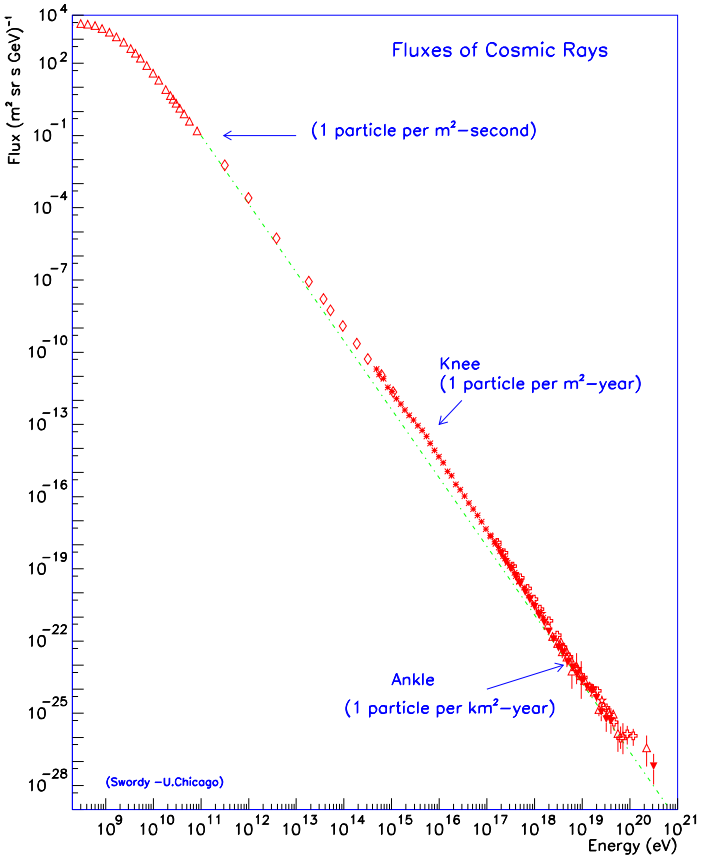

Figure 1: Energy spectrum of the cosmic rays arriving at the Earth. Figure from [CGS97]

less energy than the initial proton. Thus the flux of protons at the resonance energy is reduced. Similar resonances exist for the heavier elements of the cosmic rays. A reduction of the cosmic ray flux at about this energy is observed [Pie08]. This observed cut-off can be explained by other effects than the GZK effect, too: for example a maximum acceleration energy.

When a Comic Ray hits the Earth it interacts with a nucleus of the atmosphere. This interaction produces high energetic particles inducing new interactions and creating a so called air shower of secondary particles. This air shower has several components: a hadronic, a muonic and an electromagnetic component. The hadronic component is created from the remnants of the target nuclei and the initial particle. It usually contains a large fraction of charged and uncharged pions, but also heavier mesons and baryons. The muons are created in the decay of charged pions ($\pi^{\pm} \rightarrow \mu^{\pm} + \nu_{\mu^{\pm}}$) and kaons ($K^{\pm} \rightarrow \mu^{\pm} + \nu_{\mu^{\pm}}$). The electromagnetic component is induced by gammas from radiation losses and from the decay of the neutral pion $\pi^0 \rightarrow \gamma + \gamma$. By pair production of electrons it develops further into an electromagnetic cascade (Heitler model [Hei44]).

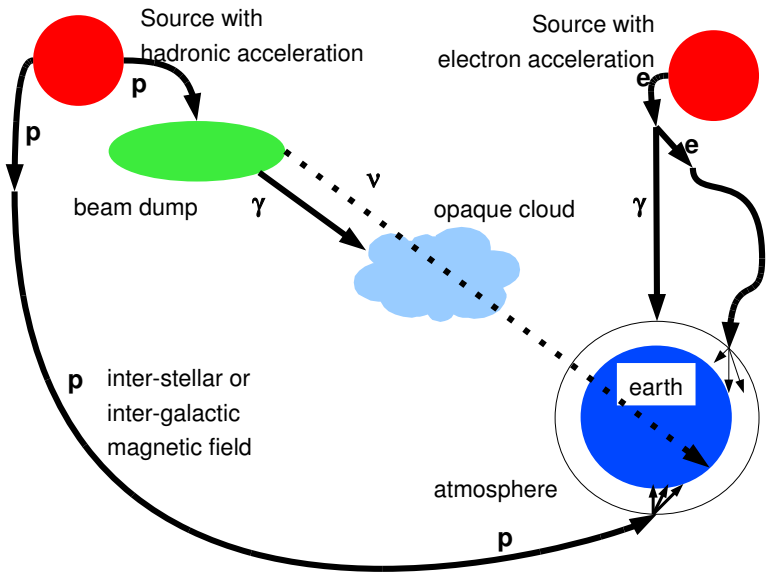

Figure 2: Sources of cosmic rays and the observation on Earth. Two different scenarios are considered: the acceleration of hadrons or the acceleration of electrons.

All components propagate through the atmosphere towards the ground. The covered atmospheric depth depends on the energy of the primary cosmic ray and on the component of the cascade. If the primary particle is low energetic, the electromagnetic and hadronic cascade thin out before reaching the ground. Many of the muons can still reach ground due to their small energy loss and the large life time. Due to the small interaction cross section of neutrinos almost all reach the ground and travel trough the Earth.

2.2 Multi Messenger Astronomy

Detecting cosmic rays it not sufficient to identify the sources of cosmic rays and to understand the interior processes at these sources. Due to inter-stellar or inter-galactic magnetic fields only cosmic rays of ultra high energies can be traced back to their origin, if it is nearby. The detection of other messenger particles can be used to identify individual sources and to investigate the acceleration mechanisms.

Figure 2 shows two kinds of sources: acceleration protons or electrons. Both particles are charged and they are deflected on their way to the earth. Additional messengers are produced by interactions of these initial particles. Electrons can produce high energetic photons by Bremsstrahlung or inverse Compton scattering with the background radiation. Protons interact with matter near the source producing pions. These decay either into photons or neutrinos. Photons and neutrinos are neutral and thus they are not deflected by the magnetic fields on their way to the earth. They point back to their sources. Therefore, photons and neutrinos can be used to identify candidate sources for the production of high energy particles.

Unfortunately, photons are shielded by matter between the source and the Earth. Low energetic photons get absorbed while high energetic photons are lost due to pair production in the vicinity of nuclei. It is thus not possible to look behind these objects at all, or the field of view is limited to certain energy ranges. Even precise measurements of the photon energy spectrum as done by HESS are not sufficient to clearly distinguish between leptonic and hadronic scenarios.
Messenger neutrinos with reasonably high energy are only produced in hadronic interactions. No neutrinos are expected in electromagnetic processes where electrons are accelerated to high energies. Thus, detected neutrinos would be clearly indicate proton acceleration. As already mentioned, neutrinos travel through the universe unhindered due to their small interaction cross section. The small cross section also complicates the detection. Up to now, no neutrinos from cosmological sources have been observed. However, this does not contradict the expectations for a hadronic acceleration.

2.3 Sources for Cosmic Rays, Photons and Neutrinos

Cosmic rays, photons and neutrinos are expected to emerge from a large variety of sources. These can be explained by two models: One, the bottom-up model, is based on the acceleration of charged particles to high energies. These particles can produce neutrinos and photons in further interactions. The acceleration mechanisms are discussed in section 2.3.1 and section 2.3.2.
In contrary heavy remnant particles from the big bang may decay or annihilate and produce neutrinos, photons and other particles as decay products. These top-down models are discussed in section 2.4.

2.3.1 Acceleration in Electromagnetic Fields

Charged particles can be accelerated by electric fields. In order to accelerate the Cosmic Rays a large electric field is needed. In order to explain such large fields, the models focus on rotating magnetized neutron stars, called pulsars [Mic84] or on accretion discs around black holes, that are threaded by magnetic fields [Ost02]. The particles are accelerated to energies up to 10^{15} eV.
However, most models do not reproduce the observed power law spectrum and they can not explain particles accelerated up to 10^{20} eV. Either the fields are not strong enough to accelerate particles up to 10^{20} eV (pulsars, stellar black holes) or the objects are shielded by dense pair plasma and intense radiation which would cause energy losses. For example the Crab nebula might accelerate protons up to energies of 10^{18} eV. Due to pair production in the electromagnetic field the potential should be even smaller.

2.3.2 Fermi Acceleration

The acceleration of cosmic rays can be understood by the Fermi mechanism [Fer49][Gai90]. Fermi acceleration is based on a step-wise energy transfer by scattering at inhomogeneous magnetic fields. The fields are induced by partly ionized gas clouds or shock fronts driven by plasma instabilities. Each particle has to go through numerous subsequent encounters to reach the highest energies.

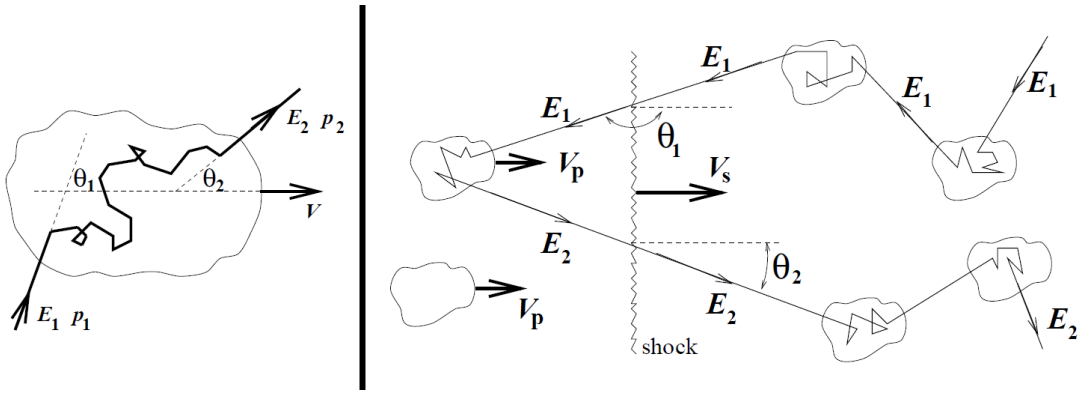

Figure 3: Fermi-acceleration. Left: Interaction of a particle of energy E_1 with a cloud of magnetic fields moving with speed V. Right: Interaction of a cosmic ray of energy E_1 with a shock moving with speed V_s [Pro96].

An ionized cloud is expected to have a velocity, which is small compared to the speed of light: $\beta_c = v_c/c < 10^{-4}$. A high energetic charged particle scatters elastically in the magnetic fields inside the gas cloud (figure 3, left). In a reference system which is not moving with the cloud the particle looses or gains energy depending on whether it is a head-on or a tail-on collision.
Calculating the energy in the rest frame of the cloud leads to

$$E_1' = \gamma E_1(1 - \beta_c \cos\theta_1) \; . \tag{1}$$

The prime marks that the energy is in the rest frame of the cloud, E_1 is the energy before the encounter and θ_1 the entry angle. In the rest frame of the cloud the particle energy is not changed: $E_1' = E_2'$. After the encounter the particle leaves the cloud at an angle θ_2 with the energy

$$E_2 = \gamma E_2'(1 + \beta_c \cos\theta_2') = \gamma E_1'(1 + \beta_c \cos\theta_2') \; . \tag{2}$$

Combining equation 1 and equation 2 the relative energy change in the reference frame is given by

$$\begin{aligned} \frac{\Delta E}{E} &= \frac{E_2 - E_1}{E_1} \\ &= \gamma^2(1 - \beta_c \cos\theta_1)(1 + \beta_c \cos\theta_2') - 1 \; . \end{aligned} \tag{3}$$

In order to determine the expectation value for the energy change, the expectation values for the angles are required. Assuming no preferred exit angle for the particle in the cloud's rest frame and an initial isotropic distribution of particles, the expectation value for the energy change per encounter is:

$$\epsilon = \left\langle \frac{\Delta E}{E} \right\rangle = \frac{1 + \beta_c^2/3}{1 - \beta_c^2} - 1 \approx \frac{4}{3}\beta_c^2 \; . \tag{4}$$

On average, a particle gains energy when scattering at the magnetic field of a cloud. The relative additional energy is proportional to $\beta_c^2 < 10^{-8}$. This is called "Second Order

Fermi acceleration". Here, the particle gains only a small amount ΔE of energy. In fact, the second order Fermi-acceleration is too inefficient to produce high energetic protons on reasonable time scales.
A more efficient model is the so-called "First Order Fermi acceleration". It appears with shocks. Shock waves are for instance generated when a supernova ejects material into the surrounding interstellar matter at supersonic speed. The speed is about $v_s = 10^4$ km/s. At the shock front the interstellar matter is compressed together with the inherent magnetic fields. Here, the acceleration has always the same direction due to the fixed propagation direction of the shock front. The energy transfer is calculated similarly as above for the second order Fermi acceleration. The mean change of the energy is

$$\epsilon = \left\langle \frac{\Delta E}{E} \right\rangle \approx \frac{4}{3}\beta_s \ , \qquad \beta_s = \frac{v_s}{c} \ . \tag{5}$$

Compared to the second order Fermi acceleration, this mechanism is thus more effective. Relativistic velocities of the shock fronts substantially change this picture. The Lorentz boost deforms the angular distribution of the particles, and it is not isotropic in the upstream and in the downstream rest frame. The angular dependence of the distribution function has to be computed explicitly. In the upstream region the particle quickly encounters the shock front again. This allows to obtain larger maximum energies for acceleration and opens up the possibility to explain cosmic rays up to 10^{20} eV. Relativistic shocks are investigated in the context of jets from Active Galactic Nuclei [Ino07][RB93] or Gamma Ray Bursts [Dar05].
Each particle passes the shock front more than once. After n interactions the mean energy of these particles is

$$E_n = E_0(1+\epsilon)^n \ . \tag{6}$$

E_0 is the initial energy. The number of interactions is estimated by the probability p of the particle to leave the area of the shock front. This probability depends on the properties of the shock fronts, the geometry, the thermodynamic parameters and on the energy of the particle. For more information see [Pro98],[Gai90].
The probability for n interactions is $(1-p)^n$. To reach an energy E,

$$n_0 = \frac{\ln(E/E_0)}{\ln(1+\epsilon)} \tag{7}$$

encounters are required. The number $N(>E)$ of particles with an energy greater than E is:

$$\begin{aligned} N(>E) &= \frac{(1-p)^{n_0}}{p} \propto \frac{1}{p}\left(\frac{E}{E_0}\right)^{-\gamma} \ , \\ \gamma &= \frac{\ln(1/(1-p))}{\ln(1+\epsilon)} \ . \end{aligned} \tag{8}$$

This is a power law energy spectrum as it is observed for cosmic rays. The spectral power index γ is not universal, but it depends on details of the shock fronts. For a mono-atomic gas γ is calculated to be $2+\delta_0$ (δ_0 is a small positive number). The observed spectrum of cosmic rays at the Earth is steeper than this spectrum. This can be understood by the energy dependent diffusion in the galaxy.

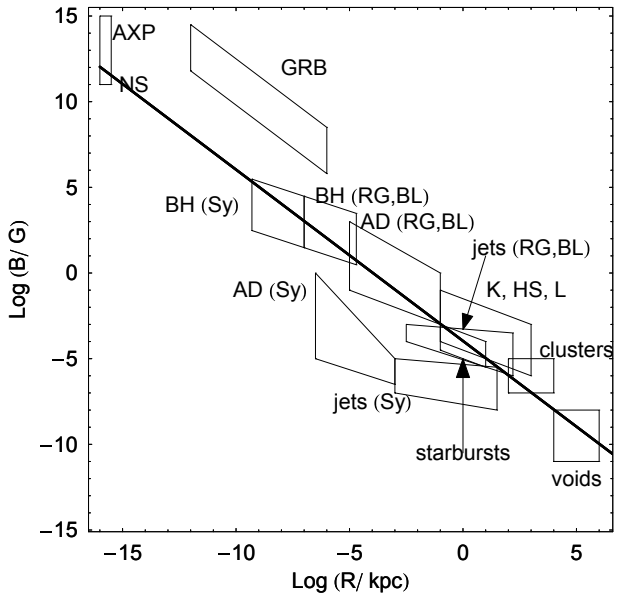

Figure 4: Hillas plot with constraints from geometry and radiation losses for 10^2 EeV protons. The thick line represents the lower boundary of the area allowed by the Hillas criterion. Boxes denote parameter regions for possible sources of the high energetic cosmic rays. These are: neutron stars (NS) and anomalous pulsars (AXP); super-massive Black Holes (BH); central regions (AD) of active galaxies (Seyfert (Sy) and radio galaxies (RG) and blazars (BL)); relativistic jets, knots (K), hot spots (HS) and lobes (L) of powerful active galaxies (RG and BL); non-relativistic jets of Seyfert galaxies (Sy); starburst galaxies; gamma-ray-bursts (GRB); galaxy clusters and intergalaxy voids. Modified figure from [PT08].

A common simplified model of the propagation is the leaky box model [BP86]. It assumes particles propagating freely in a given volume, for example the Galaxy. At the boundaries of the volume they have an energy dependent probability to escape to the outer space. The escape time, T_{esc} is related to the escape length λ_{esc} via $\lambda_{\mathrm{esc}} \propto \rho\beta c T_{\mathrm{esc}}$ (ρ is the density and c the speed of light). This model predicts a steepening of the energy spectrum during the propagation from the source to the observer. An additional small value δ is introduced to quantify the effect. The spectrum steepens to $E^{-2-\delta_0-\delta}$. δ is found to be about 0.6. The observed spectrum is therefore in good agreement with the prediction from Fermi acceleration.

For secondary neutrinos the energy spectrum does not steepen during the propagation due to rare interactions. They propagate almost unhindered. Neutrinos travel trough the galaxy independently of their energy. For neutrinos the initial hard $\gamma \sim 2 + \delta_0$ spectrum is expected.

2.3.3 Candidate Sources for the Acceleration of Charged Particles

A source accelerating particles via the Fermi mechanism can only reach a certain maximum energy depending on the source properties. A basic criterion which determines the maximum energy is that the Larmor radius of a particle does not exceed the accelerator

size, otherwise the particle escapes the accelerator and cannot further gain energy. This so called Hillas criterion can be formulated as follows

$$E < E_H = \beta_s Z \frac{B}{\mu\mathrm{G}} \frac{R}{\mathrm{kpc}} \cdot 10^{18}\,\mathrm{eV}\ , \tag{9}$$

where E is the energy gained by a particle with charge Z and shock velocity β_s in a region of size R with the magnetic field B [PT08]. The energy maximum is further constrained by radiation losses:

- **Synchrotron radiation loss** : When a charged particle is accelerated, it emits synchrotron photons. The size of the acceleration region has to be large enough to make energy loss due to synchrotron radiation negligible. The energy loss is proportional to E^4/R^2, which yields the general trend (using equation 9)

$$-\frac{dE_{\mathrm{sync}}}{dt} \propto B^2 E^2\ . \tag{10}$$

- **Photo-pion production** : The acceleration region should be smaller than the interaction length of the particle for photon-pion production with the local radiation field around the source. The energy loss is about constant

$$-\frac{dE_{\mathrm{pion}}}{dt} \sim \mathrm{constant}\ . \tag{11}$$

Figure 4 shows the capabilities of various objects in the universe to accelerate protons up to a certain energy. Candidate sources for the acceleration of high energetic protons (10^2 EeV) are active galactic nuclei (AGN) and gamma-ray-bursts (GRB). If these sources accelerate hadrons, they later interact with the surrounding interstellar matter or gas clouds. These interactions produce charged pions, which in turn decay into muons and neutrinos. The energy of the neutrinos is a fraction of their parent hadrons. Therefore all these source classes are possible neutrino sources for energies up to the order of 1 EeV.
If, instead of hadrons, leptons are accelerated, dominantly photons and electrons are produced due to Bremsstrahlung and inverse Compton scattering.
To take a maximum possible energy into account, the energy spectrum (equation 8) is modified to

$$\frac{dN}{dE} \propto E^{-\gamma} \exp\left(-\frac{E}{E_{\mathrm{cut}}}\right)\ . \tag{12}$$

Here, an exponential cut-off at E_{cut} is added, which represents the capabilities of the source.

2.3.4 Galactic Sources

All above discussed sources for cosmic rays and neutrinos are extra-galactic objects. In addition, also galactic objects can accelerate hadrons. The expected maximum energies are lower (PeV scale) and so are the energies of produced neutrinos. The advantage for an observation of these sources is the relatively small distance to the Earth. Sources with much weaker fluxes can be detected. Possible sources are:

- **Supernova Remnants** : A supernova occurs if the fusion in a massive star ends. Without the thermal power released by the fusion the gravitational force is no longer compensated by radiation pressure. The core of the star collapses into a neutron star or into a black hole, thus compressing protons and electrons to neutrons by inverse β-decay. This process produces electron-neutrinos. A region of high energy density is accumulated and only neutrinos can leave. 99% of the energy is emitted by thermal neutrinos. Their mean energy is 10 MeV.

  During the collapse the outer part of the shell is blown away with a speed above the sonic velocity of the surrounding interstellar medium. A shock front for Fermi-acceleration develops. These shock fronts may accelerate charged particles up to energies of about 100 TeV [Gai90]. The energy spectrum of the cosmic rays below the knee can be explained by supernova remnants.

- **Young Supernova Shells** : In young supernova shells particles can be accelerated by two different mechanisms: either pulsar acceleration [Sta90] or acceleration by interactions of the supernova shock with the circum-stellar medium [BP89].

  Pulsars appear only in core-collapse supernovas. The pulsar liberates rotational energy. It is used to accelerate particles via magnetic dipole radiation. Acceleration of particles by low frequency magnetic dipole radiation is highly efficient. The acceleration to relativistic velocities happens in times which are very short compared to the period of the dipole wave and the particle effectively sees a static field. For the Crab pulsar the maximum proton energy is estimated to be $1.6 \cdot 10^{15}$ eV [GO69].

  Stars with masses larger than about 15 solar masses become red super-giants or Wolf-Rayet stars. These have strong stellar winds, carrying away stellar material. A circum-stellar shell forms around the star. The supernova shock propagates into this shell with a velocity larger than the velocity of sound and continues as shock wave. A second shock is formed, decelerating material from the supernova's envelope. A thin (compared to the radius) shell of shocked matter between the inner and outer shock is formed. Gas from the envelope and the circum-stellar medium is flowing in. Repeated particle crossing of the two shocks leads to an effective particle acceleration up to energies of [BP88]

$$E_{\max} \leq 10^5 \left(\frac{B}{3 \cdot 10^{-3}\,\mathrm{G}} \right) \left(\frac{R}{10^{16}\,\mathrm{cm}} \right) \mathrm{GeV} \,. \tag{13}$$

  Above this energy a flat $dN/dE \propto E^{-1}$ tail is attached, which cuts off sharply at $E \approx 5E_{\max}$.

- **Micro-quasars** : The gravitational object in the center of a micro-quasar is supposed to be a neutron star or a black hole of about 10 solar masses. Additionally, jets and an accretion discs are observed. Micro-quasars are binary systems. The material, which is necessary to build the disc, originates from a companion star. The size of the accretion disc of a micro-quasar is about 10^{13} km and the length of a jet is several light years. Depending on the mass accretion more or less radiation originates from a micro-quasar. These variations are on the time scale of days [Mir02].

The jets of micro quasars are candidates for sources of high energetic neutrinos. They contain collimated magnetized plasma at relativistic speed. Micro-quasars could contribute to the galactic component of the cosmic ray spectrum up to several TeV [Luc74][Cha06].

- **Wind- and shock-acceleration around rotating neutron stars** : Pulsars have been discussed as galactic sources of the cosmic rays. These objects begin their lives as fast rotating neutron star ($\omega \approx 3000\,\mathrm{Hz}$) with large magnetic fields ($B_{\mathrm{NS}} > 10^{13}\,\mathrm{G}$)[BEO00]. Inside the light cylinder a magnetosphere of density

$$n(r) \sim \frac{B(r)\omega}{4\pi Zec} \tag{14}$$

co-rotates with a magnetic dipole field component scaling with $B(r) \sim B_{\mathrm{NS}}(r_{\mathrm{NS}}/r)^3$. Here r is the radius in the light cylinder, e.g. $r < c/\omega$ and r_{NS} the radius of the neutron star. With increasing distance from the neutron star surface the dipole field cannot be maintained and beyond the light cylinder a mostly azimuthal field can be assumed. Thus, one expects that from the light cylinder a relativistic plasma expands as magneto-hydrodynamic wind with Alfvén speed. As the neutron star is produced in a supernova one considers the surface of the young neutron star as enriched with elements up to the iron peak. These ions can strip off and be shock-accelerated in the winds to maximum energies of [BEO00]

$$E_{\mathrm{max}} \sim 8 \cdot 10^{20} \left(\frac{Z}{26}\right) \left(\frac{B_{\mathrm{NS}}}{10^{13}\,\mathrm{G}}\right) \left(\frac{\omega}{3000\,\mathrm{Hz}}\right)^2 \mathrm{eV}\,. \tag{15}$$

- **Strong electric field acceleration in rotating neutron stars** : The rotating magnetosphere of neutron stars is expected to induce a strong electric field of the order of $c^{-1}|(\Omega \times R) \times B|$. Here R is the stellar radius of the neutron star, B the field-strength and Ω the opening angle of the light cone. This leads to a potential of the order of [Ost02]

$$\Delta\phi \sim 10^{20} \left(\frac{B}{10^{13}\,\mathrm{G}}\right) \left(\frac{R}{10^{6}\,\mathrm{cm}}\right)^2 \left(\frac{\omega}{1000\,\mathrm{Hz}}\right) \mathrm{V}\,. \tag{16}$$

This potential looks promising to accelerate particles to highest energies. Nevertheless due to pair production in the pulsar's magnetosphere, the e^+e^- pairs shorten the circuit and reduce the effective voltage by a few orders of magnitude.

Sources already discovered by observing high energy photons are good candidates to also produce neutrinos. In case of Fermi acceleration, photons and neutrinos are produced in decays of secondary neutral and charged pions respectively. Due to the same origin the expected fluxes are correlated.
During the last years the HESS experiment and the Milagro experiment did an extensive scan for TeV γ-ray sources in the Galactic Plane [HES05a][Cha09][A$^+$07]. Within the Galactic Plane a large number of TeV γ-ray sources exist, some connected with objects known before, some new discoveries. These sources have different sizes: they vary from spots of less than 0.1° to extended sources of about 2°. Also the individual energy spectra differ. The spectral indices γ vary between about 1 and 3. For many sources a pure power

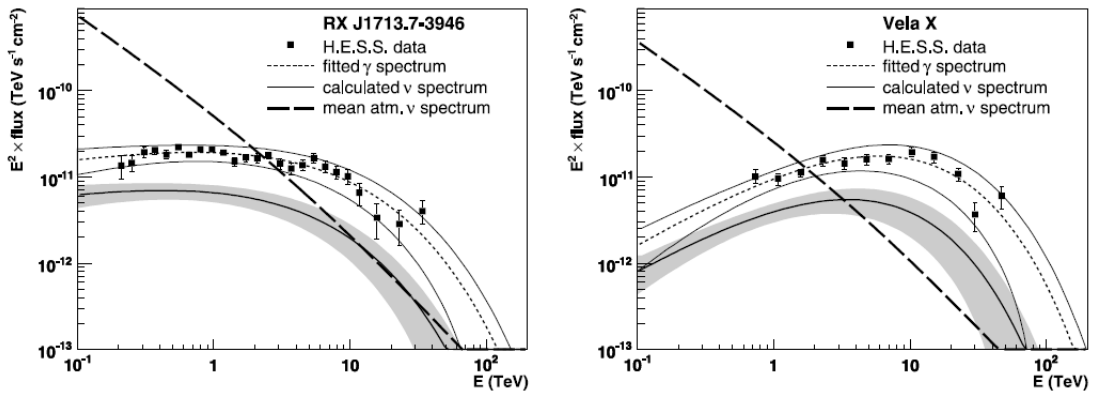

Figure 5: Example γ-ray and neutrino fluxes for two galactic sources (left: RX J1713.7-3946, right: Vela X) from [KHSA07]. Shown is the γ-ray measurement by HESS (squares), a fitted power law energy spectrum (dotted line and solid error lines) and the resulting neutrino spectrum (solid line with gray shaded errors). For both spectra, the errors show only statistical uncertainties. The data is compared to the flux expected from neutrinos produced in air showers (dashed line).

law fits the observations best, and an eventual cut-off energy is above the observation range. If a cut-off is observed in the energy spectrum, it is included in the fit: the values range from about 100 GeV to 10 TeV. Thus, the observed energy spectra of individual sources differ significantly due to source properties [Cha09].

Several assumptions have to be made to convert these observations into expectations for a neutrino flux . In addition to the same production mechanism, also source properties like the surrounding matter and radiation density or the magnetic field have to be considered. Based on a unified set of assumptions the expected neutrino flux of several TeV γ-ray sources is determined in [KHSA07]. The expected neutrino flux is about 20% to 40% of the γ-ray flux depending on the spectral index. The cut-off energies are reduced to about 60% with respect to the cut-off energies for γ-rays. Due to the correlation in neutrino and γ-ray production, a similar variety as observed in the γ-ray energy spectra is expected in the neutrino spectra. The strongest sources produce a neutrino flux above several TeV, which is larger or equal compared to the one from cosmic rays hitting the Earth's atmosphere. Figure 5 shows examples for γ-ray and associated neutrino spectra.

According to these results the search for neutrinos from sources in the Galactic Plane is promising. The largest excess is expected for neutrinos between several TeV and about 100 TeV.

A measurement or limitation of the neutrino flux from these sources allows conclusions on the source properties and on the production mechanism. For example a lower neutrino flux could appear due to an additional production of TeV γ-rays via electromagnetic processes, while a higher neutrino flux might be caused by absorption of γ-rays in an opaque medium.

2.3.5 The Galactic Center Region

The central region of our Galaxy is of special interest. It was investigated by various experiments measuring photons of different energies. This region has the highest density

of matter in the Galaxy and it includes the central Black Hole as well as several TeV γ-ray sources [MS96].
The central Black Hole has a mass of $4.31 \pm 0.06|_{\text{stat}} \pm 0.36|_{\text{sys}} \cdot 10^6 \cdot M_{\text{sun}}$ and is classified as Super Massive Black Hole [G$^+$09]. Compared to masses of central Black Holes in other galaxies (masses up to $10^9 M_{\text{sun}}$) this is a small mass, though. No evidence of jets has been observed and the Black Hole is no so called active nucleus. Compared to other galactic nuclei (e.g. the Andromeda Galaxy at a distance of about 800 kpc) the Galactic Center with a distance of about 8 kpc is relatively close. Therefore, a luminosity, which is a factor of 10^4 smaller, could lead to a similar flux at the Earth.
HESS has observed a γ-ray source (J1745-290) in the direction of the central Black Hole. This emission might originate from the Black Hole or the Pulsar Wind Nebula G359.95-0.04 [HES09a]. The angular distance between these objects is smaller than the resolution of the telescope. As discussed in the previous section, an expectation for the neutrino flux can be derived from the γ-ray flux. The resulting flux is similar to that of the neutrinos produced by air showers in the atmosphere above 5 TeV. A circular search bin for the neutrino observation with a radius $\sim 0.3^\circ$ around the source is assumed [KHSA07].
In addition, there are three other γ-ray sources seen by HESS within 2° distance from the center of the Galaxy [Cha09]. The source J1747-281 is at the same position with a supernova remnant G 0.9+0.1 [HES05b]. The source J1745-303 has no clear counterpart but is observed with a very hard energy spectrum $\gamma \approx 1.8$ and no cut-off energy [HES06c][HES10]. The third one is a very faint source J1741-302 at the lower edge of the HESS sensitivity [Tib09].
The two more powerful sources are also discussed in [KHSA07] as neutrino source candidates. The unidentified source (J1745-303) could produce a large neutrino flux compared to the atmospheric expectation at neutrino energies above 5 TeV (search bin with radius $\sim 0.3^\circ$), caused by the hard spectrum. From the supernova remnant G 0.9+0.1 a neutrino flux lower than the flux from the atmosphere is expected in the whole energy range.
The region of the Galactic Center is a good candidate to search for neutrino emission, in particular because of the existence of at least three different source candidates. A drawback would be, that the individual source can not be identified due to small angular deviations.

2.4 Neutrinos from Dark Matter Halos

A candidate for heavy remnant particles is predicted by the astroparticle evidence of Dark Matter. Its existence is derived from various astronomical observations: Cosmic microwave background, structure formation, gravitational lensing, rotation curves of stars in galaxies and others (section 2.4.1). The Dark Matter is expected to consist of non standard model particles (section 2.4.2). These particles either annihilate or decay into standard model particles and thus can be detected.

2.4.1 Evidence for Dark Matter

Various observations confirm the existence of Dark Matter. This section lists the most prominent evidences.
Most important is the investigation of the Cosmic Microwave Background (CMB) by WMAP [H$^+$08]. The power spectrum of the anisotropies depends on the cosmological pa-

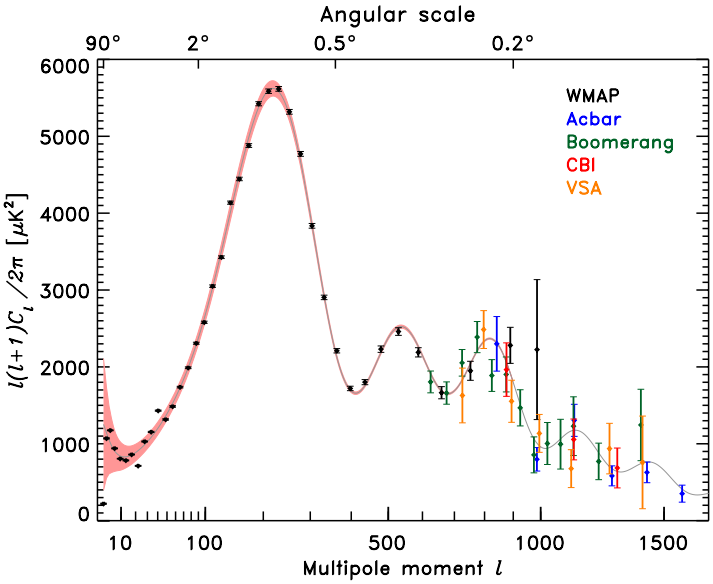

Figure 6: The WMAP three-year power spectrum (in black) compared to other recent measurements of the CMB angular power spectrum, including Boomerang [J$^+$06], Acbar [K$^+$04], CBI [R$^+$04], and VSA [D$^+$04]. For clarity, the $l < 600$ data from Boomerang and VSA are omitted; as the measurements are consistent with WMAP. Figure from [H$^+$07].

rameters, in particular on the amount of non barionic matter. Figure 6 shows the measurements of the power spectrum. The best fitting cosmological parameters are determined assuming the Λ-Cold-Dark-Matter (ΛCDM) cosmological model [Lid03]. This is the present standard model of big bang cosmology. It includes Dark Energy as well as Dark Matter components. The fit results in a Cold Dark Matter density of $\Omega_{\mathrm{cdm}}h^2 = 0.1099 \pm 0.0062$ [D$^+$08]. Even more precise results are achieved in combination with measurements from Type Ia supernovae and Baryon Acoustic Oscillations [K$^+$08]:

$$\Omega_{\mathrm{cdm}}h^2 = 0.1131 \pm 0.0034 \tag{17}$$

In the ΛCDM cosmological model the amount of Cold Dark Matter is about $(22.8 \pm 1.3)\%$ [K$^+$08] of the total energy density of the universe.
In addition to the CMB requiring Dark Matter, also the structures which we observe in the universe indicate the existence of Dark Matter. The observed structures of galaxy-clusters and voids are believed to be formed from primordial density fluctuations. These fluctuations grew over time due to gravitational interactions. Thus, the resulting structures depend on the amount of mass available in these processes and the development of the universe. The structure formation is tested in simulations [Ber98][SFW06]. More cold Dark Matter than observed matter is required to build up the observed structures in the time since the big bang.
In addition, there are also indications for Dark Matter from direct astronomical observations: gravitational lensing, gravitational interactions of galaxy clusters and galaxy rota-

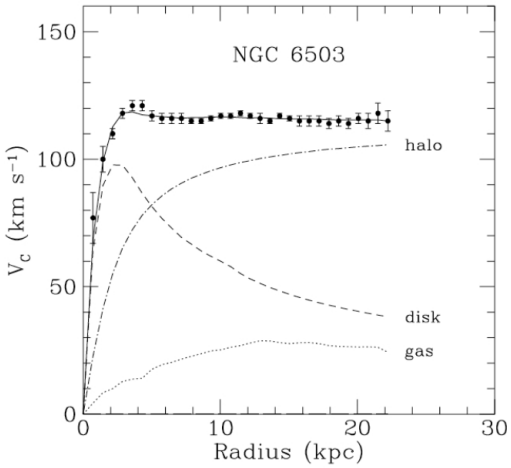

Figure 7: Example rotation curve. The data points with error bars are the observed velocities. The contribution to the rotation curve by the disk stars (dashed line) and by the gas (dotted line) are also shown. The rest is attributed to a Dark Matter halo. Figure from [Kam98]

tion curves. These phenomena, which are discussed in the following, describe observations predicting huge masses in places with no visible matter.
Gravitational lensing appears when an object with huge mass deforms spacetime. Light from a bright object behind the massive object reaches an observer on several paths, and the bright object appears at several positions [Ein36]. In the ideal case of point-like objects a ring would be visible (sometimes called Einstein Ring). Usually, the lensing effect is much weaker and only an increase in brightness is observed. The mass of the lens can be determined. This mass is usually found to be much larger than expected from the visible mass in that region. The difference is believed to consist of Dark Matter.
The rotation curves of galaxies describe the rotation velocity of the stars around the center of the galaxy in dependence of the distance between the stars and the center of the galaxy. This speed is a direct measure of the mass enclosed by the stars orbit. In general, a decrease in velocity is expected with increasing distance to the center, as shown by example in figure 7. Instead, almost constant velocities are observed [MPF96], [BS01]. The same observation is also made for the Milky Way [FBS89]. Here, the observation is more complicated due to our position inside the galactic disk. The only explanation for large velocities together with still gravitationally bound stars is a larger enclosed mass. A possible explanation is Dark Matter in a spherical halo around the galaxies. Models for the Dark Matter distribution in these halos are discussed in section 2.4.4.

2.4.2 Particle Physics Indications for Dark Matter

The previous section discussed evidences for Dark Matter by astronomical observations. The particle content of the Dark Matter, however, is unknown. Only some basic properties are required: to explain the WMAP measurements and the structure formation a certain relic density, the stability on cosmological time scales and a non-relativistic velocity (Cold Dark Matter) is required. The particles are massive and non luminous. Usually, they

are expected to interact only via the weak force. Within the Standard Model no particle fulfills these requirements. Massive neutrinos are the only candidate but their mass is to small. They would move with relativistic velocities and contribute to Hot Dark Matter.
One candidate for this particle is a weakly interacting massive particle (WIMP), usually denoted χ. The mass of this hypothetical particle is roughly between 10 GeV and several TeV. Assuming that these particles were in thermal and chemical equilibrium with the Standard Model particles after inflation, their present relic density is expressed by [KT90]

$$\begin{aligned} \Omega_\chi h^2 &\approx const. \cdot \frac{T_0^3}{M_{\mathrm{Pl}} < \sigma_A \cdot v >} \\ &\approx \frac{0.1pb \cdot c}{< \sigma_A \cdot v >} \end{aligned} \tag{18}$$

T_0 is the current temperature of the Cosmic Microwave Background, M_{Pl} the Planck mass and $< \sigma_A \cdot v >$ the average cross section for self annihilation into Standard Model particles times v, the particle velocity. For a relative density of non-baryonic Dark Matter of $\Omega h^2 = 0.106 \pm 0.008$ [S$^+$07] a typical self annihilation cross section is $< \sigma_A \cdot v > \approx 3 \cdot 10^{-26}\,\mathrm{cm^3 s^{-1}}$. This is referred to as natural scale.
A well motivated WIMP candidate is the lightest particle from super-symmetric models. These predict an additional particle for each particle known in the Standard Model. Each fermion gets a bosonic partner and vice versa. These new particles are heavier than the Standard Model particles; otherwise they would have been detected already.
Super-symmetric particles with masses at the TeV scale can solve the hierarchy problem. Neutralinos are the mass eigenstates of the super symmetric partners of the electro-weak gauge bosons and the Higgs bosons. The lightest of these four eigenstates is stable and a good WIMP candidate, if R-parity is conserved. Within the current super-symmetric theory the properties of these lightest particles are not precisely predicted. They depend on the exact realization of the theory. Important quantities like annihilation products and mass remain undetermined.
Another viable candidate is motivated by theories of universal extra-dimensions. The Kaluza-Klein (KK) theory [Duf94] aims at the unification of gravitation and electromagnetism. Compactified extra-dimension result in a set of massive eigenstates. The ground state is a stable particle due to KK momentum conservation and thus a good Dark Matter candidate. This extension of the Standard Model has less free parameters than the super-symmetric models and the predictions for the KK particle are more precise. The mass is expected to lie between 500 GeV and 1500 GeV [ACD01]. The branching ratios for Standard Model particles produced in annihilations are predicted as shown in table 1. This allows to determine the particles expected in an experiment even though the absolute cross section for annihilations is unknown.
These are two candidate theories which are capable to explain the content and properties of Dark Matter. Both predict stable Dark Matter particles which annihilate into Standard Model particles. A different type of theories predict unstable particles as Dark Matter candidates. The lifetime τ of these particles has to be roughly at the scale of $\tau \gtrsim 1/(< \sigma_A v > \cdot \rho_{\mathrm{DM}}) \sim 10^{26}\,\mathrm{s}$ to explain the present relic density. Due to the huge life time required, decaying Dark Matter particles are less favored by theory. A long list of potential Dark Matter particles is discussed for this scenario:

Table 1: The most important channels for pair annihilation of the lightest Kaluza-Klein particle and branching ratios (BR) for the final states

$\chi\chi \rightarrow$	BR
$\nu_e\bar{\nu}_e, \nu_\mu\bar{\nu}_\mu, \nu_\tau\bar{\nu}_\tau$	0.012
$e^+e^-, \mu^+\mu^-, \tau^+, \tau^-$	0.2
$u\bar{u}$, $c\bar{c}$, $t\bar{t}$	0.11
$d\bar{d}$, $s\bar{s}$, $b\bar{b}$	0.007

- Axions are introduced to explain the CP (charge conjugation and parity) conservation in strong interactions. An additional broken symmetry (Peccei-Quinn symmetry) is postulated resulting in a new particle, the axion [PQ77]. The axion is a boson. Only for small masses ($<$ GeV) it is sufficiently stable to achieve the required life time.

- The gravitino is the super-symmetric partner of the graviton, as predicted by theories combining general relativity and super-symmetry [Buc09]. In these theories it is a good candidate for the lightest super-symmetric particle. As a proposed solution to the hierarchy problem of the Standard Model, and in order to allow grand unification, the super-symmetry breaking scale needs to be pushed down to the TeV range. Therefore the gravitino mass needs to be at the same order of magnitude.

- WIMPZILLAS are super heavy Dark Matter candidates [Zia00]. Their mass is above 10^{12} GeV. WIMPZILLAS could have been produced in the evolution of the early universe.

- Q-balls arise in super-symmetric theories with bosonic particles, if there is an attraction between the particles [KS98]. The unstable super-symmetric partners of the fermions can form a Q-ball. The Q-ball and the particles therein are stable due to the attractive interaction. It is the lowest-energy configuration of that number of particles.

- Certain grand unified theories predict topological defects to have formed in the early universe [BV00]. As the universe expanded and cooled, symmetries in the laws of physics began breaking down in different regions without causal contact; topological defects occur where different regions came into contact with each other.

The given list is not complete, but gives an overview of the basic ideas. All these hypothetical particles could exist with the required live time and abundance and would decay slowly over time.

2.4.3 Expected Neutrino Signal

To detect the Dark Matter particles from the halo, the neutrino flux generated by decays or annihilation's of Dark Matter particles is searched for. The flux (differential in energy

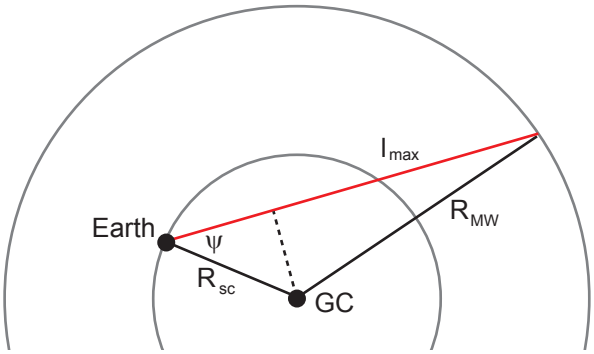

Figure 8: Sketch to explain the line of sight integration (equation 21). ψ is the observed direction relative to the Galactic Center (GC) and $l_{\max}$ is the maximum distance from the Earth taken into account. The Earth is at a distance $R_{\rm sc}$ from the GC and $R_{\rm MW}$ is the maximum distance from the GC included in the integration.

E, area A, time T and observation direction ψ) in case of decaying Dark Matter particles is

$$\frac{dN_\nu}{dEdAdTd\psi} = \frac{1}{\tau} J_1(\psi) R_{\rm sc} \frac{\rho_{\rm sc}}{m_\chi} \frac{1}{4\pi} \frac{dn_\nu}{dE} \,. \tag{19}$$

τ is the life time of the Dark Matter particles and $1/\tau$ the decay rate. $R_{\rm sc} \approx 8.5\,\mathrm{kpc}$ is the distance between the Earth and the Galactic Center. $\rho_{\rm sc}/m_\chi$ is a short notation for $\rho_{\rm DM}(R_{\rm sc})/m_\chi$ and is the Dark Matter number density. A fraction of $1/4\pi$ is included for an isotropic radiation at the production place. dn_ν/dE is the energy distribution of the expected neutrinos at the Earth describing the unknown decay process. It directly depends on the theory realized in nature and the parameters therein. The flux expected from neutrino annihilations has similar dependencies and is given by

$$\frac{dN_\nu}{dEdAdTd\psi} = \frac{<\sigma_A v>}{2} J_2(\psi) R_{\rm sc} \frac{\rho_{\rm sc}^2}{m_\chi^2} \frac{1}{4\pi} \frac{dn_\nu}{dE} \,. \tag{20}$$

Here, the decay rate is replaced by the self annihilation cross section $<\sigma_A v>/2$ and depends on the square of the Dark Matter number density. The observed amount of Dark Matter depends on the part of the halo in the line of sight. This is considered by the factors J_i, $i = 1, 2$ in the equations for the neutrino flux. It is given by (figure 8)

$$\begin{aligned} J_i(\psi) &= \frac{1}{R_{\rm sc}\rho_{\rm sc}^i} \int_0^{l_{\max}} \rho_{\rm DM}^i\left(d(l)\right) dl \\ d(l) &= \sqrt{R_{\rm sc}^2 - 2lR_{\rm sc}cos(\psi) + l^2} \\ l_{\max} &= R_{\rm sc}cos(\psi) + \sqrt{R_{\rm MW}^2 - R_{\rm sc}^2 \sin^2(\psi)} \end{aligned} \tag{21}$$

$l_{\max}$ is the maximum distance from the Earth taken into account, i.e. the far side of the galaxy. The equation depends on the observed direction ψ. $R_{\rm MW}$ ensures that all Dark Matter within a certain radius from the center of the Galaxy is taken into account. Typically $R_{\rm MW}$ has values larger than $20\,\mathrm{kpc}$. The value of J_i strongly depends on the

Table 2: Parameters of the Moore [M+99], Navarro-Frenk-White (NFW) [NFW96], Kravtsov [K+98] and Einasto [M+06] halo models. r_S is in units of kpc and ρ_{DM} in GeVcm^{-3}.

	α	β	γ	r_S	$\rho_{\mathrm{DM}}(R_{\mathrm{sc}})$	equation
Moore	1.5	3	1.5	28	0.27	22
NFW	1	3	1	20	0.3	22
Kravtsov	2	3	0.4	10	0.37	22
Einasto	0.17	-	-	20	0.3	23

Dark Matter density $\rho_{\mathrm{DM}}(r)$. This is discussed in section 2.4.4. The line of sight integral J_i has a different dependency on the Dark Matter density for the assumption of decaying and annihilating Dark Matter particles. The amount of decaying Dark Matter depends on the density while it is the density squared for the annihilation: two particles are required. Assuming a fixed amount of Dark Matter particles decaying or annihilating the difference in the expected flux at the Earth is determined by the line of sight integral over the density or the density squared.

2.4.4 Cold Dark Matter Halo Models

The expected signal from Dark Matter particles at the Earth strongly depends on the amount of Dark Matter in an observed direction and thus on the Dark Matter density profile in the halo of the Galaxy. Dark Matter halos do explain the observed rotation curves of galaxies. The simplest version is a radial symmetric matter density $\rho_{\mathrm{DM}}(r)$. The center with the highest density is at the center of the galaxy and the density decreases with larger distances. Besides the rotation curves, no direct measurements of the profiles exist.

Dark Matter distributions are derived by simulating huge numbers of particles interacting gravitationally. The initial conditions depend on the properties of the early universe. Usually a Cold Dark Matter dominated universe (ΛCDM model) with a total mass of $\Omega = 1$ is assumed. As time goes by, the particles form structures and clump. Finally, the Dark Matter density is extracted from the particle distribution after a given time. The variety of different parametrization and models is huge [M+06] and only some are discussed here.

The commonly referred to halo model is the Navarro-Frenk-White (NFW) model [NFW96]. It is based on a double power-law describing the inner cusp and the outer part of the halo (figure 9). It uses

$$\rho_{\mathrm{DM}}(r) = \rho_0 \left(\frac{r}{r_S}\right)^{-\gamma} \left(1 + \left(\frac{r}{r_S}\right)^{\alpha}\right)^{(\gamma-\beta)/\alpha} \tag{22}$$

as parametrization. ρ_0 is the absolute scale and is determined from the Dark Matter density at the solar circle R_{sc}. γ is the index for the inner cusp and β the outer parts index. r_S is the scale radius. It determines the radius of the change between the two power laws. The values of the parameters α, β and γ are given in table 2 and are verified by N-body simulations of the evolution of Dark Matter halos of different masses. Afterwards, the profile with fixed parameters α, β and γ is fitted to the simulated Dark Matter mass

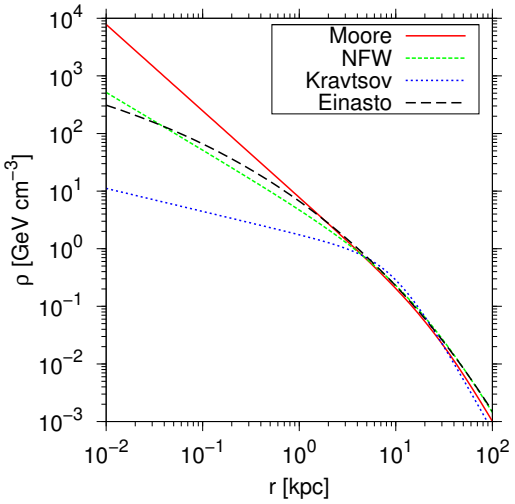

Figure 9: Dark Matter density for the the Galaxy given by different models: Moore [M$^+$99], NFW [NFW96], Kravtsov [K$^+$98] and Einasto [M$^+$06]. The used parameters are given in table 2.

distribution at distances of some kpc to more than 100kpc distance from the center of the halo.

In comparison, Moore et al. [M$^+$99] find good agreement with their N-body simulations for a different set of parameters α, β and γ (table 2). The resulting Dark Matter density rises steeper towards the center (figure 9). This profile fits better to observational results from rotation curves of low surface brightness galaxies, supposedly dominated by Dark Matter. Only in the inner most part an even higher Dark Matter density is required to explain the observed rise in the rotation curves.

Kravtsov et al. [K$^+$98] investigated a different set of Dark Matter dominated low surface brightness galaxies and dwarf galaxies. They find a good agreement using a shallow cusp (parameters given in table 2 and shown in figure 9). In addition, their result is compared to simulations using various cosmological models: the ΛCDM model as well as a model without cosmological constant (CDM) and a model including Hot Dark Matter.

The three models presented above are all based on a double power-law. In comparison to the NFW profile the other two models differ manly in the cusp region and are used to represent possible variations in the halo models.

A different approach is to describe the Dark Matter density by an equation derived by Einasto et al. for density systems with a spherical distribution of stars [Ein65] (values in table 2 and shown in figure 9):

$$\rho_{\mathrm{DM}}(r) = \rho_0 \cdot exp\left(-\frac{2}{\alpha}\left[\left(\frac{r}{r_S}\right)^{\alpha} - 1\right]\right) . \tag{23}$$

The Dark Matter density decreases exponentially. As shown in [M$^+$06], this density can describe certain results from simulations better than the densities discussed above. Additionally, the total mass of the halo has a finite value (the integration diverges for equation 22). The resulting profile is similar to the NFW model.

These four models are in the following used to determine the flux of neutrinos expected from the Dark Matter halo of the Galaxy.

2.4.5 Recent Measurements related to Dark Matter

Based on the observational evidences for Dark Matter, several projects aim at the detection of its particle content. Two types of experiments can be distinguished: direct observations and indirect observations. The direct searches detect Dark Matter particles interacting directly within their detector. They are sensitive to the interaction cross section of the 'new' particles with the Standard Model particles. In contrast, indirect measurement can measure the interaction cross section and the self annihilation cross section or the decay rate by observing different objects in space.
The current analysis focuses on the observation of the halo and it is sensitive to the self annihilation cross section or decay rate of the Dark Matter. Therefor, the direct Dark Matter searches are only shortly introduced. Recent experiments are XENON [XEN04] and CDMS [CDM04]. They are sensitive to Dark Matter particles with masses in the range of several GeV to TeV. To date, no Dark Matter particles have been detected. CDMS reports two events which could be caused by Dark Matter particles but the measurement is still within statistical fluctuations of the background [CDM09].
Indirect searches for Dark Matter are performed by various experiments detecting neutrinos, γ-rays, (anti-)protons or electrons and positrons. Experiments observing uncharged particles probe the annihilation cross section or decay rate by observing the galactic halo, the Galactic Center or other galaxies. Additionally, the interaction cross section is measured by observing massive objects, which accumulate Dark Matter particles in their core. The neutrino detectors (MACRO [MAC99], Super-Kamiokande [Sup04], AMANDA [BH09] and IceCube [Ice10a]) have not observed any Dark Matter particle up to now. For charged particles the energy spectra are measured and searched for features indicating a Dark Matter contribution.
Recent results from the Fermi Large Area Telescope (LAT) [Fer09b] indicate an excess of the electron plus positron flux at energies above 100 GeV. This confirms the earlier results from ATIC [C$^+$08] and PPB-BETS [PPB08]. The HESS [HES09b] collaboration also reported an excess of $e^+ + e^-$ above 340 GeV, confirming their previous results [HES06b]. Meanwhile PAMELA data [PAM09] has shown an excess in $e^+/(e^+ + e^-)$, compared to the Galactic background at 10 to 100 GeV. PAMELA also confirms the earlier results from HEAT [HEA97] and AMS [AMS07]. Although standard astrophysical sources may be able to account for the anomaly ([HBS09], [YKS08], [Pro08], [H$^+$09], [SNP09], [DD09], [MCG09], [F$^+$09], [B$^+$09] and more), the positron excess at PAMELA and the electron plus positron flux of Fermi LAT have caused a lot of excitement being interpreted as indirect detection of Dark Matter ([HSZ08], [RU09], [CM09], [STY09], [CGZ09], [HNN09], [Y$^+$09], [OY09], [FKS09], [LYZ09] and more).
In [MP09] the annihilation of Dark Matter particles of different masses is fitted to the measurements of PAMELA, Fermi and HESS The favored regions, as function of the mass of the particle and the self annihilation cross section are shown in figure 10. The authors assume the NFW halo model and annihilation into a pair of b-quarks, W-bosons or muons. The PAMELA data only allows for a large area in parameter space and covers the complete shown mass range. For large masses also larger self annihilation cross sections are required.

If the HESS and Fermi LAT measurements are included in the fit, a mass at about 1 TeV seems the most promising hypothesis.
In [PS09] an overview of the measurements of the self annihilation and the life time is given. Figure 10 shows the self annihilation cross section and the Dark Matter masses favored by PAMELA and HESS measurements as well as several limits obtained by Super-Kamiokande, FERMI, HESS and VERITAS. All these calculations assume the annihilation into one specific Standard Model particle. The limits are obtained by various methods:

- PAMELA has observed an excess in the positron fraction of the cosmic rays [A$^+$09]. No limit is derived. This excess can be explained by various choices for the Dark Matter particle mass and the self annihilation cross section. The best fitting values are determined for various halo models and decay channels in [MP09]. For all models self annihilation cross sections larger than the natural scale are required.

- FERMI has observed an excess in the electron-positron flux [Fer09b]. This excess can be explained only by a dominantly leptonic annihilation of the Dark Matter particles [MP09].

- FERMI also observed the γ-ray flux from the Galactic Center [Por09][Fer09a]. The identification of the origin of this flux is complicated because of different sources in the observation region. Limits on the self annihilation cross section are derived in [PS09]. The authors consider γ-rays from final state radiation and inverse Compton scattering. The scattering depends on the diffusive volume of the Galaxy L.

- HESS observations of γ-Rays from the Galactic Center (GC) [HES06b] and the Galactic Center Ridge (GR) [HES06a]. To derive limits on the Dark Matter annihilation the diffuse γ-ray background and the flux from other sources have to be considered.

- HESS and VERITAS observe γ-rays from dwarf galaxies [HES08][VER08]. Limits in are computed in [ESS09] but are strongly dependent on the assumed Dark Matter density.

- Super-Kamiokande observes neutrinos traveling through the Earth from the direction of the Galactic Center [Sup04]. This measurement is particularly robust. No foreground sources have to be considered.

- The fluctuations in the Cosmic Microwave Background (CMB) depend on the evolution of the Universe and therefore on the amount and on the properties of the Dark Matter. Dark Matter annihilations and decays into standard model particles heat the surrounding medium. Therefor, photons in regions with enhanced Dark Matter density should decouple later. This causes fluctuations in the CMB. WMAP has measured these fluctuations [K$^+$09] and derived limits on the self annihilation cross section [CIP09]. In comparison to the other limits, the limit from the CMB does not depend on the halo profile.

The limits discussed are in general more than one order of magnitude above the natural scale (section 2.4.2) for the self annihilation cross section (figure 10). They are at the

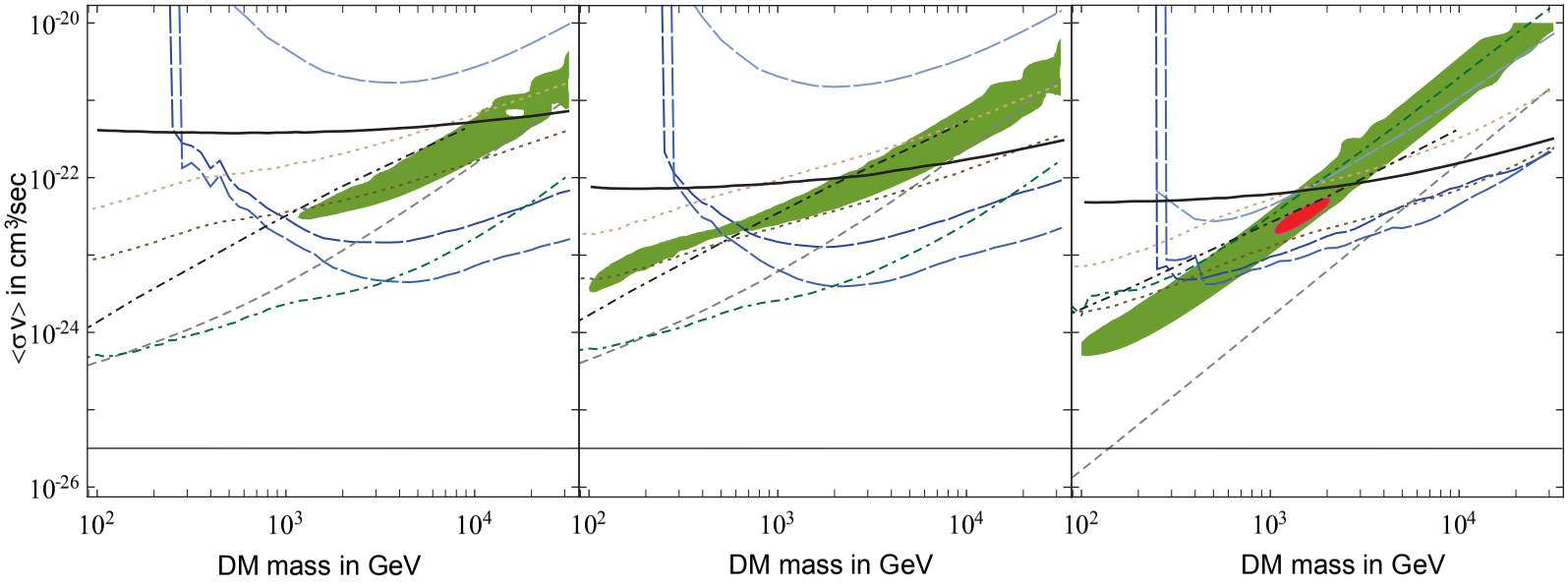

Figure 10: Upper limits (3σ) from various experiments on the Dark Matter self annihilation cross section $< \sigma v >$ assuming an NFW or Einasto halo profile: left: annihilation into $b\bar{b}$; middle: annihilation into W^+W^-; right: annihilation into $\mu^+\mu^-$. Blue (long dashed) limits are derived by HESS observations of the GC, GR and dwarf spheroidal galaxies (dark to bright). The green (dot-dash-dashed) limit is set by FERMI assuming final state radiation of photons and the brown (dotted) lines assuming inverse Compton photons (diffusive volume L = 1 kpc for the bright curve and 4 kpc for the dark curve)). The gray (dashed) curve refers to the GC-radio bound by observations of the central black hole. The black (dot dashed) limit is set by WMAP observations of the CMB and the black (solid line) is the limit set by Super-Kamiokande (90% C.L.). The green (bright gray) region shows the values favored by the PAMELA excess and the red (dark gray) region shows the values favored also including the FERMI $e^{\pm}$ excess. Figures modified from [PS09].

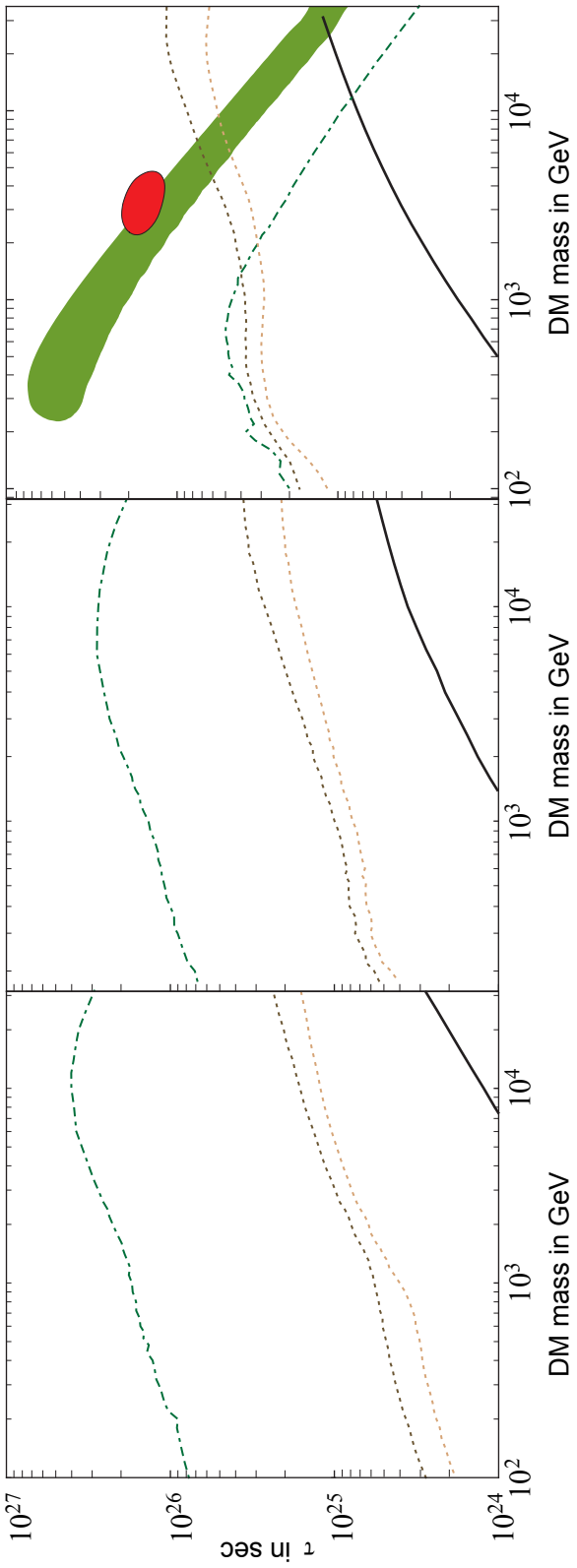

Figure 11: Lower limits (3σ) from various experiments on the Dark Matter life time τ assuming an NFW halo profile: left: decay into $b\bar{b}$; middle: decay into W^+W^-; right: decay into $\mu^+\mu^-$. The green (dot-dash-dashed) limit is set by FERMI assuming final state radiation of photons and the brown (dotted) lines assuming inverse Compton photons (diffusive volume L = 1 kpc is the bright curve and 2 kpc is the dark curve)). The black (solid line) is the limit set by Super-Kamiokande (90% C.L.). The green (bright bray) favored region shows the values by the PAMELA excess and the red (dark gray) region shows the values favored also including the FERMI $e^{\pm}$ excess. Figures modified from [PS09].

same scale as the parameter region favored by the PAMELA data. This region, however, is excluded in nearly all cases by at least one other observation.
The differences between the natural scale of the self annihilation cross section and the required values are usually explained by so called enhancement factors. These enhancement factors increase the amount of expected annihilation products without requiring a larger relic density. Two possible explanations for such a Boost Factor are the Sommerfeld enhancement [Ien09] or the Breit-Wigner enhancement [IMY09]. Due to the gravitational interactions between the Dark Matter particles substructures in the Dark Matter density of the halo are expected, so called clumps. In these denser clumps the annihilation rate is increased and thus also the expected flux. A large increase of the flux is expected from regions with a on average low Dark Matter density, while it is smaller in a region with a high density (e.g. the Galactic Center).
Alternatively, the same measurements can be applied to restrict the life time, when assuming decaying Dark Matter particles. Figure 11 shows the existing limits. Here, the HESS results are not shown. The limits obtained from high energy γ-rays are less restrictive than for the annihilations of Dark Matter. Due to the high pointing accuracy the limits depend strongly on the predicted Dark Matter density at the Galactic Center. The expected signal flux for decays depends linearly on the Dark Matter density, while the flux from annihilations depends quadratically on it. Measurements observing larger parts of the sky are less affected due to the smaller average Dark Matter density. The limits are at the order of 10^{26} s and thus in the physically possible range.
The observed positron excess can be explained only by leptonic decays of the Dark Matter particles. Assuming an annihilation into a pair of muons the favored region is at masses of some TeV. These scenarios are not ruled out by any measurement, yet.

3 Neutrino Telescopes

Observing neutrinos from our Galaxy or beyond is a great challenge. This chapter explains the detection principles and the IceCube detector which is used for this analysis. Additionally, an outlook to the IceCube extension, called DeepCore, is given. Besides IceCube other neutrino telescopes are in operation or planned. They are discussed at the end of this chapter.

3.1 Detection Technique

A direct observation of neutrinos is not possible due to their low interaction cross section. Neutrinos are usually detected by the products of their rare interaction with a nucleus. This interaction is caused by the weak force. Two different interactions are possible:

$$\begin{aligned} \nu + N &\rightarrow Z^0 \rightarrow \nu + X \\ \nu + N &\rightarrow W^{\pm} \rightarrow l + X \end{aligned} \tag{24}$$

l denotes the lepton corresponding to the neutrino flavor. X is the remnant of the nucleus. For neutrinos with energies above 1 GeV sufficient energy is transferred to the nucleus to be destroyed. In this cases X denotes the hadronic cascade. In this work the charged current interaction is used. Unlike, the neutral current interaction, the charged current interaction produces a lepton, whose energy and direction are measured.
The direction determines the origin of the neutrino. Due to the indirect observation only the direction of the lepton is measured. The average angular difference $\Delta_{\nu l}$ between the neutrino and the lepton direction is approximated by [LM00]:

$$\Delta_{\nu l} \approx \frac{0.7^\circ}{(E_\nu / \mathrm{TeV}^{0.7})} \, . \tag{25}$$

Due to a larger boost factor the difference $\Delta_{\nu l}$ decreases with higher neutrino energies E_ν. For a neutrino of 10 GeV the angle is about 3.5°, while it is only about 0.14° for a neutrino of 10 TeV.

3.1.1 Cherenkov Effect

The Cherenkov effect [MS53] is used to detect the products of a neutrino interaction: the hadronic cascade or the lepton.
The Cherenkov effect is explained by electrodynamics: A charged particle, which moves through a medium, polarizes the molecules along its path via its electromagnetic field. When the molecules fall back in their equilibrium state, they emit electromagnetic radiation. If the charged particle's velocity is small, the emitted photons interfere destructively with each other and no light is observed. If, however, the particle's velocity is higher than the speed of light in the medium, the production of new wave fronts along the particles path is faster than the propagation of the wave fronts. Therefore the electromagnetic waves can interfere constructively according to the Huygens principle in a certain direction. A light cone is formed (see figure 12). The half opening angle θ_c of the cone is given by

$$\cos(\theta_c) = 1/(\beta n) \, . \tag{26}$$

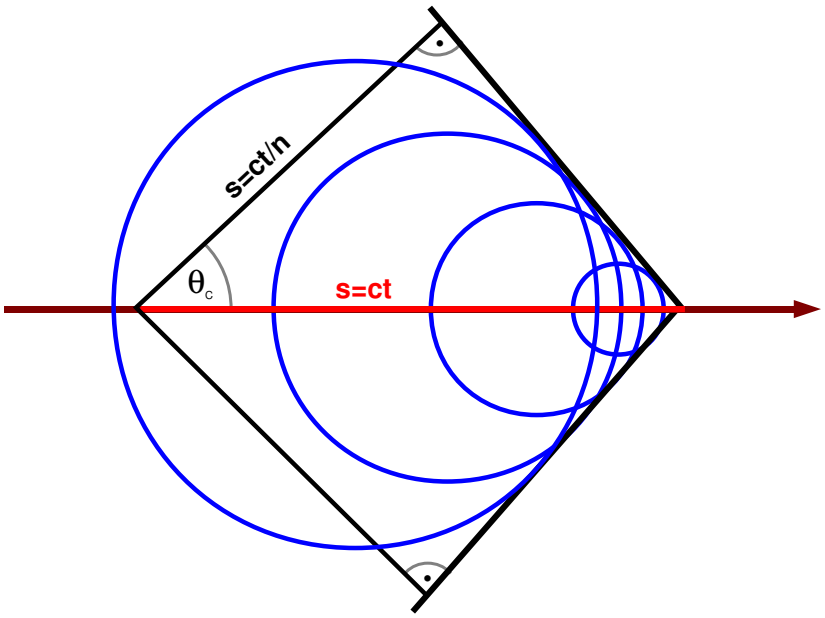

Figure 12: Cherenkov cone of a particle moving along a track with waves interfering constructively. s is the distance covered in a time t. The particle is moving with the speed of light c, while the speed of the Cherenkov photons is decreased to c/n.

$\beta = v/c$ is the charged particles velocity in units of the speed of light and n the refraction index. In ice and for $\beta = 1$ an angle of $\theta_c \approx 41°$ is derived. The number of photons N emitted per track length dx is given by the Frank-Tamm-Formula [Jac96]

$$\frac{d^2N}{dxd\lambda} = \frac{2\pi\alpha_f}{\lambda^2}\left(1 - \frac{1}{\beta^2 n^2}\right) . \tag{27}$$

α_f is the fine structure constant and λ the wavelength. For wavelengths between 300 nm and 500 nm about 250 photons are emitted per centimeter. The corresponding energy loss is

$$\frac{dE}{dx} = \frac{dN}{dx} < E_\gamma >= \frac{dN}{dx}\frac{hc}{< \lambda >} \approx 850\frac{\text{eV}}{\text{cm}} . \tag{28}$$

The emission of Cherenkov photons is not the dominant process of the energy loss. Especially for muons other processes are more important (see next section). Charged secondary particles produced in these processes also contribute to the Cherenkov light emitted. These secondary particles are low energetic or nearly aligned with the lepton direction. If they are low energetic, their speed is smaller than the speed of light and no Cherenkov light is emitted.

The emission of Cherenkov photons at an angle of typically 41° in ice enables the detection at a certain distances to the particle track. Thus, the sensitive instruments can be positioned in a grid at larger distances. This allows an easy instrumentation of a large volume.

3.1.2 Energy Loss and Decay of Leptons

The Cherenkov light is emitted by the leptons and the charged particles in the hadronic cascades as long as their energy is high enough. For a muon this is about 160 MeV total energy. The energy loss caused by the Cherenkov effect is small compared to the loss by other mechanisms. Thus, the distance a lepton travels and the deposited energy are limited by these other mechanisms.

High energy electrons loose energy by radiating brems photons which then do pair production. The interaction length for both processes is about the same. This creates a cascade of particles. Due to the boost these particles are roughly aligned with the initial electron. Small changes in direction due to interactions broaden the angular distribution of the emitted Cherenkov light.

In contrast to the case of an electron the energy loss of a muon is caused by various effects:

Ionization: The kinetic energy of the muon E_{kin} is large compared to the mean energy I required to ionize an atom. The muon knocks an electron out of the atomic shell. The energy loss of the muon dE/dx is described by the Bethe-Bloch-Formula [Par08]

$$\frac{dE_\mu}{dx} \propto \frac{Z}{A}\frac{1}{\beta^2}\left(\frac{1}{2}\ln\left(\frac{2m_e c^2\beta^2\gamma^2 T_{\max}}{I^2}\right) - \beta^2 - \frac{\delta}{2}\right) . \tag{29}$$

Here, Z and A are the charge number and the mass number of the atom and m_e is the mass of the electron. $T_{\max}$ is the maximum kinetic energy which can be transferred to a free electron in a single collision and δ is a density effect correction. The ionization is described as continuous energy loss. Additionally, stochastic production of delta electrons has to be taken into account.

Bremsstrahlung: A muon is deflected in the electromagnetic field of the nucleus and emits a bremsstrahlung photon. In comparison to the electron the muons loose less energy by brems emission ($dE_\mu/dx \propto m_{\mu/e}^{-4}$), where m_μ and m_e are the masses of an electron and a muon, respectively. Thus, muons emit brems photons less frequently: $((m_e/m_\mu)^4 \sim 5 \cdot 10^{-10}$.

Pair production: If the energy of the muons is high enough, virtual brems photons for pair production are produced. The minimum energy is about 1 MeV for electron-positron-pairs and about 210 MeV for μ^- μ^+ pairs. Here, a third charged particle (a nucleus) has to exist which takes the recoil.

Photo nuclear reactions: These are interactions where a hard virtual photon interacts with a parton or nucleon. These interactions are rare compared to pair production or Bremsstrahlung. Energy is transferred to the nucleus by a virtual photon. Usually, the nucleus is destroyed.

The total energy loss of a high energetic muon in water can be approximated by [Par08]:

$$\begin{aligned} \frac{dE_\nu}{dx} &= a + bE_\nu \text{ , where} \\ a &\approx 2\,\mathrm{MeV/cm} \\ b &\approx 3.6 \cdot 10^{-6}/\,\mathrm{cm} \text{ .} \end{aligned} \tag{30}$$

In first order the values of a and b are independent of the energy. The constant part of the energy loss is the result of ionization. Below a critical energy of about $E_\nu \approx 600\,\mathrm{GeV}$ the ionization is dominant, while above this value radiative reactions dominate. Here, the stochastic character has to be taken into account, while the ionization can be treated as continuous energy loss.

Taus are heavier than muons and thus loose less energy radiatively. Their lifetime is about 0.3 ps [Par08]. For an energy larger than 1 PeV a tau can travel a distance of more than 100 m. The tau decays into a neutrino and a W-boson. The W-boson further decays hadronically or leptonically. In case of a hadronic decay a cascade is initiated. The leptonic decay can either result in an electron, which also initiates a cascade or in a muon. The cascades are nearly spherical due to the huge amount of interactions.

3.1.3 Signatures in a Detector

As given in formula 24 the neutrinos interact via the charged current or neutral current interaction. In case of a neutral current interaction only the hadronic cascade could be observed by Cherenkov light. In the charged current interaction additionally a lepton (of the same flavor a s the neutrino) can be observed. The properties of the observed Cherenkov light depend on the flavor of the produced lepton.
A electron directly creates an electromagnetic cascade. Both cascades emit Cherenkov light in all directions. Nevertheless, this radiation is boosted into the direction of neutrino momentum. Due to the about spherical wavefront the interaction point can be reconstructed with high accuracy, but it complicates the reconstruction of the neutrino direction. All energy is deposited inside of a relatively small volume and allows a measurement of the neutrino energy.
Due to the small energy loss a muon travels a long distance before it is stopped or decays. For muon neutrinos this long track allows a precise measurement of the direction. If a muon passes through the detector volume, its energy loss can be measured and the muon energy is determined by equation 30. For minimal ionizing muons (below $\sim 600\,\mathrm{GeV}$) this estimate fails, because the energy loss is not energy dependent. To derive the neutrino energy from the muon energy the initial hadronic cascade has to be taken into account. If the interaction point of the neutrino is outside of the detector volume, the energy of the hadronic cascade is not measured.
A tau has a short life time and decays initiating another hadronic cascade or producing a muon or electron. Both cascades create a spherical light emission. They are connected by a track emitting Cherenkov light. At energies above 1 PeV the tau track is longer than 50 m and the tau event can be reconstructed. For the identification of the tau neutrino by its signature both cascades (double bang event) or the tau decay cascade (loli-pop event)

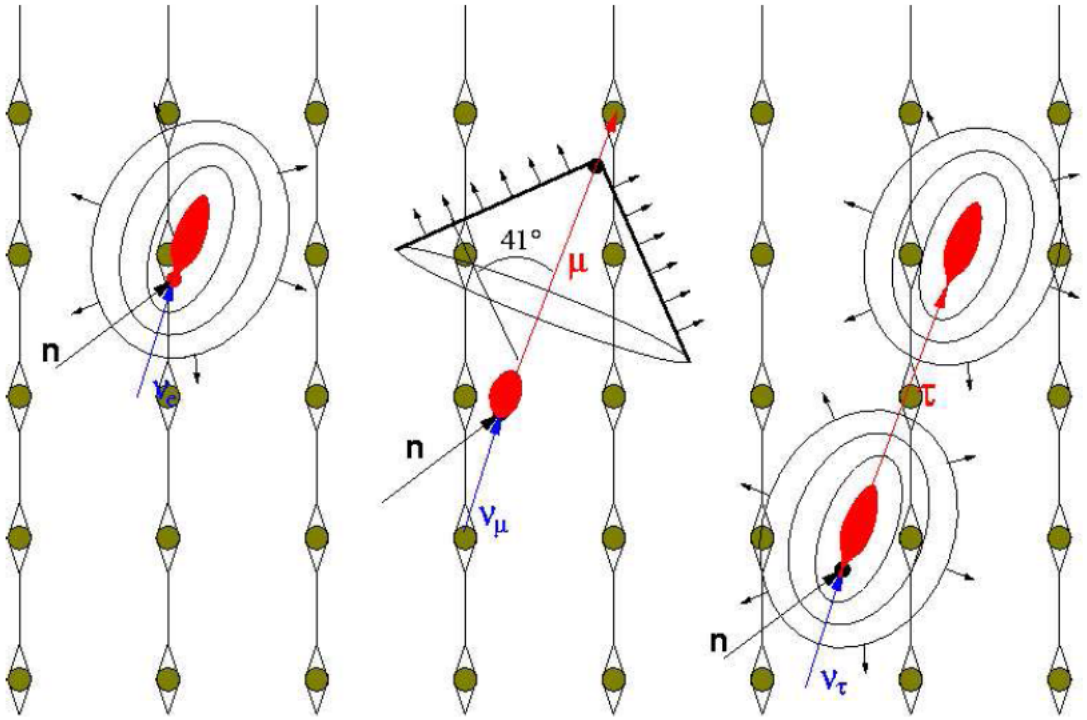

Figure 13: Schematic view of the the different neutrino signatures depending on the flavor. The arrows are tracks. Tracks of muons or taus (red) emit Cherenkov light. The red areas symbolize cascades of particles emitting Cherenkov light. Figure from [Gro06].

have to be inside the detector. The energy reconstruction has to consider both cascades and the track in between and is therefore more complicated.

3.2 IceCube

The 'IceCube' detector [Ice] is under construction near the geographic South Pole. A schematic view is shown in figure 14. It consists of a surface air shower detector called 'IceTop' and an in-ice Cherenkov detector-array (usually referred to as IceCube).
The in-ice part itself consists of 86 so called strings with 60 digital optical modules (DOM) each including 15 inner strings with denser spacing which form the 'DeepCore' detector (subsection 3.2.2). The strings are lowered into drilled holes in the ice of the glacier. The holes form a hexagonal grid (horizontally). The distance between two strings is about 125 m. The DOMs are located at a depth between 1450 m and 2450 m with a distance of about 17 m to each other. Each DOM consists of a photomultiplier in a pressure housing. Additionally, a digitization board, a light emitter device for calibration issues and the high voltage supply for the photomultiplier are built in.
The deployment began in the austral summer 2004/05 with a first string. In the following years further strings were deployed and the detector grew from 1 string to 9 strings, to 22 strings, to 40 strings, to 59 strings and to 79 strings in the year 2010. These partial detectors are called IC1, IC9, IC40, IC59 and IC79 referring to the number of strings,

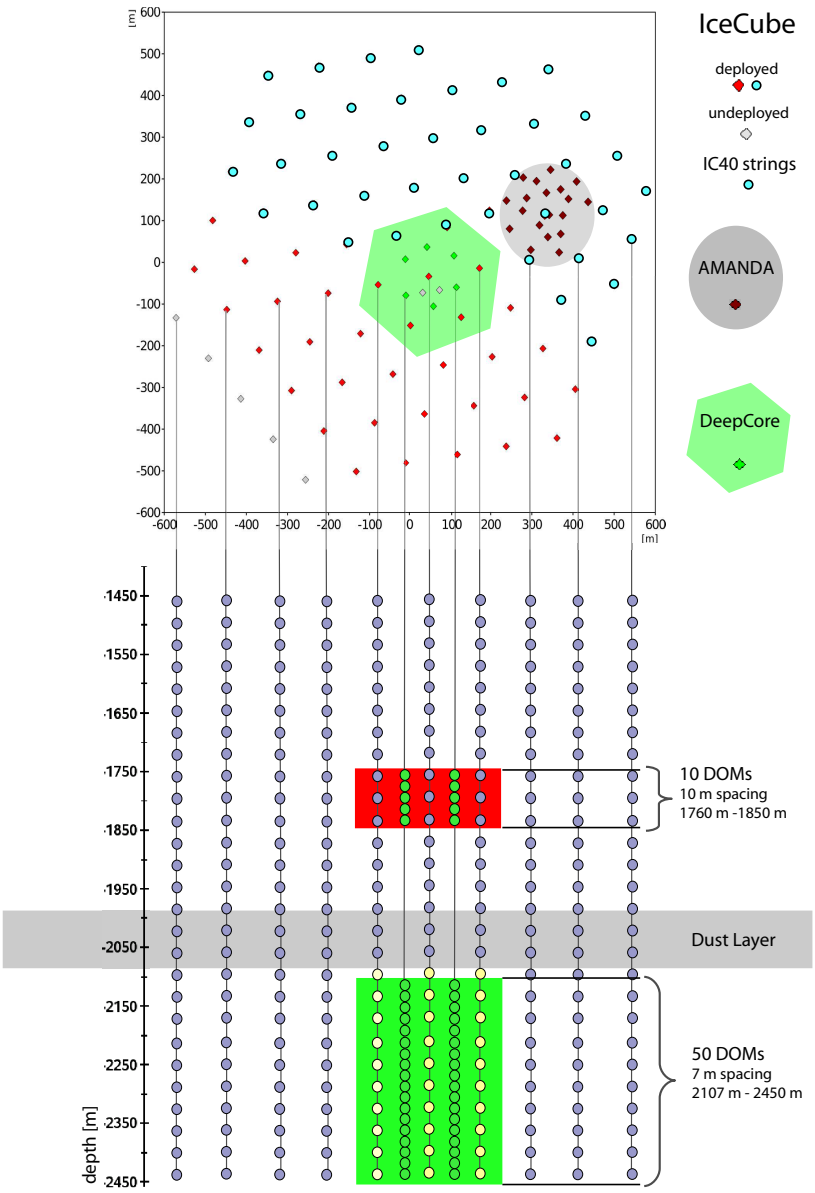

Figure 14: Schematic view of the IceCube detector. Upper part: A top view of the detector marking the position of each string. Strings marked in light gray are not yet deployed. The turquoise circles mark strings which are part of IC 40. Additionally, the positions of the AMANDA and DeepCore strings are shown. The lower part of the figure shows the in-ice layout. Shaded are the volumes with additional DeepCore instrumentation and the Dust Layer. Modified figure from [Ice10b].

respectively. One of the strings of IC59 and six of IC79 are part of the DeepCore sub-detector (next section).
The strings with attached DOMs will instrument a volume of about $1\,\mathrm{km}^3$ and measure the Cherenkov light emitted nearby. The reach depends on the local ice properties (section 3.2.3). If a sufficient number of DOMs record light (section 3.2.5) a trigger is issued (section 3.2.6). The digitized signals are transferred to the surface and and recorded. There, in a large computing farm first reconstructions and event selections are performed. All data are stored to tape while only the selected events are directly transferred to the North via satellite. In the North more sophisticated reconstructions and more detailed event selections are performed: some in a collaboration-wide effort, and others individually for a specialized analysis. The details of this analysis are described in chapter 6.

3.2.1 Experimental Signals and Backgrounds

The instrumentation of the IceCube detector enables the detection of neutrinos with energies above typically 100 GeV. This value depends on the string spacing and the amount of light emitted. With the DeepCore sub-detector the lower energy threshold is approximately 10 GeV (section 3.2.2). The signatures of these signal events in the detector are discussed in section 3.1.3.
The main background for neutrino searches in IceCube are events caused by muons produced in the atmosphere by air showers. The spectrum of primary particles reaches up to the ZeV scale and the production of high energetic secondary particles is possible. The expected energy spectrum is about $dN_\mu/dE \propto E^{-3.7}$. The spectrum is steeper compared to the Comic Ray flux due to the production of several secondary particles. The exact spectrum also depends on the observed direction, because different atmospheric depth have been traversed by the air shower.
The produced atmospheric muons travel through the atmosphere and deep into the ground. Due to IceCube's depth of more than 1400 m a reduced rate reaches the detector. IC40 triggers these events with a rate of approximately 1 kHz. Due to this large number also rare mis-reconstructions and other rare effects have to be considered for these muons.
Muon and neutrino induced events in the detector can be distinguished by three different approaches:

- The direction: The parent particle of events moving upwards through the IceCube detector must have passed through the Earth before. This is only possible for neutrinos and only mis-reconstructions of downward moving muon events produce a background.

- The energy: The energy spectrum of the atmospheric muons is steeply falling. Thus, less background events are expected for high neutrino energies.

- The position of the first recorded light: Muons always enter the detector from outside and deposit the first light at the edges of the detector. Neutrinos could interact inside of the detector. The light emitted by the resulting lepton is first observed in the inner detector part. This different signatures can be utilized by an active veto. If the observed track starts within the detector it originates from a neutrino.

The first method is used to observe mainly the Northern Sky through the Earth, while the other two methods are applied to search for neutrino signal from the Southern Sky.

In searches for extra-terrestrial neutrinos, not only muons but also neutrinos produced in air showers are considered as background. Similar to the muons, they are expected to have a steeply falling energy spectrum. Besides the energy, only directional correlations can distinguish between an event from a neutrino produced in the atmosphere and an event originating from an extra-terrestrial source. Additionally, atmospheric neutrinos can be accompanied by muons from the same pion or kaon decay [S$^+$09]. Above about 1 TeV the muon and the neutrino can be treated as aligned and both could reach the detector at the same time. The signature of such a neutrino events is overplayed with the muon signature which deposits light at the edges of the detector. Thus, it can be removed by a veto in the same way as events caused by atmospheric muons.

3.2.2 DeepCore

In addition to the original plan, IceCube is more densely instrumented in the lower center (figure 14). The so called DeepCore [Ice10b][Wie09]. It consists of 15 strings. Seven standard IceCube strings and eight additional strings between them. Six of the additional strings are arranged around IceCube string 36, each at the center of a triangle with the neighboring strings. The distance between the additional DeepCore strings and the IceCube strings is about 72 m. 50 DOMs on these strings are positioned with 7 m spacing in the lowest 350 m of the detector. Additional 10 DOMs are located with 10 m spacing in a depth of 1760 m to 1850 m. These DOMs are equipped with photomultiplier tubes with a higher quantum efficiency.
The remaining two strings are again placed at the center of two triangles with a distance of about 42 m to the neighboring strings (figure 14). This additional instrumentation creates a more densely instrumented volume of about 0.02 km^3 (including the conventional IceCube strings) in the lower center of IceCube and an even denser volume of 0.001 km^3 around the last two strings.
These denser instrumented regions are advantageous for the detection of neutrinos with energies below 1 TeV. These generate lower energetic leptons and deposit less light. With DeepCore neutrinos with energies down to 10 GeV can be detected. Besides the research topics presented here, other studies also profit from the denser spacing: For example a search for oscillations of atmospheric neutrinos [Eul][Gei] and monopole searches [Glu].
With a position at the bottom center of IceCube the rest of the detector can be used as veto. Atmospheric muons are likely to be detected in the outer IceCube part before they reach DeepCore. This allows the separation between muon and neutrino induced events from above. Additionally, the upper-most ten DOMs of the DeepCore strings improve the capabilities of this veto. It is thus possible to observe the southern sky [Eul08][Wie09].

3.2.3 The Ice Characteristics at the South Pole

The capabilities of IceCube are largely determined by the optical properties of the glacial ice [Ice06]. All emitted Cherenkov light propagates through the ice and is eventually detected by a photomultiplier in one of the DOMs. The properties of the ice are usually described by two relevant parameters: the effective scattering coefficient a_{eff} and the absorptivity a_{abs}. Both are wavelength and depth dependent (figure 15). The effective scattering coefficient takes into account that the important factor is not the total scatter-

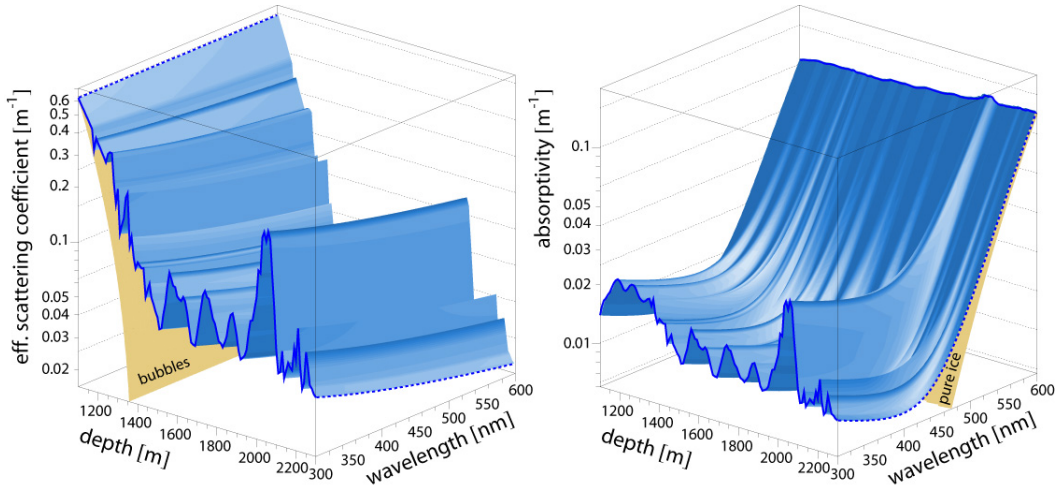

Figure 15: Effective scattering length (left) and absorptivity (right) depending on depth and wavelength.

ing cross section but only that which scatters light significantly out of the direct path The coefficient is given by [LM00]

$$a_{\text{eff}} = a_{\text{scat}} \left(1 - < \cos(\theta_{\text{scat}}) >\right) \ . \tag{31}$$

a_{scat} is the scattering coefficient and θ_{scat} the scattering angle. The properties of the different ice layers depend on the climatic situation at the time when the ice was formed (different amounts of acids, salts, minerals and dust inclusions). In the South Pole ice, there is only a small amount of inclusions, but they still change the scattering and absorption properties. At varying depth different effects dominate. Above about 1.3 km icebound gas bubbles increase the scattering; below, there are less gas inclusions. Here, the ice properties are dominated by embedded solid materials. Five regions with increased absorption and scattering are observed below 1450 m (figure 15). These regions correspond to dust layers. The dust layer at about 2000 m depth is large compared to the others. Here, the scattering coefficient increases by nearly a factor of four. This region is referred to as 'the Dust Layer'. Typical sizes of the absorption length λ_{abs} and the effective scattering length λ_{eff} in ice are (outside the Dust Layer)

$$\lambda_{\text{abs}} = \frac{1}{a_{\text{abs}}} = 90\,\text{m} - 120\,\text{m} \ , \qquad \lambda_{\text{eff}} = \frac{1}{a_{\text{scat}}} \approx 25\,\text{m} \ . \tag{32}$$

These values determine the DOM spacing given above. The DeepCore DOMs are placed outside the Dust Layer to capture as many photons as possible. With the IceCube spacing of 125 m between two strings most of the light scatters several times before detection. This is reduced in the more densely instrumented DeepCore region where the ice is cleaner.
In addition to the general ice properties also the properties of the ice in the drilled holes have to be taken into account. There, gas bubbles and impurities from drilling raise scattering and absorption.

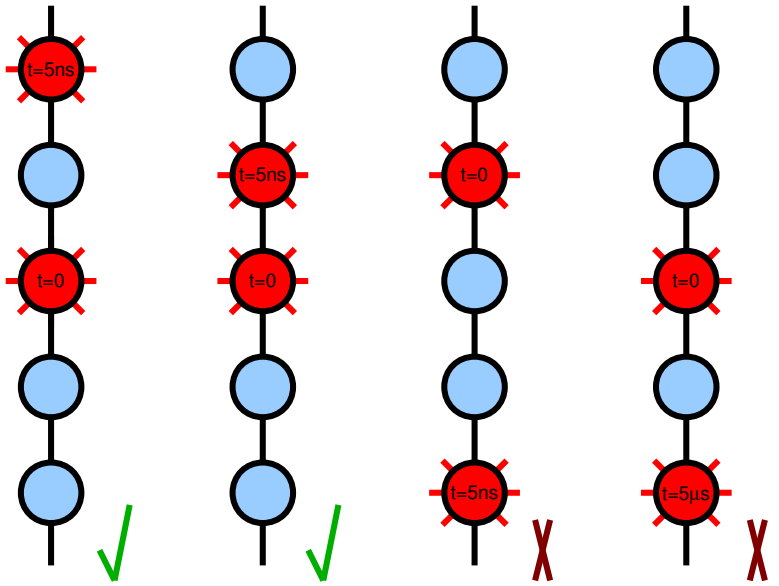

Figure 16: Hard Local Coincidence: Examples for pulses in DOMs fulfilling the HLC criterion (left side) and not fulfilling it (right side). Shown is a section of a string with five DOMs. DOMs with a pulse are marked and the time is given.

3.2.4 Measuring Neutrinos at the South Pole

If a muon (or another particle which produces light) passes through the detector, the DOMs record the emitted Cherenkov light. For each measured photon a voltage pulse is recorded. Before the DOM reports this pulse to the central computer cluster on the surface a cleaning of the pulses (section 3.2.5) is applied. The cleaned pulses of all DOMs arriving at the computer cluster are checked for trigger conditions (section 3.2.6). If one of these conditions is fulfilled, the so called joint event builder creates one event (section 3.2.6) which is processed further. For details see [Ice09d].

3.2.5 Hard Local Coincidence

Before a pulse recorded by a DOM is reported to the surface a cleaning is applied, called Hard Local Coincidence (HLC). Noise pulses are randomly distributed among the DOMs. Pulses caused by light from muons are correlated in space and time. The cleaning of noise pulses is based on this coincidences in position and time. A pulse is reported to the surface only if one of the nearest neighboring DOMs or one of the next to nearest neighbor DOMs also has measured at least one pulse within $t_{\mathrm{HLC}} = 1\,\mu\mathrm{s}$ time difference. Only DOMs along one string are taken into account, because the distance between two strings (125 m) is large compared to the distance between two DOMs (17 m). Figure 16 shows some examples.
The probability for a pair of noise hits which fulfill the HLC criterion is estimated by

$$p = 2\, t_{\mathrm{HLC}}\, r_{\mathrm{noise}}\, N_{\mathrm{DOM}}\ . \tag{33}$$

The number of neighboring DOMs is $N_{\mathrm{DOM}} = 4$. Considering a noise rate of $r_{\mathrm{noise}} \approx 260\,\mathrm{Hz}$ in each DOM about one noise pulse is expected in IC40 and in the coincidence time window of $2t_{\mathrm{HLC}}$. In this case the probability for HLC pair of noise hits is $p \approx 2 \cdot 10^{-3}$. The pulses surviving this cleaning are sent to the surface while isolated pulses are discarded.
This procedure also discards isolated pulses caused by signal events. This loss of information affects the further analysis steps and the reconstruction of the muon track. Especially for events with only a small number of pulses, this loss complicates the reconstruction or the event is lost, because the number of pulses falls below the trigger threshold. Affected are low energetic muons and muons in parts of the detector of small absorption length like the Dust Layer (section 3.2.3).
By chance the HLC requirement can remove the only pulse on a string the muon passes by. Missing one pulse usually has no critical influence on the reconstruction. This is different for the identification of muons which start or stop in the detector. Here, it is important to utilize as much information as possible from the DOMs at the edge of the detector. One rejected pulse caused by a muon entering the detector can lead to a misinterpretation of the muon as starting inside of the volume. A starting muon is a signature for a neutrino while a non-starting down-going track is most probably a atmospheric muon.
Due to the discussed difficulties at lower neutrino energies and for muon tracks starting or stopping in the detector volume the cleaning is different for the later IceCube configurations. There the HLC condition still has to be fulfilled for pulses used to trigger an event but the pulses not fulfilling the criterion are also reported to the surface. New algorithms for the cleaning of noise hits are developed [Ice10b].

3.2.6 Triggering and Event Building

The DOMs report the measured pulses after the HLC cleaning to the surface computer center. This data is recorded if one of several trigger conditions is fulfilled. The relevant triggers for this analysis are:

- If eight DOMs record a pulse within $5\,\mu$s, the so called simple multiplicity trigger (SMT-8) is issued. This is a general purpose trigger keeping huge amounts of data. It rejects only small events most probably caused by noise hits or extremely low energetic atmospheric muons.

- If five DOMs out of seven in a row on one string record a pulse with time differences less than $1.5\,\mu$s and no pulse is recorded in the upper most three DOMs (StringTrigger-5). This trigger selects vertically up or down-going events with low energies.

- If three DOMs in a row on one of four central strings (figure 24) record pulses with time differences less than $1.5\,\mu$s and no pulse is recorded in the uppermost 38 DOMS (StringTrigger-3). This trigger retains ultra low energetic events in the deep ice.

Further triggers are issued in calibration runs and for combined events of AMANDA and IceCube. The current analysis aims for lower energetic events from the direction of the Galactic Center. Thus, the string triggers retain only nearly vertical tracks and are not used for this analysis. Thus, all data has to pass the SMT-8.

Table 3: Overview of Neutrino Telescopes. The types are: w.c. for water Cherenkov detector , i.c. for ice Cherenkov detector and o. for other techniques. The units of the volume, the energy threshold $E_{\min}$ and the overburden are km^3, GeV and kmw.e., respectively. The volume column gives only the order of magnitude of the size. ^{a}: the values refer to DeepCore without the rest of IceCube, ^{b}: values from [LM00], ^{c}: depth of the see.

detector	volume	type	overburden	year	location	ref.
BNO	10^{-6}	o.	0.7	80 -	Baksan, Kz.	[A$^+$87b]
IMB	10^{-5}	w.c.	1.6	81^b -	Lake Erie, US	[IMB93]
MACRO	10^{-5}	o.	3.1	95^b - 00	LNGS, I.	[MAC02]
DUMAND	1	w.c.	4.8	-	Hawai,US	[L$^+$81]
LVD	10^{-5}	o.	3.6	96^b -	LNGS, I.	[LVD89]
Baikal	10^{-4}	w.c.	1	96^b -	Lake Baikal, Rus.	[Bai90]
AMANDA	0.02	i.c	2	96 - 09	South Pole	[AMA91]
Super-K.	10^{-4}	w.c.	2.7	96^b -	Kamioka, J.	[Sup03]
Borexino	10^{-6}	o.	3.5	97 -	LNGS, I.	[Bor09]
SNO	10^{-6}	w.c.	5.9	99^b -	Sudbury,Ca.	[SNO00]
ANTARES	0.03	w.c.	2.5^c	06 -	Toulon, F.	[ANT99]
IceCube	1	i.c.	2	05 -	South Pole	[Ice]
+DeepCore	0.025^a	i.c.	2.6^a	10^a -	South Pole	[Ice10b]
NESTOR	-	w.c.	3.5^c	-	Pylos, Gr.	[NES05]
NEMO	-	w.c.	3.5^c	-	Capo Passero, I.	[NEM09]
KM3Net	> 1	w.c.	$> 4^c$	-	-	[KM308]

Each time a trigger is issued the pulses which fulfill the HLC criterion between the first and the last of the triggering pulses are stored as one event. All pulses 5 μs before the first and after the last triggering pulse are added. These pulses are kept as one event for all further reconstructions and analyses.
Due to the huge amount of atmospheric muons the SMT-8 is initiated with a rate of about 1 kHz. All triggered events are stored on tape. This results in approximately 300 GB/day for IC40.

3.3 Further Neutrino Telescopes

During the last decades several experiments have been built and used as neutrino telescopes, each aiming at a special energy range or part of the sky. Table 3 gives an overview. In the 1960s the Homestake experiment was the first to measure extra-terrestrial neutrinos: the flux of neutrinos from the Sun [C$^+$98]. Later on, in 1987 IMB, Kamiokande-II and Baksan detected neutrinos (MeV energies) from the supernova 1987A and were the first to observe neutrinos from outside our solar system [B$^+$88],[H$^+$88],[A$^+$87a]. These observations were the beginning of neutrino astronomy.
Today, neutrino astronomy is a well established field. Various detectors search for neutrinos from the atmosphere, from the sun or from supernovae. These detectors are usually sensitive to neutrinos at energies above several MeV (e.g. SNO [SNO00], Borexino [Bor09], LVD [LVD89], BNO [A$^+$87b], Super-Kamiokande [Sup03], MACRO [MAC02]).

These detectors are also sensitive to neutrinos with higher energies than the MeV scale. Due to the lower expected neutrino flux at high energies the relatively small volumes limit their detection capabilities. Above energies of about 100 GeV large Cherenkov telescopes take over. Their technique is similar to IceCube and neutrinos up to EeV energies can be observed.
The development began in the late 70's with Baikal [Bai90] and DUMAND [L$^+$81]. Today, this technique is well established and used by three operating experiments: Baikal, ANTARES [ANT99] and IceCube [Ice]. Additionally, AMANDA [AMA91] was operated until 2009 and decommissioned after 13 years of successful operation. The experiment has measured atmospheric neutrinos up to a few 100 TeV [Ice09a] and has set today's best limits on the flux of various astrophysical sources [Ice07][Ice09e]. (See [Ice09f] for a list of detected neutrino events.)
ANTARES [ANT99] is located in the Mediterranean sea. Additionally, the NESTOR [NES05] and the NEMO experiment [NEM09] test techniques to detect neutrinos in the see. A consortium consisting mainly of the institutions working on these experiments in the Mediterranean sea is proposing a 1 km^3 scale detector in a combined effort. It is called KM3Net. The conceptual design report was published in 2008 [KM308].
With KM3Net and IceCube two neutrino telescopes on the 1 km^3 scale will cover the complete sky. IceCube observes the Northern sky and KM3Net has its best sensitivity on the southern hemisphere. With the DeepCore [Ice10b] sub-detector and due to the rotation of KM3Net with the Earth both experiments are also sensitive in the regions preferred by the other telescope.

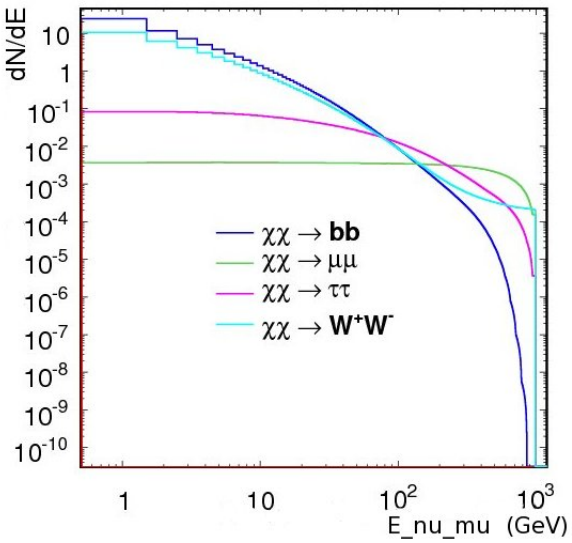

Figure 17: Average Muon Neutrino energy distribution at the Earth for different annihilation channels of one pair of Dark Matter particles with mass 1 TeV. Shown are distributions assuming a complete annihilation into only $b\bar{b}$, $\tau^+\tau^-$, $\mu^+\mu^-$ and W^+W^- (dark to bright gray). Data derived with DarkSUSY [G+04].

4 Signal Hypotheses and Analysis Technique

This chapter summarizes the possible neutrino signals, which have already been introduced in chapter 2. It concentrates on the details of the signatures at which this analysis aims. The second part of this chapter describes the analysis strategy.

4.1 Cosmic Neutrino Signals

This analysis is the first approach using IceCube to search for neutrino sources in the southern hemisphere at energies below the PeV scale. Analyses at energies above have been performed [Dum09][Ice09b][Fra07]. The current work is based on the identification of starting neutrino induced events. It focuses on one region in the sky to develop and test methods. In the future the full IceCube detector including DeepCore will easily improve this analysis (chapter 9) and studies covering a larger part of the southern sky will be performed.

The selected region lies in the direction of the Galactic Center, because it is one of the most interesting regions. It allows a search for two signal types. As discussed in section 2.3.5 high energetic gamma rays have been observed from this direction. This signal hypothesis is considered as a point-like source and is further discussed in section 4.1.2. Additionally, neutrinos could be produced by Dark Matter particles annihilating in the galactic halo (section 2.4.2). The treatment of this hypothesis is discussed in the following section.

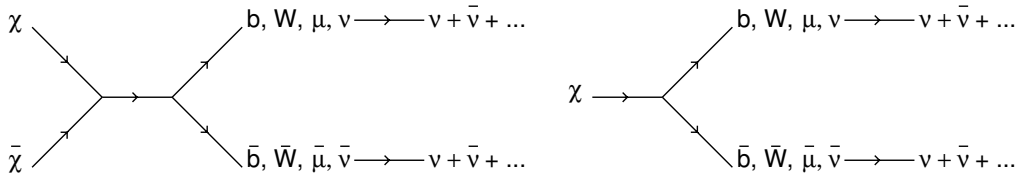

Figure 18: Schematic view of the annihilation (left) and decay (right) of Dark Matter particles χ. The details of these processes depend on the realized theory. The investigated output channels $b\bar{b}$, W^+W^-, $\mu^+\mu^-$, $\nu\bar{\nu}$ produce neutrinos ν, $\bar{\nu}$ and further particles in the final state.

4.1.1 Neutrinos from Dark Matter in the Galactic Halo

In section 2.4.3 the neutrino flux produced by Dark Matter particles decaying or annihilating in the Galactic halo is discussed. In the following this analysis focuses on the annihilation of Dark Matter particles in the following. However, also results for the decay of Dark Matter can be inferred. Equation 20 predicts the amount of neutrinos arriving at the Earth. The energy distribution of these neutrinos is unknown since Dark Matter particles may have different masses and various annihilation products are possible.
Four characteristic annihilation channels are investigated (figure 18):

- The $b\bar{b}$ channel produces the neutrinos with the softest energy spectrum.
- The $\mu^+\mu^-$ channel produces the neutrinos with the hardest energy spectrum initiated by a leptonic process.
- The W^+W^- channel produces the second hardest neutrino energy spectrum. This is the channel with the hardest energy spectrum for a hadronic process. For annihilations in the Sun or the Earth the $\mu^+\mu^-$ channel is suppressed, because the muons would interact before they can decay into neutrinos.
- The $\nu\bar{\nu}$ channel produces a line energy spectrum at the energy of the Dark Matter particle mass. No further decay processes are involved. Super-symmetric theories predict this channel to be suppressed by several orders of magnitude. It is included as model independent expectation for the hardest possible energy spectrum.

All four channels assume the annihilation of Dark Matter pairs into exactly one final state of Standard Model particles. Standard model interactions determine, how these particles decay further, and the resulting energy spectrum of the produced neutrinos. Since neutrinos oscillations occur on the way to the Earth, all three neutrino flavors have to be considered. For the neutrino flux at the Earth maximal mixing is assumed because distributions from huge distances dominate. One third of all arriving neutrinos are muon neutrinos. The energy distributions for the $b\bar{b}$, $\mu^+\mu^-$ and W^+W^- channel are derived using the DarkSUSY simulation package [G$^+$04] (figure 17). For the $\nu\bar{\nu}$ channel the energy distribution is a delta function.
The $b\bar{b}$ and the $\mu^+\mu^-$ annihilation channels generate the flux with the most and the least high energetic neutrinos at the Earth. Any other energy spectrum predicted by

annihilations into exclusively Standard Model particles will produce a flux of high energetic neutrinos with an energy distribution between these two channels. Since IceCube is more sensitive for higher energies, $b\bar{b}$ and $\mu^+\mu^-$ represent the most pessimistic and the most optimistic case, respectively. The sensitivity of IceCube for all other annihilation channels or combinations of annihilation channels then lies between the bounds set by these two channels. This covers all possible choices of the parameters in super-symmetric theories or Kaluza-Klein theories.
Additionally, the expected neutrino energy spectrum depends on the Dark Matter particle mass. This analysis tests Dark Matter particle masses m_χ from the highest values predicted by theory (about 10 TeV) to the lowest energies which IceCube can measure (about 100 GeV). The energy spectra used here are determined with DarkSUSY and the calculations had to be done for discrete masses: 100 GeV, 200 GeV, 300 GeV, 500 GeV, 700 GeV, 1 TeV, 2 TeV, 5 TeV, 10 TeV. Results for Dark Matter particles with a mass in between the tested masses are interpolated.
Dark Matter particles with higher mass produce neutrinos of higher energies when annihilating and this increases the IceCube sensitivity for the signal. However, resonances could lead to differences in the neutrino energy spectra. These are not considered. For this reason the obtained results are only estimates.

4.1.2 Galactic Center as a TeV Neutrino Source

This analysis searches for a point-like source in direction of the Galactic Center. As discussed in section 2.3.5 several potential sources exist in this direction. For this analysis all of them are treated as a single point-like source. Their angular distances are below 1°. This is below the angular resolution of IceCube (using events below 1 PeV).
The expected neutrino flux (equation 12) follows a power law with a cut-off: It is characterized by the spectral index γ and the cut-off energy E_{cut}. Both parameters are correlated to the properties of the source. The expectation for the spectral index is $\gamma \approx 2$ for sources with Fermi acceleration (section 2.3.2). Due to different observed power law indices in the observed γ-ray fluxes this analysis tests power law indices between 1.5 and 2.5.
The energy cut-off E_{cut} is varied over the complete range from 100 GeV to 1 PeV. The maximum value is given by the IceCube search for high energetic neutrinos from the southern hemisphere [Ice09b]. This analysis uses only high energetic events and it is sensitive above 1 PeV. The amount of muons produced by air showers decreases rapidly with increasing energy and within the considered energy range it is not necessary to identify starting tracks. The analysis using all tracks is more sensitive above 1 PeV. Therefore, this energy range is not tested in this analysis. The minimum tested value for the cut-off energy is 100 GeV. This is about the lowest neutrino energy IceCube can detect (section 3.2).

4.2 Analysis Strategy

The Galactic Center is a spot in the sky. Due to the angular resolution and the Dark Matter distribution, signal events are expected from a region around this spot. It is advantageous to split the recorded data into two parts based on the reconstructed direction: one part contains events which might originate from the source (on-source region) and one part has no expected signal events (off-source region). The amount of background events expected

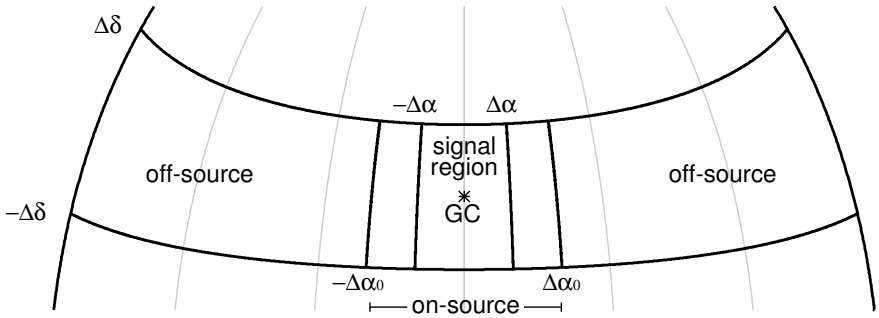

Figure 19: Sketch of the on- and the off-source region, as well as the signal region. The width of all regions in declination is given by $\Delta\delta$. The width of the signal region in right ascension is $\Delta\alpha$.

in the on-source source region is then predicted from the events in the off-source region. This prediction has no systematic errors due to uncertainties in the background simulation.

Figure 19 shows a sketch of the on- and the off-source region. The on-source region is placed around the direction of the Galactic Center. In this on-source region a smaller signal region is chosen. The size of this signal region is optimized in order to achieve the best sensitivity to each signal hypothesis (section 7.1). The events in the remaining part of the on-source region are not used at all. Including them into the signal region would not result in an optimal sensitivity. Due to a possible signal contribution the data can not be used for the background prediction either.

The dominant background are atmospheric muons. Their rate has a strong dependency on the zenith angle which is equivalent with the declination for an experiment at the South Pole. To predict the amount of background events in the signal region $N_{\mathrm{sig}}(BG)$ from the off-source region, they have the same width in declination $\Delta\delta$. The size of the off-source region in right ascension is given by the distance to the Galactic Center where no signal events are expected. For all hypotheses the signal decreases by a factor 0.01 or more at an angular distance of $\Delta\alpha_0 = 20^\circ$ in right ascension. The amount of background events in the signal region (assuming a flat distribution in right ascension) is given by:

$$N_{\mathrm{sig}}(BG) = N_{\mathrm{off}} \frac{\Delta\alpha}{180^\circ - \Delta\alpha_0} \,. \tag{34}$$

N_{off} is the amount of events in the off-source region and $\Delta\alpha$ is the size of the signal region in right ascension. A more detailed calculation, which takes the exposure for different directions into account, is presented in section 7.2. The search region is not rectangular but narrows towards the South Pole due to the definition in spherical coordinates. The selected bin shape is based on the expected signal and background distribution. As shown in figure 25 the amount of background is expected to increase drastically towards vertical events from above. Thus, the background distribution favors a narrower signal region towards the pole. However, the signal decreases for larger angular distances to the Galactic Center. This favors a spherical signal region. The ideal solution is a compromise shape in between these two.

To take both constraints into account and to keep the definition of the signal region as simple as possible, the nearly rectangular region with a half width $\pm\Delta\delta$ in declination and a half width $\pm\Delta\alpha$ in right ascension is chosen. The spherical symmetry is considered by

$$\sin^2(\theta_{\mathrm{GC}})\cos(\Delta\alpha) + \cos^2(\theta_{\mathrm{GC}}) = \cos(\Delta\delta) \tag{35}$$

the equation for angular distances in spherical coordinates. It ensures an equal angular width in declination and right ascension at the declination of the Galactic Center θ_{GC}. The bin is wider towards the equator and narrower towards the South Pole. This takes into account the background distribution and approximates the ideal shape of the signal region.

5 Reconstruction of Muon Tracks

Muon tracks are reconstructed from the light measured by the DOMs of the IceCube detector. The reconstructed quantities are the direction of the muon, the event time, the energy, the position of the neutrino interaction vertex and the track length. However, for most analysis tools an infinite muon track length is assumed. Thus, the interaction vertex is not reconstructed and the determined position is just an arbitrary point on the track. In the following, several techniques are presented which are used within the IceCube collaboration to reconstruct these quantities.

The search for neutrinos from sources in the southern hemisphere is a new challenge for IceCube. As discussed in section 3.1.3 it is important to identify whether the muon track starts inside the detector or outside and to reconstruct the interaction vertex. On average events which start inside the detector cause less hits in the DOMs, because these events are only visible in a part of the detector. With less hits the reconstruction is usually less accurate.

This chapter describes the reconstruction tools used in the present analysis for muon tracks. This includes tools which are appropriate for infinite tracks as well as newly developed tools for the reconstruction of neutrino events interacting inside the detector. The tools for infinite tracks are reviewed concerning their application to muons which start in the detector. The tools for muon tracks which start and stop inside of IceCube are part of the 'finiteReco' project [Hue] of the IceCube software framework. These are the reconstruction of the interaction vertex and the stop point (section 5.1.2) and the P_{hit}-P_{noHit} likelihood function (section 5.3). Both are based on the hit pattern.

5.1 Initial and Pattern Based Reconstruction

The initial reconstruction algorithms determine the properties of a muon track by geometrical calculations based on the times and the positions of the measured hits. They do not use an iterative procedure. Therefore, these algorithms are relatively fast, but they usually have larger uncertainties in the reconstructed quantities. Many different approaches are implemented and tested within the IceCube collaboration. However, in data processing only the so-called LINEFIT is used, which is discussed in detail in the following sub-section.

5.1.1 LINEFIT Reconstruction

The LINEFIT algorithm [Ste90] is used to do an first reconstruction of the direction and the position of muon tracks based on the hits measured in the DOMs. It ignores all physical processes and assumes light traveling with velocity v_0 along a straight line through the detector. In this description the position of DOM i with a recorded hit is given by:

$$\vec{r_i} = \vec{r_0} + \vec{v_0} \cdot t_i \ . \tag{36}$$

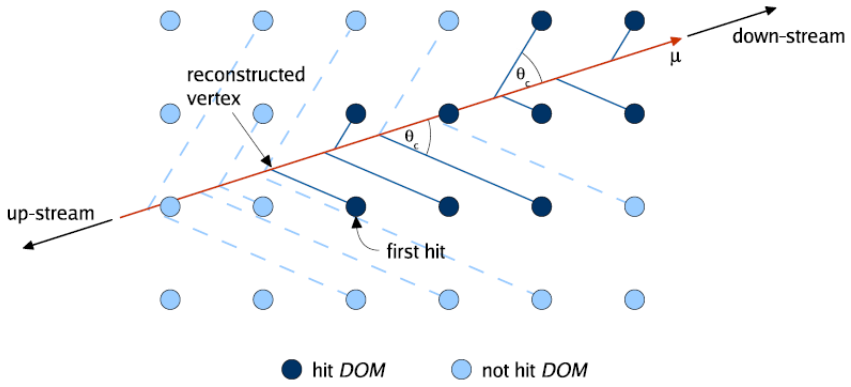

Figure 20: The interaction vertex is reconstructed by the projecting each DOM along the path of Cherenkov light onto the muon track. θ_c is the Cherenkov angle. Figure from [Eul08].

t_i is the time when the hit is recorded. The algorithm is based on the correlation between the time of the hit and the position of the DOM relative to the path of the light. A χ^2 can be minimized analytically to determine the offset $\vec{r}_0$ and the velocity $\vec{v}_0$

$$\chi^2 = \sum_{i=1}^{N} |\vec{r}_i - \vec{r}_0 - \vec{v}_0 \cdot t_i|^2 \ . \tag{37}$$

This minimization yields the solutions

$$\begin{aligned} \vec{v}_0 &= \frac{< \vec{r}_i t_i > - < \vec{r}_i >< t_i >}{< t_i^2 > - < t_i >^2} \ , \\ \vec{r}_0 &= < \vec{r}_i > - \vec{v}_0 \cdot < t_i > \ . \end{aligned} \tag{38}$$

The $<$ .. $>$ brackets denote the calculation of the unweighted mean using all N hits recorded for the event. The position of the track is given by $\vec{r}_0$ and the direction by the velocity $\vec{v}_0$. The absolute value of the velocity $|\vec{v}_0|$ describes the propagation speed through the detector. For a high energetic muon traveling through the detector the value of $|\vec{v}_0|$ is expected to be about the speed of light. For cascade-like events smaller velocities are expected due to the spherical emission of light from approximately one fixed position. For tracks with an interaction vertex or stop point in the detector the algorithm works identically. Since there are less hits recorded in this case, reconstruction uncertainties are larger.

5.1.2 Interaction Vertex and Stop Point

The LINEFIT algorithm estimates the most basic track parameters (overall position and direction). Muon tracks caused by neutrinos may start and stop in the detector volume and also an initial estimate of these positions is required. This estimate requires a given geometrical reconstruction of the direction and the overall position. It uses the geometrical position of the hit DOMs. The algorithm is called 'StartStopPoint'.

The position of each DOM with a recorded hit is projected along the path on which a Cherenkov photon would have directly propagated (see section 3.1.1 and figure 20) onto the muon track. For each DOM one position on the track is determined. The most upstream position is returned as an estimate for the interaction vertex and the most downstream position as an estimate for the stop point. The distance between both is the reconstructed track length L_{finite}.
This reconstruction neglects scattering and has a limited precision. The true position of both positions, the interaction vertex or stop point, could be father upstream or downstream compared to the reconstructed positions. In addition to this limited precision, the algorithm could underestimate the true length due to the spacing of the DOMs and strings. The muon can travel some distance before the first or after the last position without being noticed. The light emitted on these parts of the track might not hit any DOM.
This reconstruction is intended for neutrinos interacting inside of IceCube. In this case, photons from the initial hadronic cascade are also recorded. If hits caused by photons from cascades are projected onto the track assuming Cherenkov light, the estimated interaction vertex is placed to far upstream and the reconstructed length is overestimated.
Besides these effects also the dependency on the accuracy of the used initial track reconstruction has to be kept in mind. A poor geometrical reconstruction of the track position and direction results in large reconstruction errors for the interaction vertex and the stop point position.

5.2 Likelihood Algorithms

The general principle of the likelihood reconstruction is to maximize the probability (likelihood value) that an assumed muon track, given by a set of parameters $\vec{a}$ (direction, position, energy, time, length), caused the measured hits. The best fitting muon track is determined in an iterative process beginning at an initial muon track. This starting value or seed is determined with a less precise algorithm. The required computation time for iterative likelihood reconstructions is usually large. The advantage is a more accurate reconstruction result.
A probability density function (pdf) is required to determine the probability P for an assumed muon track. This pdf is constructed from pdfs p_i for the hits in each DOM. Since the DOMs act independently the overall probability is given by:

$$L(\vec{a}) = \prod_{i \epsilon I} p_i(\vec{a}) \; . \tag{39}$$

I is a subset of the DOMs that can differ between different reconstructions. p_i describes the probability that a hit is registered in DOM i. It depends on the position of DOM i in the ice and on the distance to DOM i and the muon track. Several tools have been developed for the reconstruction of muon tracks. They have been adapted for the present work that focuses on the following tools: Single Photo Electron (SPE) likelihood function, Multi Photo Electron (MPE) likelihood function and a total hit probability based likelihood function (P_{hit}-P_{noHit}). All these algorithms have advantages and drawbacks. The SPE and MPE method are introduced in the following subsections, the method based on the total hit probability is discussed in section 5.3 in more detail. This is a recently developed technique to include the interaction vertex into the likelihood reconstruction.

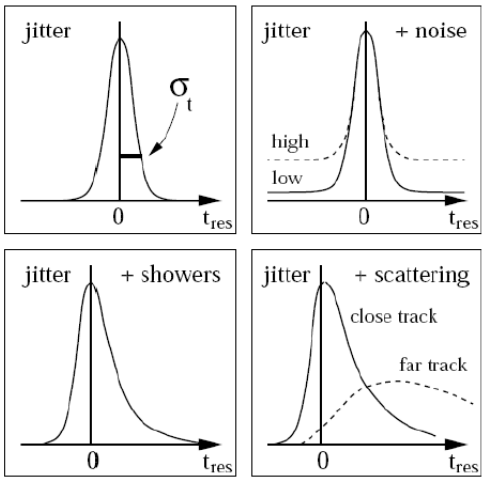

Figure 21: Schematic time residual distributions including different effects: only jitter (upper left), jitter and noise (upper right), jitter and photons from particle showers due to stochastic energy losses of the muon (lower left) and jitter and scattering (lower right). Figure from [AMA04].

5.2.1 Single Photo Electron Likelihood Function

The Single Photo Electron (SPE) likelihood function determines the probability for a hit in each DOM by using the arrival time of the first recorded hit and the relative position of the DOM to the assumed muon track. The measured arrival time is compared to the expected arrival time, which is determined by geometric arguments assuming direct Cherenkov light propagation (figure 20). In the ideal case the pdf for the time residual Δt_{res} is a delta function

$$p_i(\Delta t_{\text{res}}) = \delta(\Delta t_{\text{res}}) \; . \tag{40}$$

A more realistic approach takes into account electronic jitter, noise, showers and scattering in the ice. Figure 21 shows the effect on the time residual distribution.

- Electronic jitter could lead to a small offset in the recorded arrival time. This widens the the time residual distribution. It can be described by a Gaussian distribution with width σ_t.

- Noise hits included in the event are uncorrelated to the muon track. Thus, their arrival time has a uniform distribution. This causes a offset in the time residual distribution.

- Cherenkov photons produced by stochastic losses and brems photons (section 3.1.2) arrive later at the DOMs than unscattered Cherencov photons directly from the muon. Therefor, the time residual distribution has a longer tail to larger times.

- All photons are delayed by scattering in the ice. The impact of scattering also depends on the distance between the DOM and the muon track d. At larger distances the time residual distribution becomes wider and the mean is shifted to later times.

The time residual distribution $p(\Delta t_{\text{res}})$ without jitter and noise is described reasonably well by the so called Pandel function [Pan96], which is a Γ-distribution

$$p_{\text{SPE}}(t_{\text{res}}, d) = \frac{1}{N(d)\Gamma(d/\lambda)t_{\text{res}}} \left(\frac{t_{\text{res}}}{\tau}\right)^{d/\lambda} \exp - \left(t_{\text{res}} \left(\frac{1}{\tau} + \frac{c_{\text{ice}}}{\lambda}\right) + \frac{d}{\lambda_a}\right) , \tag{41}$$

$$\text{where } N(d) = e^{-d/\lambda_a} \left(1 + \frac{\tau c_{\text{ice}}}{\lambda_a}\right)^{-d/\lambda} .$$

is a normalization constant, λ_a is the attenuation length and c_{ice} the speed of light in ice, λ and τ are free parameters. Γ is the Gamma function. The attenuation length is kept at a fixed value. Thus, only average ice properties can be used. This distribution is convoluted with a Gaussian distribution with a width given by the jitter and a flat distribution for the noise to include both effects. The parameters of these two distributions are determined for each DOM in dedicated calibration runs.
This pdf is sensitive to the geometry of a track hypothesis via the time residuals. The direction and the overall position in the detector can be determined when maximizing L with respect to these parameters. In a single event more than one hit can be recorded for each DOM. By convention only the first hits are used and the vertex times tend to be underestimated. Information of further hits is not taken into account. The algorithm is not sensitive to the position of the interaction vertex or a stop point. For this reconstruction method a muon which starts or stops in the detector simply appears as an event with fewer usable hits. This reduced information can result in a poorer directional precision.

5.2.2 Multi Photo Electron Likelihood Function

The Multi Photo Electron likelihood function (MPE) is a more advanced version of the SPE likelihood function. It includes not only the information of the first hit in the pdf but also the number of measured photo electrons N_{pe}. The arrival time of each photo electron can be described by the function p_{SPE} (equation 41). Therefore, the MPE likelihood uses the probability

$$p_{\text{MPE}}(t_{\text{res}}, d, N_{\text{pe}}) = N_{\text{pe}} \cdot p_{\text{SPE}}(t_{\text{res}}, d) \left[\int_{t_{\text{res}}}^{\infty} p_{\text{SPE}}(t, d) dt\right]^{N_{\text{pe}}-1} \tag{42}$$

for the first out of N_{pe} photo electrons to arrive at the measured time residual t_{res}. This pdf recovers some of the drawbacks of the SPE approach. Its general capability to reconstruct direction and position is similar or better at high energies. The comparison of angular reconstructions is discussed in appendix B in more detail. For events caused by high energetic muons the results of the MPE fit is usually better than the SPE. Events producing a small amount of light tend to have only one photo electron per DOM and no improvement is achieved. The main advantage of the MPE fit is the more accurate reconstruction of the vertex time.

5.3 The P_{hit}-P_{noHit} based Reconstruction

The reconstruction algorithms discussed above are mainly based on the arrival times of the hits. Additionally, the geometrical distribution of DOMs with hits within the detector (hit

pattern) is used in the so called P_{hit}-P_{noHit} approach. The hit pattern is independent of the measured times and depends on the distance of the DOMs to the track. This approach is particularly useful for muon tracks with an interaction vertex or stop point inside the detector. In addition to the sensitivity to the position and the direction of a muon track, the hit pattern is also sensitive to the position of the interaction vertex and the stop point.

5.3.1 The P_{hit}-P_{noHit} Likelihood Function

The likelihood function for the P_{hit}-P_{noHit} approach is given by the probability to observe at least one hit in a certain DOM. This probability depends on various effects: the distance between the muon track and the DOM, the orientation of the DOM, the ice properties and the readout logic. The dependency on the distance between DOM and the muon track allows to determine the track parameters. Therefore, the ice properties and the readout logic have to be included as accurately as possible.
For a given muon track with parameters $\vec{a}$ the expected number of detected photons N_p at a certain DOM is determined. This is discussed in detail in the next section. Due to Poisson statistics the probability for at least one hit in the DOM caused by the track p_{hit} is given by:

$$p_{hit}(\vec{a}) = 1 - p_{noHit}(\vec{a}) = 1 - e^{-N_p(\vec{a})} \; . \tag{43}$$

Additionally, a noise hit can be recorded by the DOM depending on the noise rate r_{noise} (fixed value). The probability that a DOM records either a signal hit or a noise hit is given by:

$$p_{hit}(\vec{a}, r_{noise}) = p_{hit}(r_{noise}) + p_{hit}(\vec{a}) - p_{hit}(r_{noise}) p_{hit}(\vec{a}) \; . \tag{44}$$

The probabilities for all DOMs are combined into the overall likelihood function:

$$L(\vec{a}) = \prod_{i \epsilon H} \left[p_{hit,i}(\vec{a}, r_{noise}) \right] \prod_{i \epsilon M} \left[1 - p_{hit,i}(\vec{a}, r_{noise}) \right] \; . \tag{45}$$

H and M are the DOMs with a recorded hit and without, respectively. The likelihood $L(\vec{a})$ is particularly sensitive to the interaction vertex and the stop point of a muon track. Hits are expected along a muon track but not before the interaction vertex or after the stop point. Only if a DOM is close to the assumed muon track it has a large probability p_{hit} to record a hit. Hits close to the neutrino track or after the stop point reduce the likelihood value.
This likelihood function has to be modified due to the operation mode of the IceCube detector. The IceCube detector is operated with hard local coincidence (HLC, section 3.2.5) to reduce the noise rate. HLC discards all hits in DOMs with no hit in one of the four neighboring DOMs on the same string (section 3.2.5). The probability for a recorded hit in a DOM depends on its neighbors and their probability to record a hit. This is taken into account by replacing the equation above by:

$$L(\vec{a}) = \prod_{i} p_{string,i}(\vec{a}, r_{noise}) \; . \tag{46}$$

$p_{string,i}$ is the probability for the hit pattern observed on one complete string. It is calculated from the hit probabilities $p_{hit}(\vec{a}, r_{noise})$ given by equation 44. Details of the algorithm are described in appendix A. The probabilities for no hits in the not hit DOMs are considered as well as the probabilities of the hit DOMs.

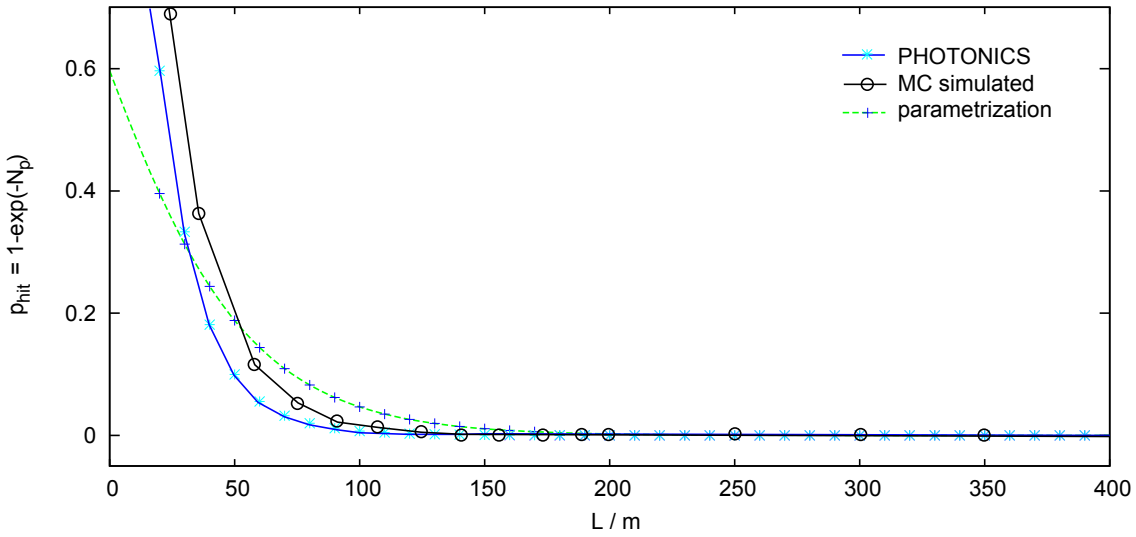

Figure 22: Probability for a hit $p_{\text{hit}}(\vec{a})$ in dependence of the distance to the track, determined by different methods. Blue Line (solid): N_p determined with the PHOTONICS tables from a vertical muon track in the center of IceCube; Green Line (dashed): N_p determined with the parametrization (equation 41); Black Line (solid with circles): p_{hit} determined with Monte Carlo simulations.

5.3.2 Number of Expected Photons at a DOM

The above calculation relies on the determination of the expected number of detected photons N_{p}. This number depends on the distance between the DOM and the assumed muon track, the orientation of the DOM and on the ice properties. Two approaches can be used to calculate N_{p}.

The first approach to determine N_{p} is based on Monte Carlo (MC) simulations. For simulated events the fraction of DOMs with at least one hit at a certain distance d is calculated. This fraction is directly used as probability for a hit p_{hit} and avoids the determination of the number of photons. This distribution is averaged over all possible positions and directions of the muon track in the detector. The differences in the ice properties are smeared. The drawbacks of this method are its dependency on Monte Carlo parameters, its limited statistics and the use of averaged ice properties.

The second algorithm uses PHOTONICS [L$^+$07]. PHOTONICS contains a huge set of tables parametrizing the propagation of photons in the ice. It uses a model with depth-dependent ice properties. For a given muon track and DOM position the number of expected photons can be obtained from these tables. Here, a minimal ionizing muon is assumed to avoid a dependency on the energy reconstruction. This method is more precise than the two presented above. Its drawbacks are a large memory requirement (at least 1 GB) and longer computation times (factor of about two).

Figure 22 shows the the probability for a hit $p_{\text{hit}}(\vec{a})$ in dependence of the distance to the muon track. The probability decreases rapidly with the distance to the track. The difference between PHOTONICS and the MC simulation is explained by the use of local or averaged ice properties. Additionally, figure 22 shows a hit probability based on a parametrization. Here, the normalization N_{d} in equation 41 is used. This has no physical

or mathematical motivation and the probabilities differ significantly. It is used only for tests of the algorithm.
Both algorithms determine the number of expected photons and thus the probability for a hit without consideration of the energy. This avoids dependencies on the energy reconstructions, but in general this is to simple. The chance for a hit increases with the energy. Future algorithmic improvements will also take the energy dependence into account. However, the current analysis is focused on low energetic neutrinos ($< 1TeV$), which induce even lower energetic muons. These are in good approximation all minimally ionizing ($< 600\,\mathrm{GeV}$) and the energy dependency vanishes. Additionally, the increase of the hit probability is radial symmetric around the muon track. Thus, all hit probabilities are underestimated in a similar manner and the likelihood function is basically scaled. The parameters $\vec{a}$ minimizing the likelihood function are therefore less affected.

5.3.3 Reconstruction with the $\mathbf{P_{hit}}$-$\mathbf{P_{noHit}}$ likelihood

The P_{hit}-P_{noHit} likelihood can be used to reconstruct the direction and the position of a muon track including the interaction vertex and the stop point. The likelihood fit does not determine whether an event is caused by a through going muon or a neutrino interacting inside. It only determines the parameters of the seeded track. Another algorithm has to be used to identify the track properties.
If the interaction vertex and the stop point are reconstructed, the parameter space is increased. In comparison to the reconstruction of a through going muon, the degrees of freedom of the likelihood fit are increased by two: the interaction vertex substitutes the vertex of the thoroughgoing muon (one additional degree of freedom, because the interaction vertex is not free to shift along the track) and the stop point is given by the length of the track (one degree of freedom).
The P_{hit}-P_{noHit} likelihood function is independent of the arrival time of the hits in the DOMs. It is, thus, not possible to determine the event time and the sign of the direction. Another drawback is that the distributions are broader for the number of expected photo electrons compared to the time residual distributions used in the SPE and MPE approach. This directly results in a poorer reconstruction precision. Therefore, the P_{hit}-P_{noHit} likelihood is not useful to reconstruct the direction and the overall position. The advantage of the method is its sensitivity to the position of the interaction vertex and the stop point.
Two approaches allow to make use of this sensitivity. Either the reconstruction is done with the SPE or MPE likelihood and the result is used as a seed for the P_{hit}-P_{noHit} likelihood with the positions as the only free parameters or a combined likelihood is used:

$$L(\vec{a}) = L_{\mathrm{SPE/MPE}}(\Delta t_{\mathrm{res}}) \cdot L_{P_{\mathrm{hit}}-P_{\mathrm{noHit}}}(d)^{\alpha} \; . \tag{47}$$

α is a free parameter to adjust the weight of the used likelihood functions to each other. This combination is only possible because the SPE/MPE likelihoods depend on the time information while the P_{hit}-P_{noHit} likelihood depends on the hit pattern, two independent observables.

5.4 Energy reconstruction

Reconstructing the muon neutrino energy is a challenging task. The neutrino is not observed directly. A part of the energy is transferred to the muon and the rest to the

hadronic cascade, which is produced in the interaction. If the interaction occurs outside of the IceCube volume, the hadronic cascade is not observed and only the muon energy loss inside the detector can be measured. It is possible to determine of the neutrino energy in a statistical manner and neutrino energy spectra can be measured by unfolding methods. This analysis does not use any energy reconstruction. This section gives a short overview about available methods.

The muon energy reconstruction is based on the energy loss (equation 30). The loss is proportional to the number of emitted photons. The average energy loss per distance is nearly constant for muons below approximately 600 GeV and increases linearly for higher energies. Thus, for low energetic muons which are created outside of IceCube and which do not stop inside the instrumented volume the energy cannot be determined.

A simple estimator for the energy is the number of DOMs N_{chan} with at least one hit. If more photons are produced, the chance to observe some of them farther away from the track increases. This results in larger values of N_{chan}. Unfortunately, this parameter is also affected by geometrical properties of the track. A track which passes a long distance through the detector has on average a larger value of N_{chan} than one traveling only a short distance within the detector. Additionally the different ice properties are not considered. Similar quantities which are also sometimes used as energy estimator are the number of hits in the event and the amount of deposited light (hits plus amplitude).

A more advanced algorithm for estimating the energy is called MuE [ZC07]. The photon density around the track is parametrized taking scattering and absorption into account. MuE reconstructs the energy deposit along the track. Other methods which include the ice properties based on the PHOTONICS [L$^+$07] tables are also available.

For neutrinos with energies below 600 GeV the energy is reconstructed using the position of the interaction vertex and the stop point. If both are within the detector volume, the length of the muon track is determined. At these energies the length is proportional to the muon energy (equation 30). This method relies on the tools to determine the interaction vertex and the stop point introduced in the current work (section 5.1.2 and section 5.3). It is used to determine the energy resolution of the DeepCore sub-detector [Ice10b].

6 Simulation and Filtering

This chapter explains the processing of the simulated and the measured data used in this analysis. First, the simulated signal and background data sets are described (section 6.1). All simulated and measured events are further processed through the same algorithm chain. This includes the on-line filtering at the pole (section 6.2) as well as reconstruction and event selection (section 6.3).

6.1 Simulated Data

For this analysis four simulated data sets are used, which are based on simulations:

1) Neutrino induced events from the direction of the Galactic center (GC data)

2) Neutrino induced events from the region of the Galactic Center (GCR data)

3) Atmospheric muon events caused by a single air showers

4) Atmospheric muon events with muons caused by two air showers in coincidence

The first two data sets contain neutrino induced events. The GC data set is used as signal simulation for a point-like source, the GCR data set for the neutrinos produced by Dark Matter annihilations.
The third and fourth data set are background data sets. Atmospheric muons are the main source of background events for the downwards direction. These muons can propagate into the deep ice (section 3.2.1). In some cases muons from two independent air showers reach the detector at about the same time and are recorded as one event. About 10% of all triggered air shower events in IC40 are such coincident events. The fourth data set contains events like this.
Simulated signal and background data is generated by a subsequent chain of modularized software tools which are based on Monte Carlo techniques. Each module simulates a dedicated process. The chain has four main steps: the initial generation of muons either from neutrinos or air showers, the propagation of the muons through the detector medium, the propagation of the emitted photons through the ice and finally, the simulation of the detector response. These steps are explained in the following subsections and schematically visualized in figure 23.
Except for the initial event generation all used modules are the same for neutrino and air shower induced events. This allows to test the reliability of the signal (neutrino) simulation based on a comparison between simulated and measured background (muons from cosmic rays).

6.1.1 Neutrino Event Generation

The used neutrino generator is a version of ANIS [GK05] modified to work within the IceCube software framework. Neutrino events are generated with a selected energy spectrum and isotropically within a given angular range. These neutrinos are forced to interact near or inside the IceCube detector. To account for the interaction probability and absorption before reaching the detector, a weighting factor is stored with each event. Due to the small interaction cross sections this procedure is much more efficient than discarding events with

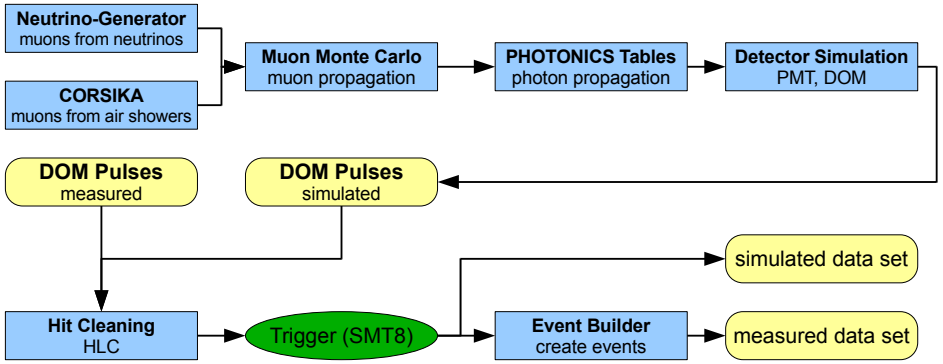

Figure 23: Scheme of the simulation. Blue (rectangular) are algorithms (or groups of algorithms) used in the processing, yellow (rectangular with round corners) are data sets and the trigger is marked in green (elliptical).

Table 4: Parameters of the simulated neutrino data sets for the region of the Galactic center (GCR) and for the spot of the Galactic Center (GC). θ_{GC} is the zenith direction of the Galactic Center. N is the number of generated events

	GC Region	GC
E_{min}	10 GeV	10 GeV
E_{max}	10^9 GeV	10^9 GeV
γ	2	2
θ	$\theta_{\mathrm{GC}} \pm 20°$	$\theta_{\mathrm{GC}} \pm 0.001°$
ϕ	$0° - 360°$	$0° - 360°$
N	10^9	10^9

no interaction or events with interactions far away from the detector. An additional weight factor can be computed which describes the distribution of atmospheric neutrinos. Thus, the data set can be used as a sample of neutrinos from a source as well as a sample of atmospheric neutrinos.
For the two used data sets the minimum neutrino energy in the simulation is 10 GeV. This is roughly the minimum energy for a neutrino to trigger the detector. The highest energy is 1 EeV, well above the highest investigated energies. For the simulated energy distribution a power law ($dN/dE \propto E^{-\gamma}$) is used. With the choice of $\gamma = 2$, the data sets are dominated by low energetic events. The number of events above a given energy E_0 is approximately:

$$N(E > E_0) \approx N \frac{10\,\mathrm{GeV}}{E_0}, \tag{48}$$

where $N = 10^9$ is the number of generated events. For $E_0 = 1\,\mathrm{PeV}$ (the upper bound of the analysis) $N(E > 1\,\mathrm{PeV}) = 10^4$ events are generated. This is a sufficient number taking into account that high energetic events are likely to trigger and pass higher level filters.

The directions of the events are generated according to an isotropic distribution in the considered zenith range. The GC data set contains events from the direction of the Galactic Center ($\theta_{GC} \approx 61°$). The GCR data set covers a zenith range of 40° around the Galactic Center. In the azimuth angle (detector coordinates) all directions are generated. This is necessary to account for the rotation of the detector with respect to the galactic objects. Table 4 summarizes all parameter settings.
The GC data set is used for all point source like signals. Various energy spectra are produced by reweighting the events. The GCR data set is the signal simulation for the Dark Matter annihilation hypothesis. The energy spectrum (section 4.1.1) and the distribution (section 2.4.4) of the Dark Matter are considered by reweighting the events.

6.1.2 Cosmic Ray simulation

Muons produced by cosmic rays are generated with the CORSIKA software package [H$^+$98]. The tool considers direction and position of a cosmic ray and simulates the resulting air shower of particles. The air shower consists of various kinds of particles. Due to the depth of the IceCube detector only muons and neutrinos are able to reach it. These muons can be single muons or bundles of almost parallel muons from one air shower.
The amount of muons which reach the detector strongly depends on their zenith angle. Additionally to the effect of different density layers in the atmosphere, also the amount of matter the muon has to pass before reaching the detector differs: from directly above they have to pass through only about 1.4 km of ice, from the horizon the distance is more than 100 km. The distribution of muons from air showers is maximal from the direction of the South Pole and decreases towards the horizon.
Due to the high rate of these events, muons from two different air showers can reach the detector almost simultaneously; These muons are recorded in one event. In the single air shower events (third data set) the probability for non-coincident events is stored with the simulated data and used to correct for this effect. The fourth data set is produced with events caused by two air showers. This data sets contains weighting factors for the probability that coincident events occur.

6.1.3 Muon Simulation and Photon Propagation

Muons are propagated through the ice by a tool named Muon Monte Carlo (MMC) [CR04] [Chi04]. It takes into account the different processes (section 3.1.2) for energy losses: continuous energy loss is considered as well as stochastic losses of larger amounts of energy. Depending on the process further particles are generated and small particle cascades are initiated.
For all charged particles in the ice the produced Cherenkov photons are calculated. These photons are propagated through the ice. The properties of the photon propagation are summarized in detailed tables. These tables are part of the PHOTONICS [L$^+$07] project. They contain the probability density functions for the photons to arrive at a certain time at a given position in the detector considering absorption and scattering. The content of the tables depends on the measured properties of the antarctic ice [PWC00]. These tables are used in a Monte Carlo process to simulate the number of photons which reach a DOM and their arrival time.

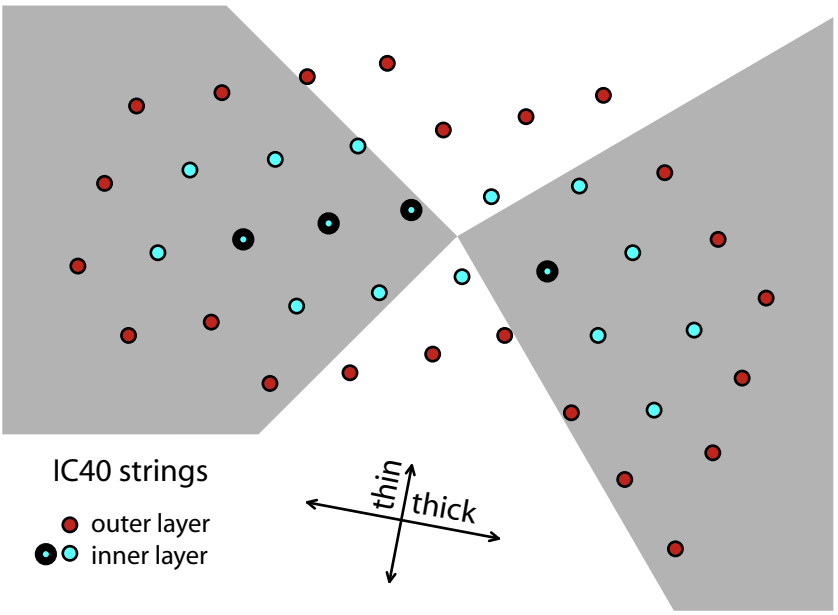

Figure 24: Top view of IC40. Each circle marks the position of one string. The strings marked with red filled circles are part of the outer veto layer of the on-line filter. The gray shaded directions visualize the azimuth angle selections of the on-line filter. The four thicker circles dots mark the strings used for the StringTrigger3 (section 3.2.6).

6.1.4 Detector Simulation

In the detector simulation the response of each DOM to a photon is calculated. The voltage pulses recorded by the PMTs are generated and stored as waveforms. In these waveforms additional pulses from noise are included. The calculation accounts for the individual properties of the DOMs. The output is the analog response of the sensors. Afterwards, the digitization as it is done by the DOMs at the South Pole is applied to the waveform.

The same coincidence criterion (HLC, section 3.2.5) as for the data measured at the South Pole and the same triggers (section 3.2.6) are applied. A major difference is the construction of events. In the simulation, for each initial object (an air shower, two air showers or a neutrino) one event in the detector is generated. This procedure is more complicated for the measured data. A priori, the break between two events is unknown. After the event building, simulated and measured data are treated identically.

6.2 The On-Line Filter at the South Pole

The recorded events at the South Pole are sent to the North via satellite. Additionally, they are stored on tape and shipped in the next austral summer. The triggered data is dominated by events caused by atmospheric muons and the data rate is too high to be completely transferred via satellite. Thus, on-line filters are used to select potential interesting events. These are transferred via satellite, while the complete set is stored on tape. For the analysis of signals from the Galactic Center a dedicated filter has been

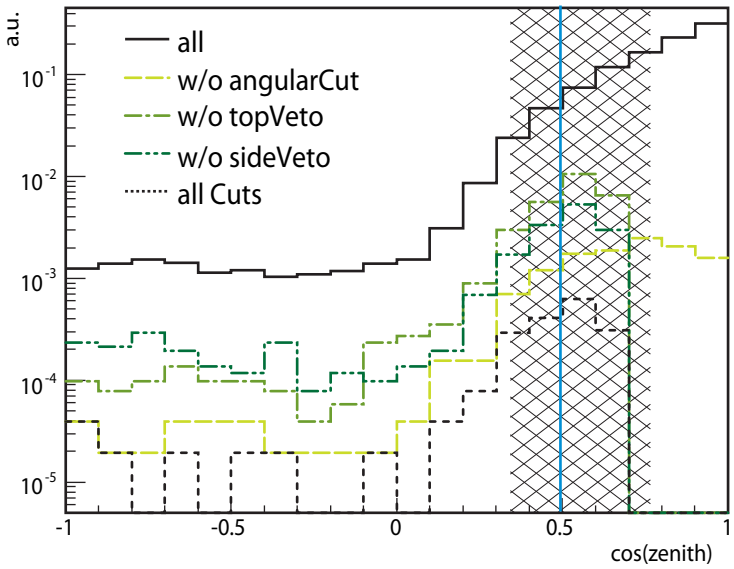

Figure 25: Impact of the different selections of the on-line filter on the background data shown by the distribution of reconstructed zenith angles (SPE Fit). The black solid line includes all triggered events and the black dotted line shows the remaining events after all selections. The green (dashed, dot-dashed and dot-dot-dashed) lines are the distributions for the remaining events if one of the three selections is not applied. The angular selection combines the selection on zenith and azimuth angle. The shaded region shows the directions, which are potentially interesting for this analysis. The Galactic Center position is marked by the vertical blue line.

implemented , which is called 'Starting-Downgoing-Filter'. This is one out of seventeen filters running in the on-line filtering of IC40. The largest amount of data is retained by the so called 'Muon-Filter'. It aims at up-going muon tracks and keeps all events with a reconstructed zenith angle larger than 70°.
Prior to the application of the filtering selection reconstructions of the event direction and position are performed. Therefore, the times and charges of the measured pulses are extracted. Based on these times the direction is reconstructed by a 'SPE likelihood' fit (section 5.2.1) which is seeded with the initial reconstruction of a LINEFIT (section 5.1). An overview of the dependencies of different reconstructions is given at the beginning of section 6.3 in figure 28. The SPE reconstruction is used for the Starting-Downgoing-Filter. The aim of the Starting-Downgoing-Filter is to retain down-going neutrino induced events and particularly these from the direction of the Galactic Center ($\theta_{\mathrm{GC}} \approx 61°$). It concentrates on events in the zenith region around the Galactic Center ($\Delta\theta = |\theta_{\mathrm{GC}} - \theta| < 20°$). Events with zenith angles larger than 70° are also all kept by the muon filter.
The only possibility to distinguish between neutrino and air shower induced muon events is to identify tracks which start in the detector and to remove non-starting events. Therefore, the filter removes all events with:

- a reconstructed zenith angle smaller than 50° or an azimuth angle between 30° and 135° or between 225° and 300° (angularCut),

- at least one hit in the upper 30 DOMs of the IceCube detector (topVeto),

- the earliest hit on one of the strings of the outer layer (sideVeto, see figure 24).

The veto built by the upper 30 DOMs and the zenith angle selection remove down-going muon events with relatively small zenith angles, which are the regions of the largest amount of background events. For the signal from Dark Matter particles annihilating in the halo the selection at 50° seems quite narrow, because it is only 10° away from the direction of the Galactic Center, but it is necessary to achieve the low passing rate required for satellite transmission. For the final analysis additional selections are applied which select a smaller region (section 7.1).
In addition to the veto built by the upper DOMs a rejection of non-starting tracks which enter the detector from the side is also required. Due to the geometry of IC40 (figure 24) it is inefficient to reject all events with a pulse on the strings at the edge of the detector. This would reduce the remaining detection volume significantly. Additionally, less background events are expected in the lower half of the detector compared to the upper half due to a thicker ice shield. Muons entering the detector can cause DOMs on the first string they pass by to generate a pulse. In general, this pulse is the earliest recognized pulse in the event. However, for muons which start inside the detector a pulse on one of the outer strings arrives later. Therefore, all events with the earliest pulse at the edge of the detector are rejected. Signal events are only affected by this selection if additional pulses from noise or an air shower are included in the same event. By chance these pulses can be earlier than the first pulse caused by the muon. If a neutrino event has such a pulse on one of the outer strings, it is lost. For background events with an additional early pulse on an inner string it is the other way around.
The last selection of the filter is based on the geometrical properties of the IC40 detector. It is thicker in one direction and thinner in the perpendicular direction (figure 24). Events which pass the detector in the thin direction can be detected only by a few strings. If the event starts within the detector even less strings have pulses. Therefore, azimuth directions with a thin detector are discarded.
The choice for the azimuth selection was based on the geometrical shape of the detector. This shape is slightly bent and the removed azimuth region is smaller on one side than on the other. This is a non-optimal choice. The detector has approximately the same properties for an event from a certain azimuth direction and an event from the opposite direction. Unfortunately this was discovered after the data taking and could not be changed later. Future on-line filters aiming at the same events are destined differently.
Figure 25 shows the impact of the zenith and azimuth selection, the top veto and the first pulse veto selection on the amount of passing background events. Removing one of these selections increases the amount of passing background events by more than an order of magnitude. The resulting data rate would be too large for the satellite transfer. The given configuration keeps about 0.18% of the triggered events. They produce a data rate of less than 450 MB/day. In comparison the muon filter has an output of about 8500 MB/day. This data is sent to the North via satellite.
Figure 26 (left) shows the impact of the selections on atmospheric neutrino events with zenith angles larger than 40° and an interaction vertex inside the instrumented IC40 volume. Out of these events about 15% survive. This relatively small number is caused by the azimuth selection which removes 50% of the signal and the top veto which removes more than 50% of the effective detection volume: the upper 30 DOMs are 50% of the volume and in addition events right below this veto with only a small amount of light

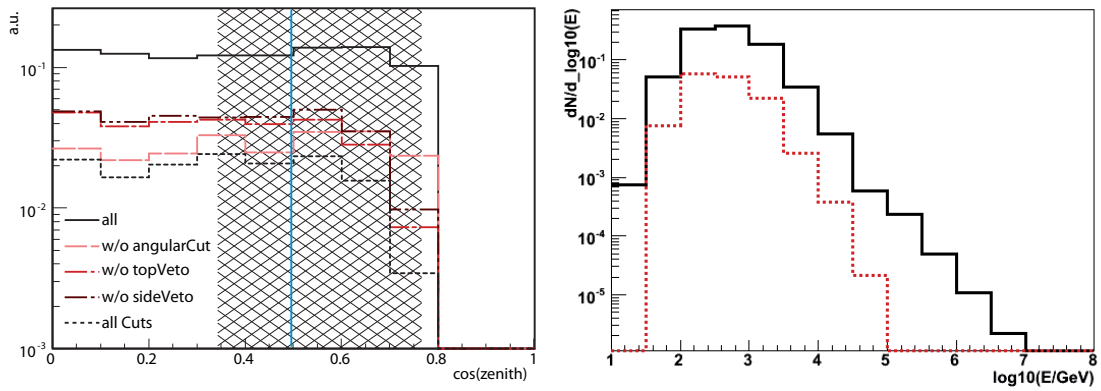

Figure 26: Impact of the different selections of the on-line filter on events originating from atmospheric neutrinos. Left: Distribution of simulated zenith angles. The black solid line includes all triggered events and the black dotted line shows the remaining events after applying all selections. The red lines are the distributions for the remaining background if one of the three selections is not applied. The angular selection combines the selection on zenith and azimuth angle. The shaded region indicates the directions interesting for this analysis. The Galactic Center position is marked by the vertical blue line. Right: the distribution of the simulated energy before (solid black) and after all selections (dotted red).

in the upper part are also rejected. From the events which comply these geometrical constraints about 70% are kept.

Figure 26 (right) shows the amount of passing events versus the energy of the neutrino. The largest passing fraction is achieved in the energy range between 10 GeV and 10 TeV.

On-Line Filter Performance

The Starting-Downgoing-Filter was operated at the South Pole between April 2008 and May 2009. During this time the IC40 detector was operated with an up-time of about 99%. Test runs, calibration runs and runs with not operating strings reduce the life time. The Starting-Downgoing-Filter has filtered events with a rate of approximately 2 Hz and has produced a data set with a total live time of 8813 hours.

Figure 27 shows the event rate of the accepted data-runs. The run number increases with time. A standard run of the IceCube detector has a duration of eight hours. Runs are shorter if they are recognized as faulty or if special runs are scheduled in between. The observed event rate varies over time between 1.7 Hz and 2.1 Hz. This variation corresponds to the seasonal variations observed in the atmospheric muon flux [Til09]. Additionally, gaps between the runs are visible. Two of them are particularly large: at run numbers of about 112750 and 113750. The first corresponds to the first test runs for the IceCube configuration with 59 strings in February 2009. The second gap is due to a large set of final test runs in May 2009. In between, several smaller tests were executed causing smaller gaps. Further tests of the filter performance are shown in [Kno09].

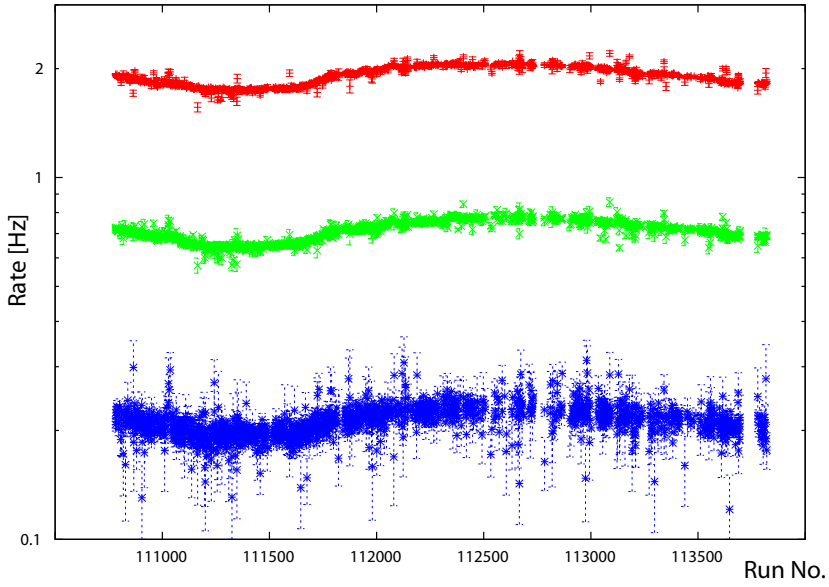

Figure 27: Recorded Event Rate by the on-line filter (top) and on higher filter levels: the low energy data set in the middle (section 6.3.2) and the high energy data set at the bottom (section 6.3.4). For a better visibility the rate of the high energy data set is magnified by a factor of ten. The error bars indicate statistical errors.

6.3 Reconstruction and Data Filtering

All data arriving from the pole are stored in a computer center at the University of Wisconsin - Madison. The next processing step is applied to events passing various filters. It does not apply any selections. For each event additional reconstruction algorithms are applied and observables which describe the event properties are determined. The output of the Starting-Downgoing-Filter is part of this processing (section 6.3.1). After these general reconstructions the data is further processed with more specialized algorithms and filtering steps (section 6.3.2 and section 6.3.4) for tracks with an interaction vertex inside of the detector are performed. Figure 28 gives an overview of the dependencies of different reconstructions and characteristic parameters.

6.3.1 Muon Track Reconstruction

In the North the data is reprocessed. Here, the reconstructions performed at the pole are not used. In the new processing updates of the calibration and the status information are considered. The results of the new reconstructions are therefore more accurate than these obtained at the pole. The reconstruction of the muon tracks is done in several steps. It starts with the recorded waveforms of the DOMs. The following algorithms are applied to each event selected by the Starting-Downgoing-Filter:

- The FeatureExtractor extracts the arrival times and amplitudes of the pulses from the waveforms recorded by the DOMs,
- the duration of the event is reduced to the central 6 μs,

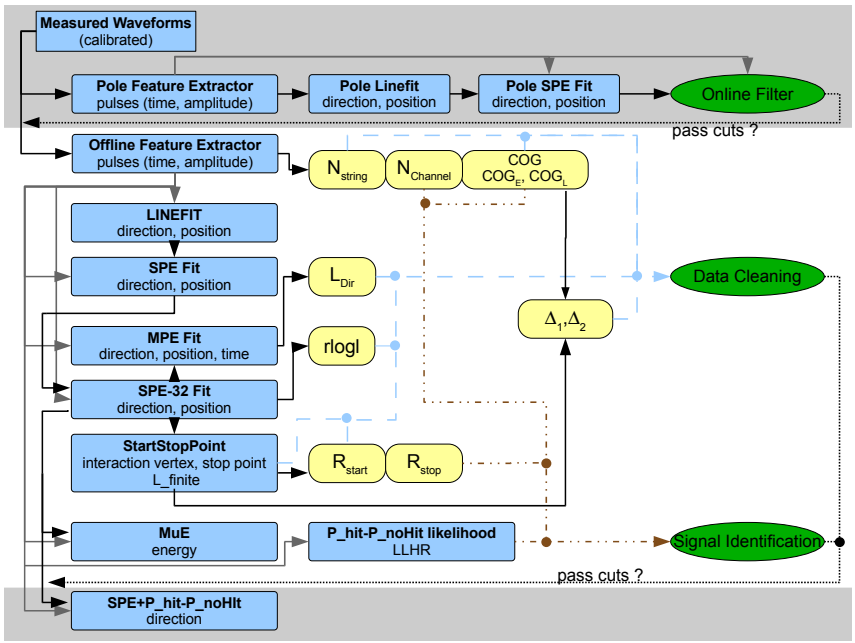

Figure 28: Dependencies of the reconstructions, observables and selections. Yellow (rectangular with round corners) are observables, green (elliptical) selections and blue (rectangular) reconstruction algorithms together with the determined parameters. The gray shaded areas separate different selection steps. The different line styles and colors are used to improve the readability.

- the LINEFIT reconstruction is applied to the remaining hits (section 5.1),
- a SPE likelihood reconstruction (section 5.2.1) seeded with the LINEFIT result is applied,
- a SPE likelihood is executed 32 times with random seeds, called 'SPE-32 Fit',
- the StartStopPoint reconstruction is applied to obtain the interaction vertex and the stop point (section 5.1.2) based on the reconstruction with the SPE-32 Fit.

These reconstructions focus on the direction and the position of the track in the detector. These are the quantities required for all analyses. A good performance is achieved by using a likelihood fit (SPE) seeded with an initial reconstruction (LINEFIT). To ensure that the minimum found by the SPE fit is the global minimum in the allowed parameter space the likelihood reconstruction is repeated with 32 random seeds. This probes different regions in the parameter space to eventually find better solutions. In the following analysis the direction and position determined by the SPE-32 Fit is used. A comparison to other reconstructions can be found in appendix B.
The last step reconstructs the position of the interaction vertex and the stop point. This is not part of the central IceCube processing. The algorithm relies on the angular reconstruction of a previous algorithm. The SPE-32 Fit provides the most accurate reconstruction of the direction and the position and thus ensures the best possible results for the interaction vertex and the stop point estimate.

Table 5: Cleaning selections used on the data to remove events with a bad angular reconstruction and events which are unlikely to originate from a neutrino interacting in the detector.

rlogl	< 12	N_{string}	> 2
COG_Z	$> -400\,\text{m}$	R_{start}	> 0.1
L_{Dir}	$> 100\,\text{m}$	Δ_1	$< 60°$
L_{finite}	$> 200\,\text{m}$	Δ_2	$< 20°$

Further algorithms are only applied to events of a good reconstruction quality. This reduces the required amount of computation time. A reconstruction is considered good if the reduced likelihood value (rlogl) of the SPE-32 Fit is smaller than 12 (section 6.3.2). In this case the following additional algorithms are applied:

- a MPE likelihood reconstruction (section 5.2.2),

- the MuE energy reconstruction (section 5.4).

These two algorithms provide the estimates for the event time and the muon energy. The time information is important to determine the Direct Hits (section 6.3.2). This analysis does not use the energy information of the events. However, the MuE reconstruction is included to test its applicability. This is discussed in details in section 6.3.4.
In addition, also the here developed P_{Hit}-P_{noHit} likelihood in combination with the SPE likelihood (section 5.3) is used for the reconstruction. This is done only with a subset of the data to check the performance. The results are documented in appendix B.

6.3.2 Cleaning Selections to Remove Badly Reconstructed Events

The goal of cleaning selections is to remove events with bad reconstructions and events which are unlikely to be generated by a signal neutrino. Signal events with a large difference between the reconstructed direction and the source direction are identified and removed. The remaining signal is expected from a relatively small region. Additionally, events unlikely to be neutrino signal events are removed. For events with a reconstructed interaction vertex close to the border of the detector the hypotheses of a track with the interaction vertex inside or outside the detector cannot be distinguished and they are discarded, too.
In an optimization process which considers various available quality parameters, eight of these parameters are selected. Figure 30 shows the distributions of these parameters and figure 31 shows the dependency between some of these parameters and the error of the reconstruction for simulated signal events. The selection parameters and values are listed in table 5. Each of these selections is loose: the aim is to improve the angular resolution and not to separate between signal and background events. Therefore, the selections discard only small amounts of events. Below, each of the selections is discussed individually. For the evaluation the signal simulation and the measured data from the off-source region (section 4.2) are used.

Reduced Likelihood Value (rlogl)

The reduced log-likelihood value at the global maximum

$$rlogl = \frac{1}{N_{\text{d.o.f.}}} \min_{\vec{a}} \left[-\log(L(\vec{a})) \right] \ . \tag{49}$$

is delivered by the likelihood reconstruction. In this equation the log-likelihood is scaled by the number of degrees of freedom $N_{\text{d.o.f.}}$. This is the number of measured input parameters minus the number of reconstructed parameters. This factor scales the log-likelihood of events with a similar reconstruction quality to the same number. Note, that this definition is statistically problematic, since the absolute value of $\log(L)$ is undetermined by an additive constant, which could differ between events. The division by $N_{\text{d.o.f.}}$ is therefore only justified empirically.
rlogl of the SPE-32 Fit quantifies the quality of the fitted parameters. Well reconstructed tracks have a small value of rlogl. This selection removes events for which the assumption of a single muon track in the likelihood reconstruction is not appropriate. The different signal distributions in figure 30 peak at small values of rlogl and decrease towards poorer reconstructions. The position of the peak shifts to higher values for signals with more low energetic events.
The off-source data distribution is broad due to the inclusion of events which do not fit the hypothesis of a muon track. These events are responsible for the relatively large amount of events with high values of rlogl (compared to the signal distributions). All simulated events contain a muon track. Here, events with large values of rlogl are caused by the input into the reconstruction: there are either few or mostly scattered hits. In this case the reconstructed direction has large uncertainties. Above a value of about rlogl= 11 the fraction of off-source events is larger than the contribution of all shown signal hypotheses. The selection on rlogl is placed carefully. The fact that the peak shifts to higher values with a larger amount of low energetic events indicates that these tend to have larger rlogl values. A hard selection would remove too many of the low energetic events. Therefore, a moderate value of rlogl= 12 is chosen for the selection. More background than signal is removed from the data set by this cut.

Number of Hit Strings (N_{string})

The selection on the number N_{string} of strings with at least one hit DOM is placed to achieve a more reliable reconstruction. N_{string} describes the horizontal size of the recorded event. Due to the sparse instrumentation in this direction the number of strings is important for the reconstruction of the azimuth angle. If only two strings have DOMs with a hit, the reconstruction is likely degenerated and the likelihood reconstruction may yield more than one optimum. Therefore, events with $N_{\text{string}} > 2$ are selected. The distribution of N_{string} (figure 30) shows that the number of removed events is small for off-source data and signal simulations. Due to the similar distributions further selections on N_{string} are not useful.

The Direct Length (L_{Dir})

For each event the Direct Hits are determined. A hit recorded in a DOM is called direct if the time residual Δt_{res} (section 5.2.1) is between -15 ns and 75 ns. For a given muon

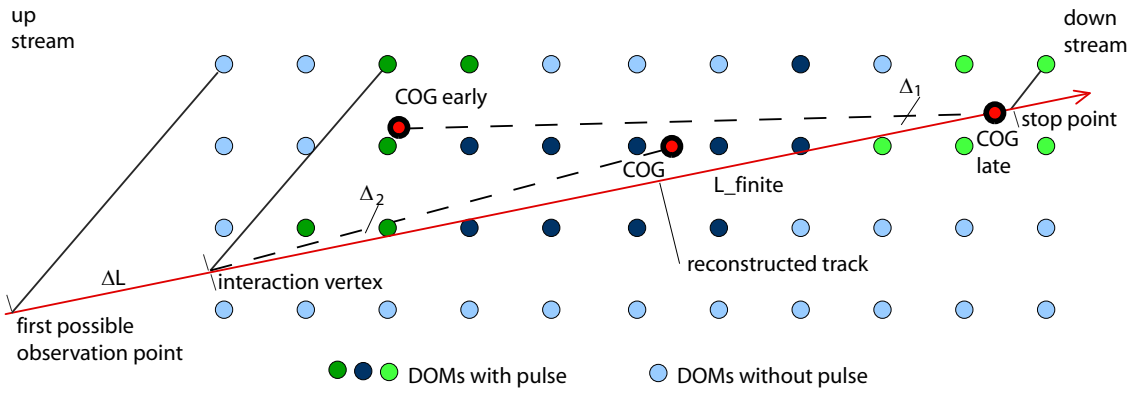

Figure 29: Schematic view of a track passing through the detector. The markers represent DOMs: dark green are early hits, dark blue intermediate hits and light green late hits. The larger red dots mark the center of gravity of the hits and different sub-sets of hits. Also, the reconstructed interaction vertex and stop point are shown. They are determined by the assumption of Cherenkov light arriving at the DOMs. In this example is $R_{\text{stop}} = 0$ and $R_{\text{start}} = \Delta L/(L_{\text{finite}} + \Delta L)$.

direction and position the Direct Hits depend on the reconstructed event time. Therefore, the time reconstructed with the MPE Fit (section 5.2.2) is used. Direct Hits are most likely caused by unscattered Cherenkov photons and provide the best information for the reconstruction.
For each DOM with a Direct Hit the closest approach position of the reconstructed track is determined. The largest distance between two of these positions is called 'Direct Length' L_{Dir}. It describes the size of the region, for which Direct Hits yield good information. Figure 30 shows the distributions of signal and off-source events. They have several peaks caused by the string spacing in the detector. The selection at a length of 100 m is placed at the first minimum and requires Direct Hits on at least two strings. Muons with at least 20 GeV can cover this distance in the detector. This is a minimum requirement for any track-like event. Events fail this selection if they are not track-like and do not have Direct Hits or if they are reconstructed in a completely wrong direction. Events with $L_{\text{Dir}} < 100$ m have a more or less random direction compared to the truth known from simulations (figure 31). Signal events not passing this selection are thus badly reconstructed since the identification of Direct Hits fails. For the background, events a larger fraction is rejected by this selection. Here, the assumption of a muon track does not fit.

Comparisons to the Recorded Hits (Δ_1, Δ_2)

The SPE-32 Fit uses the timing information of the extracted hits. The reconstructed direction is compared with the spacial hit distribution to test its accuracy. The following geometric observables are characteristic for the distribution of the hits (they are sketched in figure 29):

- the position of a potential interaction vertex ($\mathbf{X}_{\text{start}}$),
- the position of the center of gravity of the earliest 25% of the hits ($\mathbf{COG}_{\text{early}}$),

- the position of the center of gravity (**COG**) of all hits,
- the position of the center of gravity of the latest 25% of the hits ($\mathbf{COG}_{\text{late}}$),
- the position of a potential stop point ($\mathbf{X}_{\text{stop}}$).

The first two positions are close to the beginning of the hit distribution while the last two are close to the end; the third one is in the center. In the ideal case all connections between two of these positions have the same direction as the reconstructed muon track. Figure 30 shows the distributions of the angular difference (**d** is the reconstructed direction)

$$\Delta_1 = \arccos\left(\frac{\mathbf{d}\cdot(\mathbf{COG}_{\text{early}} - \mathbf{COG}_{\text{late}})}{|\mathbf{d}|\cdot|\mathbf{COG}_{\text{early}} - \mathbf{COG}_{\text{late}}|}\right) \tag{50}$$

for different signals. They are more strongly peaked at small angles than the distribution for the off-source data. The off-source events have a long tail towards large angular differences. This tail contains dominantly events with a bad angular reconstruction (figure 31). It is removed by a cut at 60°. The loss of signal is small.
A second angular difference used is

$$\Delta_2 = \arccos\left(\frac{\mathbf{d}\cdot(\mathbf{X}_{\text{start}} - \mathbf{COG})}{|\mathbf{d}|\cdot|\mathbf{X}_{\text{start}} - \mathbf{COG}|}\right) . \tag{51}$$

The distributions for the various signal hypotheses and the off-source data are rather similar to those for Δ_1. However, two differences are observed: the distributions are narrower and the off-source events peak at 90°. These reconstructed events are perpendicular to the direction expected from the hit distribution. This peak is explained by events without a track-like component. Due to the narrower distributions all events with $\Delta_2 > 20°$ are removed. At this value hardly any ($< 1\%$ for all energy spectra) signal events are rejected.

Reconstructed Length (L_{finite})

$L_{\text{finite}} = |\mathbf{X}_{\text{start}} - \mathbf{X}_{\text{stop}}|$ is the distance between the reconstructed interaction vertex and the reconstructed stop point (section 5.1.2, figure 29). Similar to the Direct Length the distributions of L_{finite} (figure 30) have peaks corresponding to the distance between the strings. This selection improves the angular reconstruction quality by testing the hit distribution in the detector. If the hits are all located in a small area the angular reconstruction is on average rather bad. Rejecting events with $L_{\text{finite}} < 200\,\text{m}$ removes badly reconstructed events and is still below the main contribution of the signal events (figure 31). Approximately 200 m correspond to the distance between two strings taking into account the zenith direction of the Galactic Center. This requirement is similar to the selection on the number of strings and the Direct Length. Events which do not pass this selection are too small for a reliable reconstruction or the reconstructed direction is not aligned with the hits.

Depth of the Center of Gravity ($\mathbf{COG}_Z$)

The depth of the center of gravity COG_Z of the hits of an event has to be more than 100 m above the bottom of the detector (-400 m in the coordinate system with the origin

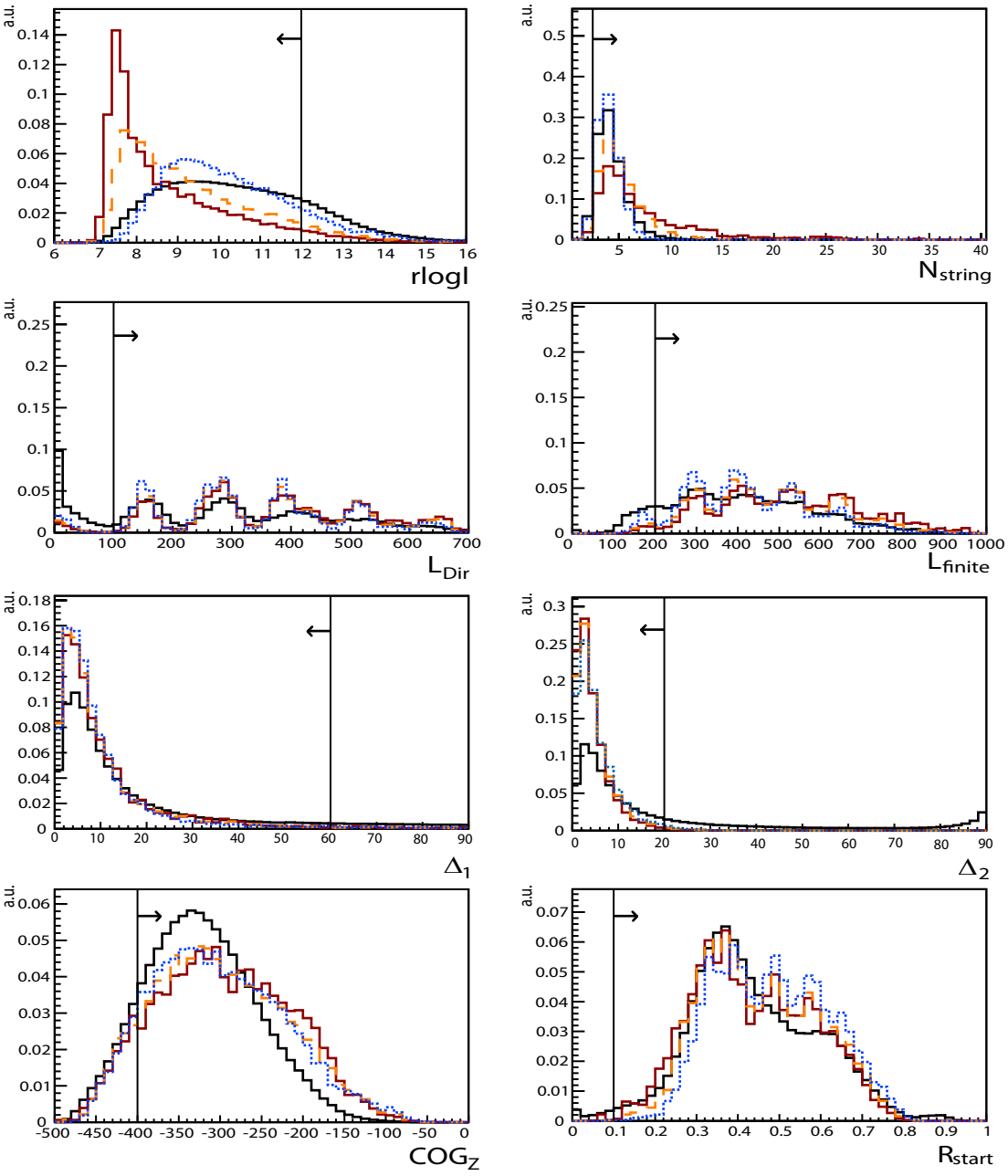

Figure 30: Distributions of the cleaning parameters. From top left to bottom right: rlogl, N_{string}, L_{Dir}, Δ_2, Δ_1, L_{finite}, COG_Z and R_{start}. The black distribution is for background determined from the off-source region and the thin vertical line is the selection value. The arrows indicate the region which is kept. The colored lines represent different signals. For point source like signals two energy spectra with $\gamma = 2$, $E_{\text{cut}} = \infty$ (full dark red line) and $\gamma = 2$, $E_{\text{cut}} = 10\,\text{TeV}$ (dashed orange line) are shown. For the neutrinos from annihilating Dark Matter particles a mass of 1 TeV (dotted blue line) is shown for the W^+W^- decay channel. All distributions are normalized to 1.

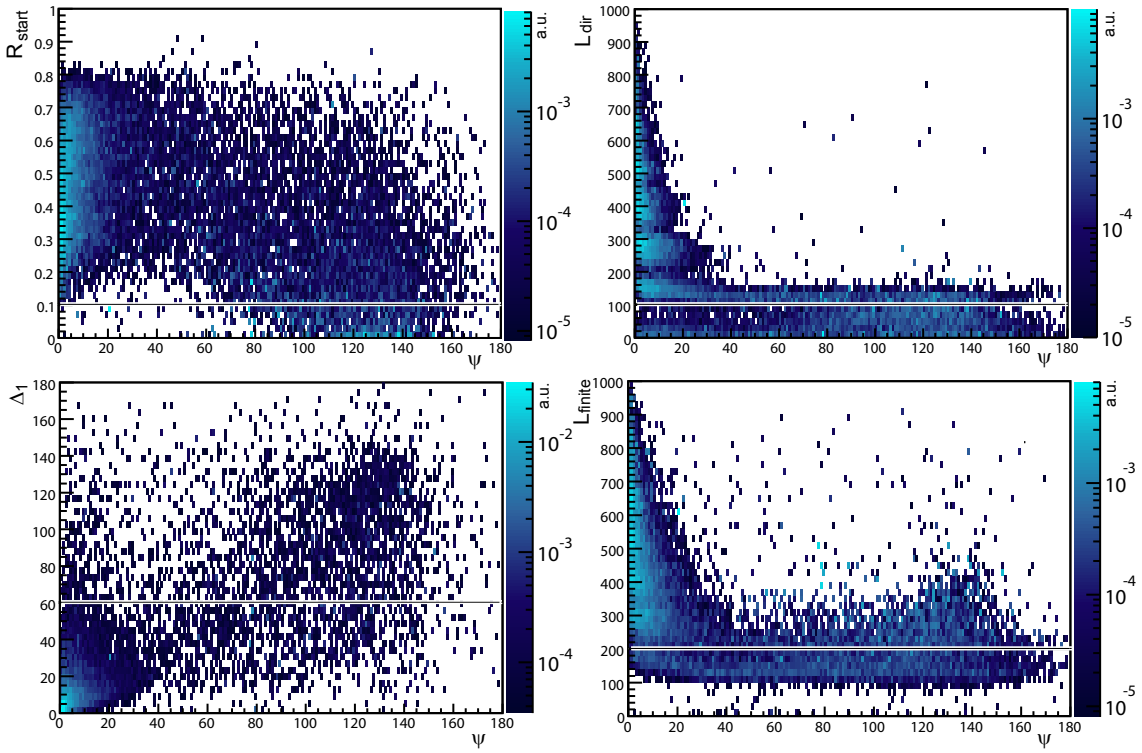

Figure 31: Distributions of the cleaning parameters in dependence of the reconstruction error ψ (difference between simulated and reconstructed direction). From top left to bottom right: R_{start}, L_{Dir}, Δ_1 and L_{finite}. The black line indicates the selection value.

in the center of the detector). The distributions (figure 30) for the events from the signal simulation and the off-source region are similar in this range. Events with recorded hits only below this limit are short and a good reconstruction is unlikely. The choice of 100 m is a similar requirement to these applied by the N_{string}, L_{Dir} or L_{finite} selection. Larger selection values would remove more signal events than intended.

Selecting Starting Events (R_{start})

Finally, a selection on R_{start} selects events which might have interacted in the detector volume.

$$R_{\text{start}} = \frac{|\mathbf{POS}_{\text{start}} - \mathbf{X}_{\text{start}}|}{|\mathbf{POS}_{\text{start}} - \mathbf{POS}_{\text{stop}}|} \,. \tag{52}$$

Here, $\mathbf{POS}_{\text{start}}$ is the first and $\mathbf{POS}_{\text{stop}}$ the last possible observation point given by the reconstructed geometry of the track (figure 29). This parameter measures how long the particle travels through the detector unnoticed.
For the later identification (section 6.3.4) of neutrino induced events it is necessary that the track passes through part of the detector without a hit. The selection requires $R_{\text{start}} > 0.1$. This selection is similar to the requirement that the most up-stream string has no hit. Events which do not fulfill this requirement are indistinguishable from muons entering the detector from outside. This selection removes hardly any signal events ($< 1\%$). The

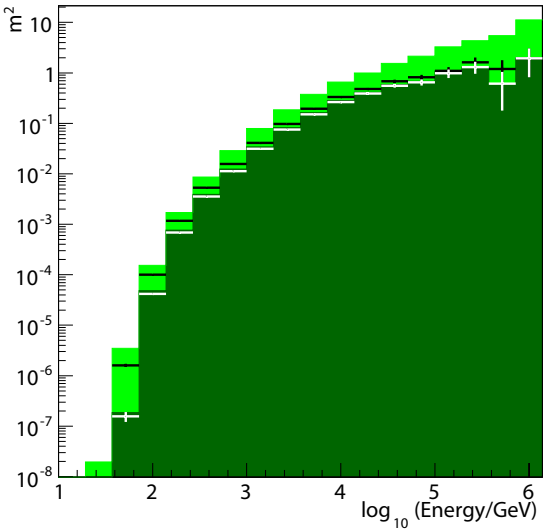

Figure 32: Effective neutrino area in the direction of the Galactic Center before (light green) and after (dark green) the cleaning selections. Additionally, the effective areas before (black) and after the selections (white) are shown for events with an angular reconstruction error less than 10°. Error bars indicate statistical uncertainties.

dominant fraction of events has values larger than 30%. This large value is caused by the previously applied online filtering (section 6.2) and the vetos therein. Additionally, figure 31 shows that events with $R_{\text{start}} < 0.1$ are on average reconstructed with a large angular error.

About 36% of the background events (off-source data) pass these selections. The main difference between the different signal hypotheses is the expected energy distribution of the neutrinos. Figure 32 shows the effective detector area in dependence of the energy, to investigate the impact of the selections on the signals. The effective area quantifies the apparent size of the detector for events of a certain energy and it is proportional to the expected amount of signal events. The values are determined from the signal simulation. The effective area before applying the selections increases rapidly above 100 GeV. The increase slows down at higher energies. About $10\,\text{m}^2$ effective area is achieved at 1 PeV.

The selections reduce the effective area by approximately a factor of two in the central energy range. The loss for energies below 100 GeV and close to 1 PeV is larger. The larger loss at low energies is caused by events which are not properly reconstructed due to the small amount of light in the detector. The removed high energetic events are dominantly rejected because of the requirement to have no hit on the first 10% of the path through the detector. These neutrinos interact outside of the detector volume.

In addition figure 32 shows the effective area for events with a reconstruction accuracy better than 10°. Before the selections are applied a large difference between this effective area and the effective area for all data is observed. After the selections both are similar. Comparing the effective areas before and after the selections for the events with a good reconstruction shows that in the central energy range only about 10% of the area is lost.

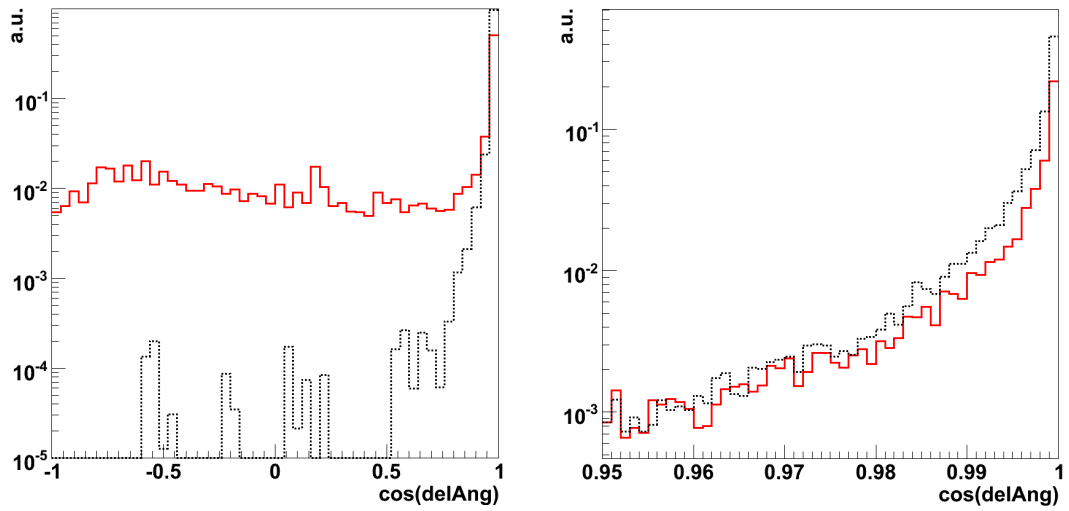

Figure 33: Angular distance between the neutrino direction generated in the simulation and the reconstructed direction by the SPE-32 Fit before (red solid line) and after (black dotted line) the cleaning selections. An energy spectrum with a power law index of $\gamma = 2$ and a energy cut-off at $E_{\text{cut}} = 100\,\text{GeV}$ is used (equation 12). The other investigated energy spectra are similar. The left panel shows the whole parameter range, the right has a finer binning and shows only events with smaller reconstruction errors. Both distributions are normalized to one.

Below 200 GeV the selections remove also well reconstructed events, resulting in larger losses.

Figure 33 shows the distribution of the angular difference between the initial neutrino direction in the simulation and the result of the SPE-32 Fit before and after the cleaning for one example energy spectrum. Both distributions peak at small angular differences. Without the selections a long tail of poorly reconstructed directions is observed. This tail contains more than 40% of the events. Applying the cleaning selections removes the tail almost completely. Mostly well reconstructed events remain in the dataset.

The angular resolution, given by the median of the distribution of the angular differences, is about 16° before and 2.6° after the cleaning. Thus, the presented selections work well to clean the data set from badly reconstructed events.

6.3.3 The Lowest Energy Events

This analysis is focused on low energetic events. For the Dark Matter signal the neutrino energies are expected to be below some TeV. For the point-like source signal hypothesis the lowest investigated cut-off energy E_{cut} is at 100 GeV (section 4.1.2). Events with these energies are among the lowest energetic in the remaining data sample (figure 32).

The only way to separate neutrino induced events from muons generated by air showers is to ensure that the interaction vertex lies within the detector. In this case the trace of the light begins in the middle of the detector volume. Unfortunately, this signature can be created by atmospheric muons, too.

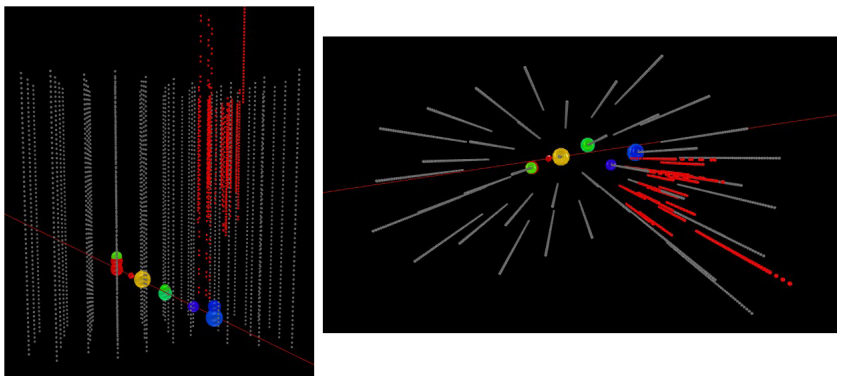

Figure 34: An example event from the simulation of muons produced in air showers. It mimics a neutrino event with the interaction vertex in the center of the detector. The small dots symbolize the DOMs of the IceCube detector. The colored spheres mark DOMs with a recorded hit. The color corresponds to the time (red to blue) and the size to the amount of deposited charge. The line indicates the track of the muon. Left: side view; Right: top view.

Atmospheric muons have a steeply falling energy spectrum. Thus, they are in general not highly energetic. A realistic assumption is a minimally ionizing muon. It causes the least possible light deposit per distance. The amount of light detected at a certain position depends only on the ice properties and the distance to the particle. A muon entering the detector in the middle between two strings or in a region of large absorption in the ice might pass a part of the detector unobserved. Later along the track, the ice properties might have changed or it passes close to a string and hits are observed. This perfectly mimics a neutrino interacting close to the first observed hit. The hits further down-stream might be caused by the secondary muon.

The amount of muons with this kind of signature is enhanced by the combination of two facts: the hits removed due to the HLC cleaning and the large absorption in the Dust Layer have a large impact for events from the direction of the Galactic Center.

The HLC cleaning removes DOMs with isolated hits (section 3.2.5) from the data to reduce the amount of noise. This procedure also removes hits caused by muons if they are isolated. If the probability of a hit in a certain detector region is small due to the ice properties or the relative position to the muon track, there might be only isolated hits. For average ice properties and minimum ionizing particles the probability to measure a single hit in 50 m distance (perpendicular) to the muon track is about 20% (extracted from simulated data, figure 22). Thus, this procedure removes many hits generated by muons passing through the middle between two strings.

In the regions of the detector with increased absorption in the ice this effect is further enhanced. Such a region is the Dust Layer (section 3.2.3). With its position at a depth of 1980 m to 2080 m the Dust Layer is just below the veto at the top of the detection region. A muon entering the detector from the side at the depth of the Dust Layer propagates through it almost unseen. When the event leaves the Dust Layer it may mimic a neutrino interacting at this point.

In combination these two effects significantly enhance the number of muons from air showers sneaking into the inner parts of the detector and mimicking an interacting neutrino.

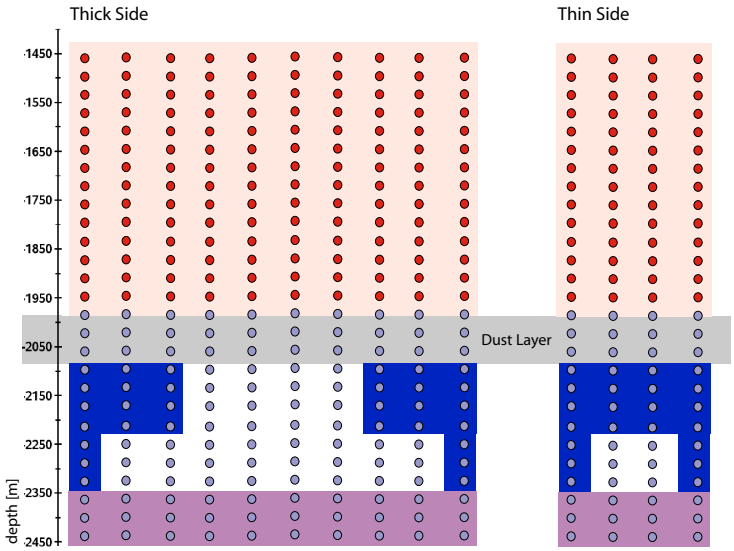

Figure 35: Schematic side view of the IC40 detector including the Dust Layer. Regions affected by bad veto conditions and bad reconstruction conditions are marked: The top part is included in the veto and the bottom part is removed by the COG_Z selection. The regions at the sides are affected by the first hit selection of the on-line filter. This region is increased due to the impact of the Dust Layer.

Due to the position of the Dust Layer the amount of these events depends on the observed zenith direction. Roughly horizontally and vertically muon events are not affected: Horizontal events pass through the detector below the Dust Layer or get completely lost in it while the vertical events are already rejected by the DOMs above the Dust Layer. For events from the direction of the Galactic Center the effect is maximal. The events travel twice the vertical distance in horizontal direction. Considering the thickness of the Dust Layer the tracks can pass up to three layers of strings (approximately 300 m) before leaving the Dust Layer at its lower border. This is about a third of the length a muon can travel inside the detector (figure 35). Muons with this signature are indistinguishable from neutrinos interacting below the dust layer.
Figure 34 shows an example event from the simulation of muons from air showers. It perfectly mimics a neutrino with the interaction vertex in the center of the detector. The only possibility to remove events like this would be to remove all events entering the detector through the Dust Layer or in between strings.
As a possible solution to remove events entering through the Dust Layer, events with the first hits in the upper parts of the detector just below the Dust Layer have to be excluded (figure 35). Considering the thickness of the Dust Layer and the direction of the signal events these have to be more than 200 m away from the border of the detector (or about three rows of strings).
Below the removed region the remaining volume is small considering that 8 hits are needed to fulfill the trigger conditions or even more to achieve a good reconstruction. Due to the larger absorption events causing hits in the Dust Layer have on average higher energies. This is discussed in section 6.3.4 for high energetic events. Additionally, a larger amount

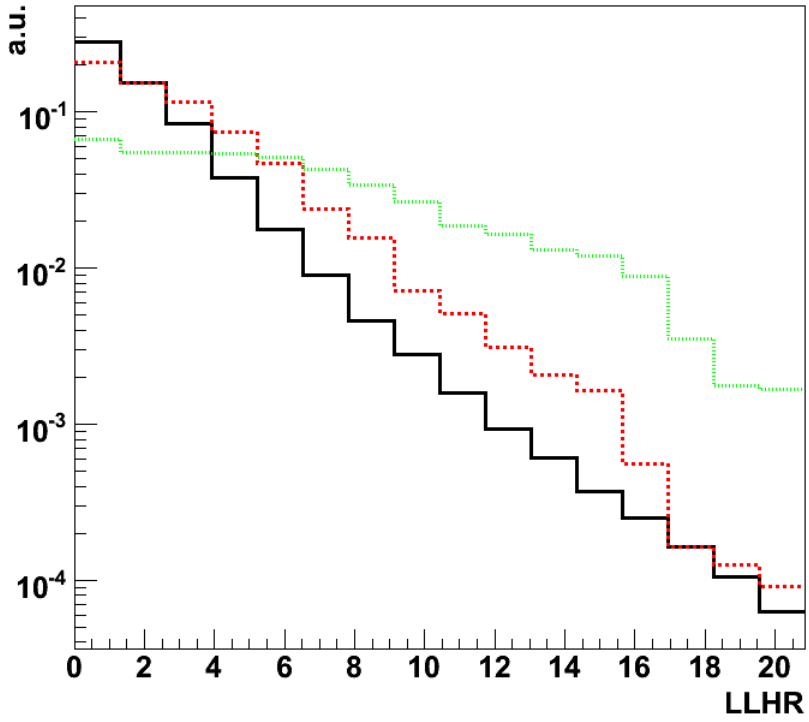

Figure 36: Distribution of the LLHR parameter quantifying the probability to detect a muon earlier then the first recorded hit. Solid black line: off-source data; Dashed red line: signal simulation ($\gamma = 2$, $E_{\text{cut}} = 1\,\text{TeV}$). Additionally $Sig/\sqrt{BG}$ (Sig: amount of signal events, BG: amount of background events) for a selection on small LLHR values is shown (green dotted).

of background events is measured in the Dust Layer due to the thinner ice shield above. Applying such constraints on the volume removes a huge fraction of signal events. This loss can not be recovered by the amount of removed background events. Thus, it is not possible to remove the background events by excluding all events passing through the Dust Layer.
The second possible solution is to remove the events sneaking in between strings. The LLHR parameter quantifies the probability for an event to be detected before the first hit is recorded taking into account the ice properties (section 6.3.4). Its distribution for one signal assumption and background is shown in figure 36 together with the change in sensitivity for selections on this parameter. The sensitivity S depends on

$$S \propto Sig/\sqrt{BG} \tag{53}$$

Sig is the amount of signal events and BG is the amount of background events. All selection values lower the sensitivity and thus, this method is not applicable.
As shown, both methods fail to improve the sensitivity of IC40. It is possible to increase the purity of signal events in the data set but not to gain sensitivity. In addition each applied selection would contribute to the systematic uncertainties of the signal prediction. This

Table 6: Selections used to identify high energetic starting events.

N_{chan}	> 40	R_{stop}	< 0.19
LLHR	> 2.5	COG_Z	$> -270\,\text{m}$

prediction is based on the simulated events and an imprecise prediction of the distribution of a selection parameter affects the passing rate. Thus, no further selections are applied to the data.

6.3.4 Signal Selections for High Energy Events

This analysis tests for a point-like source with a hard power law energy spectrum with events up to 1 PeV. The higher energetic neutrinos expected from these hypotheses are separated from background events by selections on energy dependent parameters. The aim of this filtering stage is to optimize the sensitivity for neutrino events between 10 TeV and 1 PeV while accepting the loss of events of lower energy. In section 6.4 the signal hypothesis, for which this data set is most sensitive, is determined.

Among all possible selection parameters four are chosen. These selection parameters and their values are listed in table 6. The selections on these variables are optimized by a scan of the complete parameter space. The distributions of signal and background events are shown in figure 37 and discussed individually below. Due to the focus on high energies, energy spectra with $\gamma = 2$ and $E_{\text{cut}} > 10\,\text{TeV}$ serve as test signals. The distribution of background events is determined from the off-source data as well as from the simulated background events. This approach allows a cross check of the simulation procedure.

Likelihood for a Starting Track (LLHR)

The likelihood ratio LLHR quantifies the probability of the observation of the track (parameters $\vec{a}$, SPE-32 Fit, section 5.2.1) before the reconstructed interaction vertex (StartStopPoint, section 5.1.2) is.

$$LLHR = \log\left(L_{P_{\text{hit}}-P_{\text{noHit}}}(\vec{a}|\text{start})\right) - \log\left(L_{P_{\text{hit}}-P_{\text{noHit}}}(\vec{a}|\text{inf})\right)\ . \tag{54}$$

Here, the P_{hit}-P_{noHit} likelihood (section 5.3) is used: assuming a track which starts inside the detector or is infinite. For events with $LLHR \approx 0$ an infinite track has the same probability as a track starting in the detector.

Figure 37 shows the distributions of LLHR for different signal hypotheses and background: All peak at zero and decrease rapidly for large values of LLHR. At LLHR = 0 about a factor of two more background is expected than signal. At larger values of LLHR signal events are more likely. The difference between the signal and the background distribution is relatively small. Due to the geometry of IC40 most of the signal events start close to the outer string layer and, thus, have LLHR values close to zero. The selection is placed at a relatively small value of LLHR > 2.5.

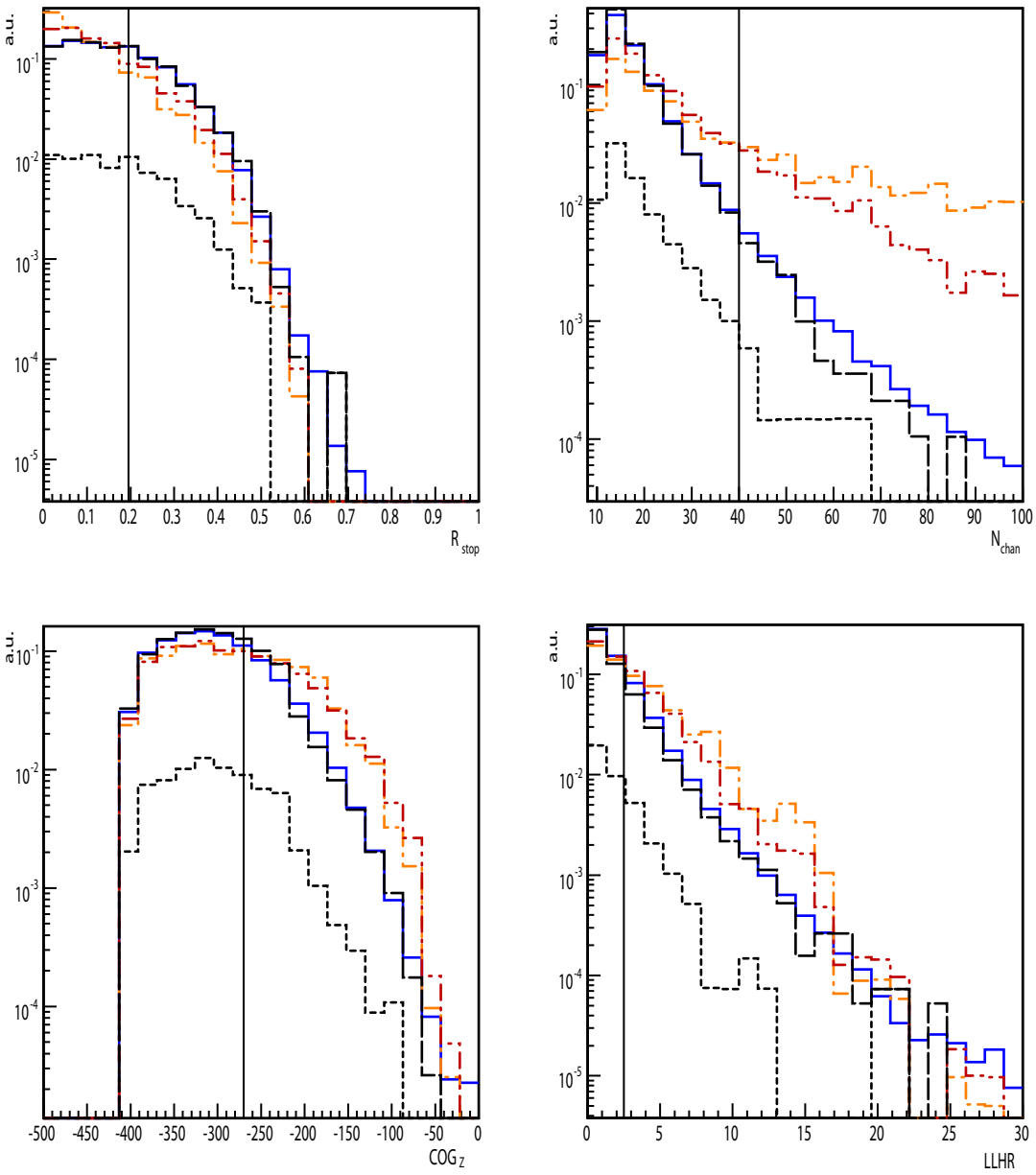

Figure 37: Distributions of the parameters used for the signal identification selections. Top left: R_{stop}; top right: N_{chan}, bottom left: COG_Z; bottom right: LLHR. The blue line shows events from the off-source region and black shows simulated background events: coincident air showers (small dashes) and the sum of single and coincident air showers (large dashes). The red lines are neutrino signals with an E^{-2} energy spectrum: no cut-off (light red, dot dashed) and a cut-off at 10 TeV (dark red dot-dot-dashed).

Selecting not Stopping Events ($R_{\mathbf{stop}}$)

R_{stop} is defined similar to R_{start} in equation 52. X_{start} is replaced by X_{stop} the position of the potential stop point (figure 29). This parameter measures how long the particle travels through the detector unnoticed before leaving the detector. A selection on R_{stop} is based on the expected track length of the muon generated by signal neutrinos: For muon energies above several 100 GeV the average track length is more than 1 km. A high energy muon produced in a neutrino interaction in the detector has a high probability to leave the detector and $R_{\text{stop}} \approx 0$ is expected.
Figure 37 shows the distributions of R_{stop} for different signal hypotheses and background. As expected, the signal distributions have a clear maximum at $R_{\text{stop}} = 0$. The background distributions are flat between up to $R_{\text{stop}} \approx 0.2$ and decrease afterwards. Above $R_{\text{stop}} \approx 0.6$ no events are observed. For events with larger values of R_{stop} the remaining detector volume is to small to trigger. The difference at small R_{stop} is used by selecting only events with $R_{\text{stop}} < 0.19$.

Depth of the Center of Gravity ($\mathbf{COG}_Z$)

COG_Z is forced to be within the 270 m below the top veto of the on-line filter. All events with a zenith direction close to the zenith angle of the Galactic Center and a $\text{COG}_Z > -270$ m have passed the top veto. Figure 37 shows the distributions of COG_Z for different signal hypotheses and background. In both cases the amount of events increases with depth and breaks off at -400 m due to the cleaning selection.
In the top part a relatively large amount of signal events is expected compared to the background expectation. The top veto is highly efficient in rejecting background events even when considering the higher rate due to the thinner ice shield. Below background events enter the detector from the side passing the less efficient side veto and result in a larger amount of background. Signal events may interact below the top veto and can cause the events with $\text{COG}_Z > -270$ m.

Amount of Light in the Detector ($N_{\mathbf{chan}}$)

N_{chan} is a measure of space points which enter the reconstruction. For more points more precise results are expected. Additionally, N_{chan} is correlated with the muon energy, as discussed in section 5.4. Therefore, the use of N_{chan} as selection parameter discards low energetic events.
Figure 37 shows the distributions of N_{chan}. They have a peak at small values just above the trigger threshold and decrease towards higher values. The distributions of background events decrease faster than for expected signals. Only events with $N_{\text{chan}} \geq 40$ pass the selection.
Figure 38 compares the selection on N_{chan} with a selection on the reconstructed energy (MuE) by showing the resulting signal and background passing rates. Independent of the selection value and the signal hypothesis, N_{chan} separates signal and background events better (or equally well) than the energy reconstructed by the MuE algorithm. Presumably, this effect is related to the fact that N_{chan} not only selects high energy events but also geometrically better reconstructed events.

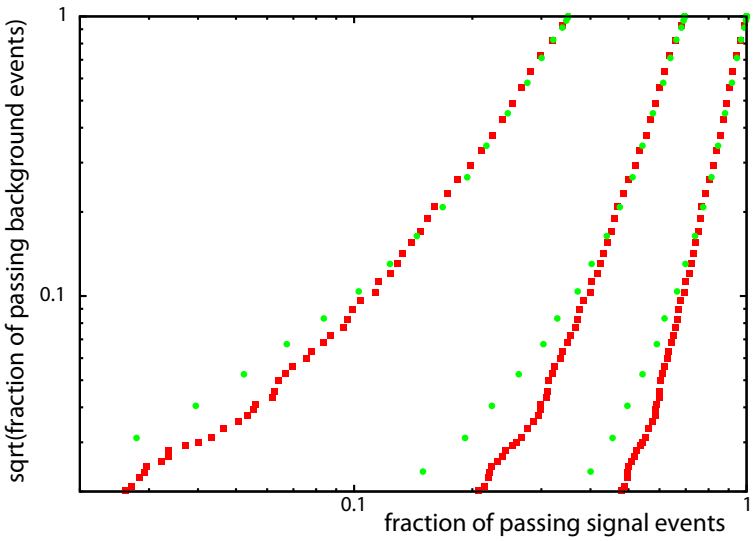

Figure 38: Signal passing rate versus background passing rates for various selections on the energy reconstructed with MuE (green circles) and N_{chan} (red squares). The signal passing rates are calculated for neutrinos with an energy spectrum with $\gamma = 2$ and cut-off energies at 10 TeV, 100 TeV and no energy cut-off (left to right). The used events also fulfill the selections on LLHR, R_{stop} and COG_Z.

Figure 37 shows two different distributions for the background expectation. One is determined from the events in the off-source region and the other one is derived from simulated events. The distribution of simulated events is composed from single and coincident air showers (section 6.1.2). For all four selection parameters the distributions of simulated and off-source events are reasonably similar. The only difference is observed for values of N_{chan} larger than 50. Less events with these values are simulated than measured in the off source region.

The efficiency of the signal selections is evaluated for the simulated data and the off-source data. The amount of remaining background events differs by about 5%. The agreement tests the reliability of the simulation procedure for signal and background events. The observed deviation between the background simulation and the off-source data is used as systematic uncertainty of the signal simulation, because both use the same algorithms.

A fraction of $7.7 \cdot 10^{-4}$ of the background events surviving the cleaning selections (off-source region) also pass the signal selections. Figure 39 shows the effective area to illustrate the passing rates for the different signal hypotheses. The effective area decreases for lower energies and below 1 TeV no simulated event survives the selections. The fraction of surviving signal events is about 10% for an energy of 10 TeV and larger above. This is a small amount of signal events passing the selections. However, in comparison to the amount of passing background events it results in a significant improvement of the sensitivity.

Assuming a signal hypothesis with an energy spectrum with $\gamma = 2$ and no energy cut-off the central 90% of the surviving signal events have an energy in the range between 8 TeV and 800 TeV. For energy spectra with a cut-off this shifts slightly towards lower energies.

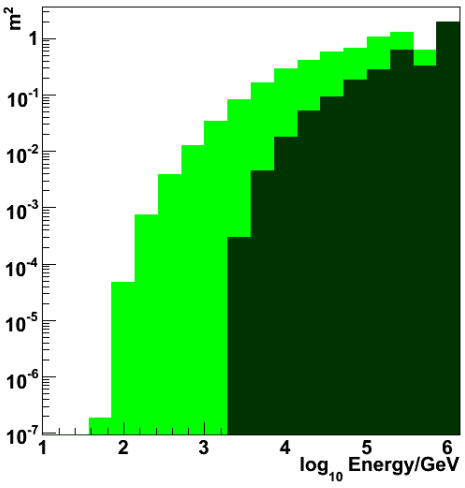

Figure 39: Effective neutrino area before (light green) and after (dark green) the signal identification selections in direction of the galactic center.

Table 7: Passing signal and background fractions after the combined filter steps (the values at trigger level are set to one). The fractions for the signal are averages due to the large variety of signal energy spectra.

	Sig ($E < 10\,\text{TeV}$)	Sig ($E > 10\,\text{TeV}$)	Off-Source	BG Sim
trigger	1	1	1	1
on-line filter	$\approx 1 \cdot 10^{-1}$	$\approx 1 \cdot 10^{-1}$	$2 \cdot 10^{-3}$	$2 \cdot 10^{-3}$
cleaning selections	$\approx 8 \cdot 10^{-2}$	$\approx 8 \cdot 10^{-2}$	$7 \cdot 10^{-4}$	$7.1 \cdot 10^{-4}$
signal selections	$< 10^{-7}$	$> 8 \cdot 10^{-3}$	$6 \cdot 10^{-7}$	$5.7 \cdot 10^{-7}$

The angular resolution remains about unchanged at the value achieved by the cleaning selection (section 6.3.2).

6.4 Summary of the Selected Data Sample

The passing fraction of signal events and background events are shown in table 7. The on-line filter and cleaning selections do not have a large energy dependence. These two steps reduce the amount of background events by more than three orders of magnitude. The high energy signal selection achieves a suppression of background events better than six orders of magnitude. In comparison to the IC40 search for point sources on the southern hemisphere [Dum09] the energy threshold is lowered by about two orders of magnitude from about 1 PeV to 10 TeV. Thus, sources with a energy cut-off in this range are accessible only with this analysis.
For the further analysis two data sets are used. One contains the events passing the high signal selection (high energy data) and is used for all hypotheses producing high energetic events. For all other hypotheses the data set after the cleaning selections without further selections is used (low energy data). The more sensitive data set is chosen for each signal hypothesis. This is investigated in the next chapter.

Table 8: Parameters of the energy spectra used in the optimization of the source region (equation 12). On the left side are spectra used for the high energy data set and on the right side these for the low energy data set.

	γ	E_{cut}		γ	E_{cut}
$\Phi_{2;\infty}$	2	∞	$\Phi_{2;0.1}$	2	100 GeV
$\Phi_{2;10}$	2	10 TeV	$\Phi_{2;1}$	2	1 TeV
$\Phi_{2;100}$	2	100 TeV	$\Phi_{2;10}$	2	10 TeV
$\Phi_{1.5;\infty}$	1.5	∞	$\Phi_{1.5;0.1}$	1.5	100 GeV
$\Phi_{2.5;\infty}$	2.5	∞	$\Phi_{2.5;\infty}$	2.5	∞

7 Sensitivity

The low and high energy data samples described in the previous section are used for the search for neutrinos from the direction of the Galactic Center. To achieve the optimum sensitivity the signal region as defined in section 4.2 is optimized in section 7.1. The optimization is done separately for the neutrinos from Dark Matter and for neutrinos from a point-like source. The number of expected background events from the off-source region is determined in section 7.2. Finally, the sensitivity for a neutrino signal from Dark Matter particle annihilations in the Galactic halo (section 7.4) and for a point-like source at the position of the Galactic Center is determined (section 7.3).

7.1 Optimization of the Signal Region

The size of this region is determined by the angular distance in declination $\Delta\delta$ (section 4.2) to the Galactic Center. The maximum angular difference in right ascension $\Delta\alpha$ depends on this size (equation 35). All events with a reconstructed angular distance to the Galactic Center smaller than $\Delta\delta$ in declination and $\Delta\alpha$ in right ascension are in the signal region. The optimization of $\Delta\delta$ has to be done separately for neutrinos from Dark Matter particle annihilations and neutrinos from a point-like source due to different source sizes and different energy spectra.
The optimization is done by maximizing $Sig/\sqrt{BG}$ in dependence of $\Delta\delta$. Here, Sig is the number of signal events and BG the number of expected background events in the signal region.

7.1.1 Optimization for a Signal from a Point-Like Source

The huge possible parameter space (section 4.1.2) complicates the choice of the optimum signal region size $\Delta\delta$ for a point-like source at the position of the Galactic Center. The power law index γ of the flux (equation 12) is varied between 1.5 and 2.5 and the energy cut-off between 100 GeV and 1 PeV. For some spectra the low energy data set and for others the high energy data set is more sensitive. The choice of the data set for each set of parameters is based on the final sensitivity at the optimum size of the signal region.
Only the low energy data set contains a reasonable amount of events below 10 TeV and the optimization is done only for steep energy spectra and cut-off energies below 10 TeV. For flat energy spectra and higher cut-off energies the high energy data set is expected

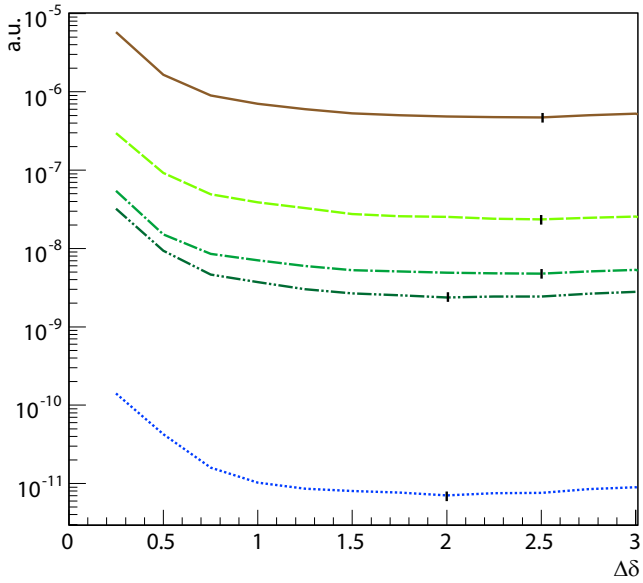

Figure 40: $Sig/\sqrt{BG}$ (in arbitrary units) for different signal region sizes $\Delta\delta$ for energy spectra with a cut-off energy greater than 10 TeV using the high energy data set. The parameters of the energy spectra are given in table 8. In green $\Phi_{2;\infty}$, $\Phi_{2;10}$ and $\Phi_{2;100}$ (bright to dark, dashed to dot-dot-dashed). Brown (solid) is $\Phi_{2.5;\infty}$ and blue (dotted) $\Phi_{1.5;\infty}$. The black dashes mark the minima. The calculation is done in 0.25° steps.

to be more sensitive. Benchmark energy spectra $\Phi_{\gamma;\mathrm{E_{cut}}}$ of fixed power law index γ and energy cut-off E_{cut} are chosen for the optimization. The values are listed in table 8.

This selection of energy spectra covers the whole range of parameters for the optimizations on both data sets. $\Phi_{1.5;\infty}$ has no cut-off and is the expectation with the most high energetic neutrinos. $\Phi_{2;10}$ has an energy cut-off at the transition energy between the high energy data set and the low energy data set. It is used in both optimizations. The lower bound of the low energy data set is tested by $\Phi_{2;0.1}$ with the cut-off energy at the lowest investigated values. In addition intermediate energy spectra are tested to ensure a good optimization result over the full parameter space. A special case is the energy spectrum $\Phi_{2.5;\infty}$. Due to its steep slope mostly low energetic events are expected, but the tail reaches to the highest energies. It is included as test spectrum for both data sets.

Figure 40 shows the sensitivities to the neutrino flux depending on the signal region size $\Delta\delta$ for the high energy data set. $\Delta\delta$ is changed in 0.25° steps. For all tested energy spectra the sensitivity improves with increasing signal region. Above $\Delta\delta = 2°$ to 3° the sensitivity decreases again. The shape of all optimization curves is similar and the minima are broad and flat. The major difference is the absolute scale which is not relevant for this optimization. The optimum is at $\Delta\delta \simeq 2°$ for the energy spectra with large amounts of high energetic neutrinos ($\Phi_{2;\infty}$, $\Phi_{1.5;\infty}$) and at $\Delta\delta = 2.5°$ for the others.

This difference in the optimum angle between the energy spectra is small. Due to the broad minima the loss of sensitivity is small if a value slightly different from the optimum is chosen. Only the energy spectra without an energy cut-off clearly prefer a 2° signal region size. This analysis aims at energy spectra with a cut-off and thus the analysis

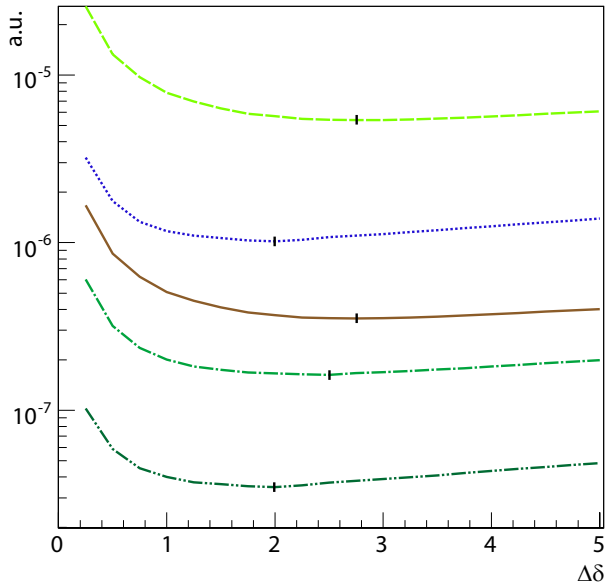

Figure 41: $Sig/\sqrt{BG}$ (in arbitrary units) for different signal region sizes $\Delta\delta$ for energy spectra with a cut-off energy smaller than 10 TeV using the low energy data set. The parameters of the energy spectra are given in table 8. In green $\Phi_{2;0.1}$, $\Phi_{2;1}$ and $\Phi_{2;10}$ (bright to dark, dashed to dot-dot-dashed). Brown (solid) is $\Phi_{2.5;\infty}$ and blue (dotted) is $\Phi_{1.5;0.1}$. The black dashes mark the minima. The calculation is done in 0.25° steps.

is done with $\Delta\delta = 2.5°$. Signal hypotheses with cut-off energies E_{cut} between 100 TeV and 1 PeV are slightly degraded in sensitivity by this choice of the region size. This loss is smaller than for the spectrum without energy cut-off. A separate analysis would not achieve a statistical improvement.

The optimization for signal hypotheses with a cut-off energy $E_{\text{cut}} < 10$ TeV is done for the low energy data set. The same procedure as for the higher energy cut-offs is used. Figure 41 shows the sensitivity to the neutrino flux depending on the signal region size $\Delta\delta$. It is varied in 0.25° steps. For all energy spectra the sensitivity improves for larger signal regions. Above about $\Delta\delta = 2°$ to 3° the sensitivity decreases again. The shape of all sensitivity curves is similar compared to the high energy results: they have broad and flat minima. Again, the major difference is the scale, which is not relevant for the optimization of the size of the source region. Only the dependency of the sensitivity for $\Phi_{1.5;0.1}$ on $\Delta\delta$ differs slightly. The decrease in sensitivity for larger search regions is slightly larger compared to the other energy spectra.

The optimum size of the signal region is similar to the one obtained in the high energy optimization. It varies between $\Delta\delta = 2°$ and 2.75°. Smaller sizes correspond to energy spectra with more high energetic events. Considering the small changes in the sensitivity around the optimum and the small differences in the optimum values $\Delta\delta = 2.5°$ is chosen for all energy spectra.

7.1.2 Optimization for a Signal from Dark Matter Particle Annihilations

The search for a signal from Dark Matter particle annihilations is performed with the low energy data set. The expected neutrinos have energies below 10 TeV. The signal region is optimized for all tested masses and all selected channels ($\chi\chi \rightarrow b\bar{b}, W^+W^-, \mu^+\mu^-, \nu\bar{\nu}$, section 4.1.1). In addition, the optimum size of the signal region depends on the selected halo model. The bin size is optimized for the most up to date models: Einasto and NFW (section 2.4.4). Their Dark Matter distributions and the resulting neutrino fluxes are similar. The other two halo models (Moore, Kravtsov) are included as a reference to estimate the model dependencies. Because they are analyzed with the signal region optimized for the Einasto and NFW halo profile, the optimum sensitivity is not achieved, here.
Figure 42 shows the sensitivity in dependence of the Dark Matter particle mass m_χ and the annihilation channel. For each configuration $Sig/\sqrt{BG}$ is calculated depending on $\Delta\delta$ in 0.5° steps. For all channels and masses the sensitivity improves with increasing signal region up to about 6° to 8° and decreases slowly afterwards. The different scales of the sensitivity are not relevant for the optimal bin size.
For the largest masses (5 TeV, 10 TeV) and annihilation channels with many high energetic neutrinos ($\mu^+\mu^-$, $\nu\bar{\nu}$) smaller angles of about 6° or 7° provide a higher sensitivity. The analysis has to be performed with the same $\Delta\delta$ for all channels, to conclude on neutrino fluxes with energy spectra between the tested spectra (section 4.1.1). 8° is favored by most masses and annihilation channels. Also at high masses the $b\bar{b}$ and W^+W^- channels favor this value. Therefore, $\Delta\delta = 8°$ is chosen as signal region size. The sensitivity at 8° is only slightly worse for hard neutrino energy spectra. The larger optimum signal region compared to the search for a point-like source arises because of the extended Dark Matter distribution.

7.2 Amount of Background Events in the Signal Region

The expected amount of background events in the signal region has to be determined from the amount of events in the off-source region (section 4.2). Equation 34 estimates the number of background events assuming a flat event distribution in right ascension. This assumption is based on the rotation of the detector with respect to extra-terrestrial objects. During each day a fixed direction of the sky is observed under all azimuth angles. This assumption is only valid up to a certain precision. Figure 43 (right) shows fluctuations up to about 1.6% in the relative amount of background events in dependence of the right ascension. The azimuth dependent detector efficiency is not completely averaged because of the on- and off-times of the detector. Off-times occur due to various reasons, often connected to human activity. The off-times are not randomly (flatly) distributed over time and thus the differences in the exposure remain as small effect visible in the right ascension. The two differently high peaks arise from the elongated shape of the detector and is further enhanced by the on-line filter.
The low energy sample contains a huge amount of events and is sensitive to fluctuations of less than 1%. Therefore, the background prediction has to be more precise and a correction for the direction dependent fluctuations is applied and is decribed in the following.
The azimuth distribution of the off-source data in the low energy data set is determined and normalized. This is the probability density function (pdf) for an event to have a certain

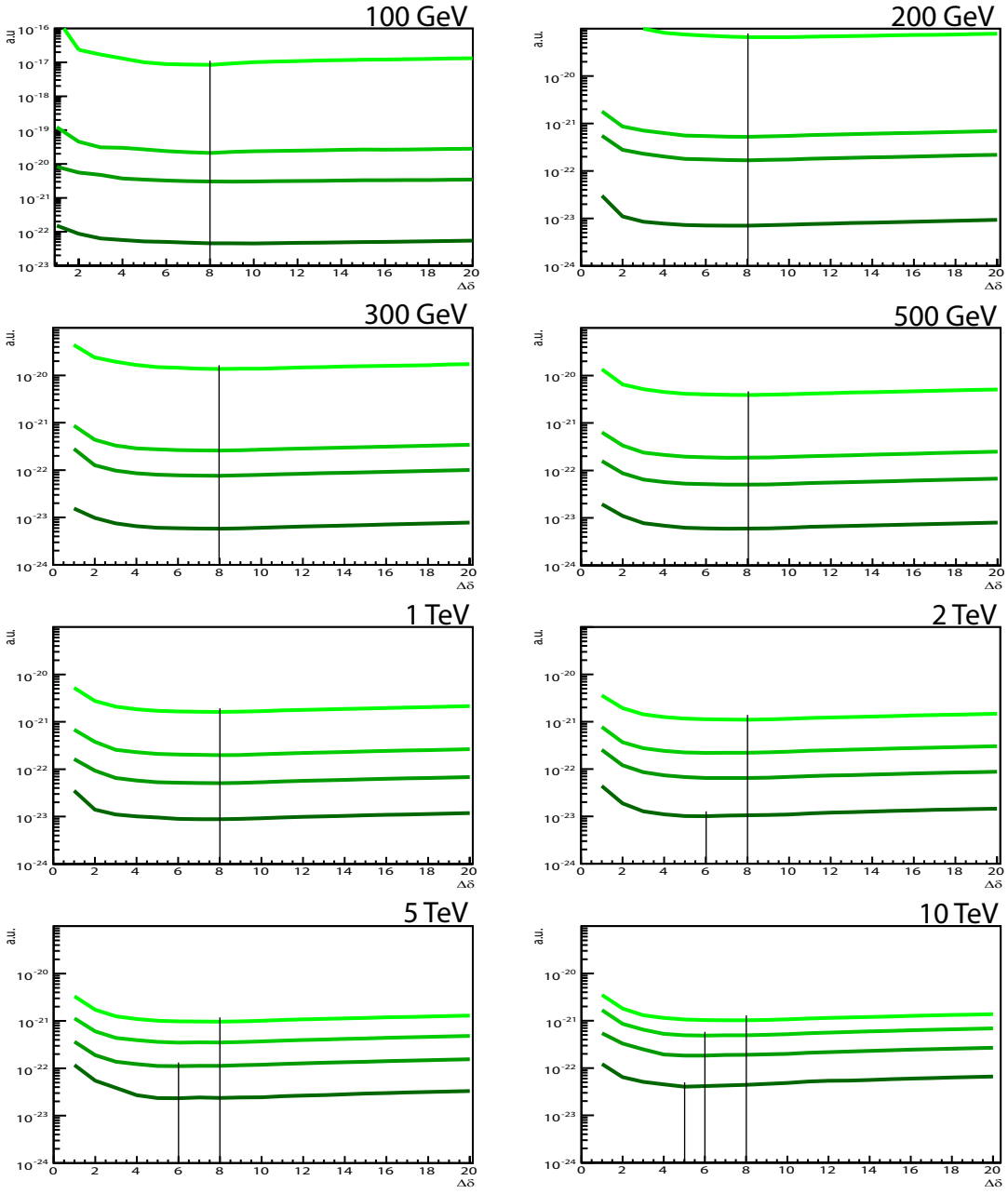

Figure 42: Sensitivity (in arbitrary units) for the Dark Matter particles annihilating in the Galactic halo using the low energy data set and the Einasto and NFW halo model in dependence of the signal region size. The figures show the optimization for different Dark Matter masses. Top left to bottom right: 100 GeV, 200 GeV, 300 GeV, 500 GeV, 1 TeV, 2 TeV, 5 TeV and 10 TeV. The four lines correspond to the different tested annihilation channels (top to bottom): $b\bar{b}$, W^+W^-, $\mu^+\mu^-$, $\nu\bar{\nu}$. The vertical black lines mark the positions of the optimums.

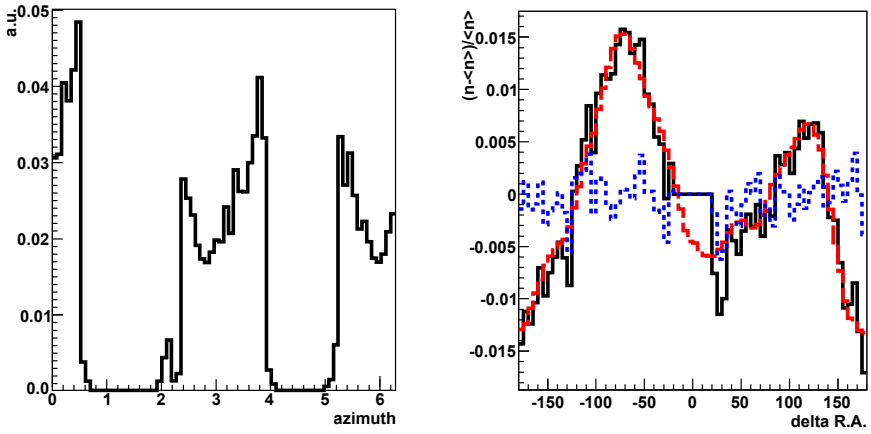

Figure 43: Left: Azimuth distribution (SPE Fit 32 Iterations) of recorded off-source events in the low energy data set (normalized to one). Right: Relative deviations of the event distribution in right ascension from a flat distribution for the low energy data set. The right ascension is given with respect to the Galactic Center. Shown are the distribution of the measured data in the off-source region (black), the expected distribution of these events as described in the text (red dashed) and the measured distribution reweighted by the expectation (blue dotted). In the off-source data the central 40° around the Galactic Center are excluded because the data from the on-source region is blinded.

reconstructed azimuth direction (figure 43, left). The on-line filter (section 6.2) applied in this analysis causes the two angular regions with hardly any events. The remaining events in these regions have a PoleSPE Fit azimuth direction in the retained range and are later shifted by the SPE-32 Fit.

The azimuth pdf $D_{\mathrm{AZI}}(t)$ rotates with the detector and gives the probability to observe an event from a certain direction at a given time. For one fixed time this probability in azimuth is the same as in right ascension (not rotating with the detector). The expected event distribution D_{RA} in right ascension is determined by:

$$D_{\mathrm{RA}} = \frac{1}{N_{\mathrm{event}}} \sum_{i}^{N_{\mathrm{events}}} D_{\mathrm{AZI}}(t_i) \; . \tag{55}$$

Here, N_{event} is the number of events in the low energy data set. AZI is always rotated such that it fits the detector position at the event times t_i. D_{RA} describes the relative exposure for different directions in the sky for background events (figure 43, right), and thus the amount of expected background events for all directions. The distribution includes seasonal variations of the background flux since a larger amount of background events at certain times contributes more to the resulting distribution.

The derived distribution fits to the measured fluctuations of the background. Both peaks are modeled with the correct shape and height. The events in the measured distribution in right ascension are weighted by the expectation in order to cross check whether all effects are taken into account. The result is shown in figure 43 (right).

The relative fluctuations of this distribution are of the order of about 0.2% and no regions with obvious over- or under-fluctuations are observed. The comparison with a flat distribution in right ascension using a χ^2-test and a Kolmogorov test results in a probability of 49% and 41%, respectively. In conclusion the fluctuations are only statistical and the background expectation describes the measurement. From this distribution the number of expected background events in the signal region is determined. For the Dark Matter analysis ($\Delta\delta = 8°$) $798.8 \cdot 10^3$ background events and for a point-like source ($\Delta\delta = 2.5°$) $84.51 \cdot 10^3$ background events are expected.
The same procedure as for the low energy data sample is repeated for the high energy sample. Here, the systematic fluctuations in right ascension are small compared to the statistical errors, due to the smaller amount of events. Therefore, the measured off-source distribution in right ascension is directly compared to a flat distribution. The result is a compatibility of 20% and 15% (χ^2-test and Kolmogorov test, respectively). Thus, this distribution can be assumed as flat. For a point-like source ($\Delta\delta = 2.5°$) 5.8 background events are expected.

7.3 Sensitivity for Neutrinos from Point-Like Sources

The sensitivity to a neutrino flux from a point-like source at the position of the Galactic Center is determined by calculating the average upper limits (90% confidence level) for each energy spectrum (equation 12). Here, the optimum search bin size of $\Delta\delta = 2.5°$ is used. For cut-off energies E_{cut} larger than 10 TeV the high energy data set is used and for energies below 1 TeV the low energy data set is used. In between the sensitivity is calculated with both data sets and the more sensitive one is chosen.
Figure 44 (left) shows the sensitivity for the high energy data set. For a fixed power law index γ the sensitivity varies more than 3 orders of magnitude between the hypotheses. For $\gamma = 2$ the sensitivity is

$$\Phi_0 = 10^{-5}\,\text{TeVcm}^{-2}\text{s}^{-1} \;\text{ to }\; 2 \cdot 10^{-9}\,\text{TeVcm}^{-2}\text{s}^{-1} \tag{56}$$

depending on E_{cut}. The sensitivity always improves with larger values of E_{cut}. The improvements for flat energy spectra (small values of γ) are larger than the improvements for steep energy spectra. This is expected, because the flat energy spectra have more events close to the cut-off energy compared to the steep spectra. The largest improvement is achieved for $1\,\text{TeV} < E_{\text{cut}} < 10\,\text{TeV}$, in the transition region between the two data sets. Comparisons for fixed E_{cut} and varying γ are not meaningful, because the units of the derived values depend on γ.
Figure 44 (right) shows the sensitivity using the low energy data set. The sensitivity is in general worse compared to the high energy data set. The dependency on γ and E_{cut} are similar: for a fixed γ the sensitivity varies more than 3 orders of magnitude. It improves with larger values of E_{cut}. For $\gamma = 2$ the sensitivity is

$$\Phi_0 = 2 \cdot 10^{-4}\,\text{TeVcm}^{-2}\text{s}^{-1} \;\text{ to }\; 3 \cdot 10^{-8}\,\text{TeVcm}^{-2}\text{s}^{-1} \tag{57}$$

depending on E_{cut}. The improvement for flat energy spectra with increasing values of E_{cut} is also observed, but it is smaller than in the high energy data set. The event distribution of the selected sample has a less sharp cut-off at low energies. A major difference to the

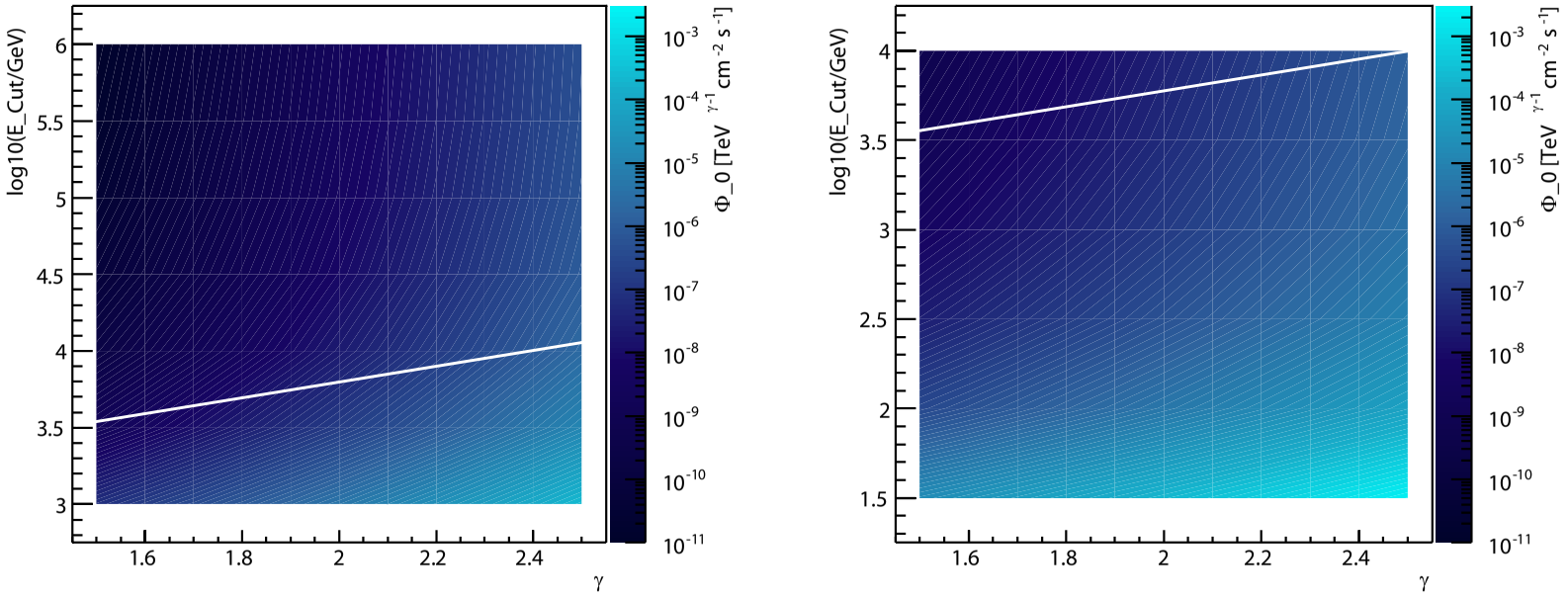

Figure 44: Sensitivity to a Neutrino Flux from the Galactic Center depending on the energy spectrum. The energy spectrum (equation 12) is characterized by the power law index γ and the energy cut-off E_{cut}. Left: Sensitivity for $E_{\text{cut}} > 1\,\text{TeV}$ using the high energy data set; Right: Sensitivity for $E_{\text{cut}} < 10\,\text{TeV}$ using the low energy data set. The white lines indicate the boundary where the low or the high energy data sample are most sensitive. The units on the z-axis depend on the power law index γ of the energy spectrum: the figure changes with a different choice of the units.

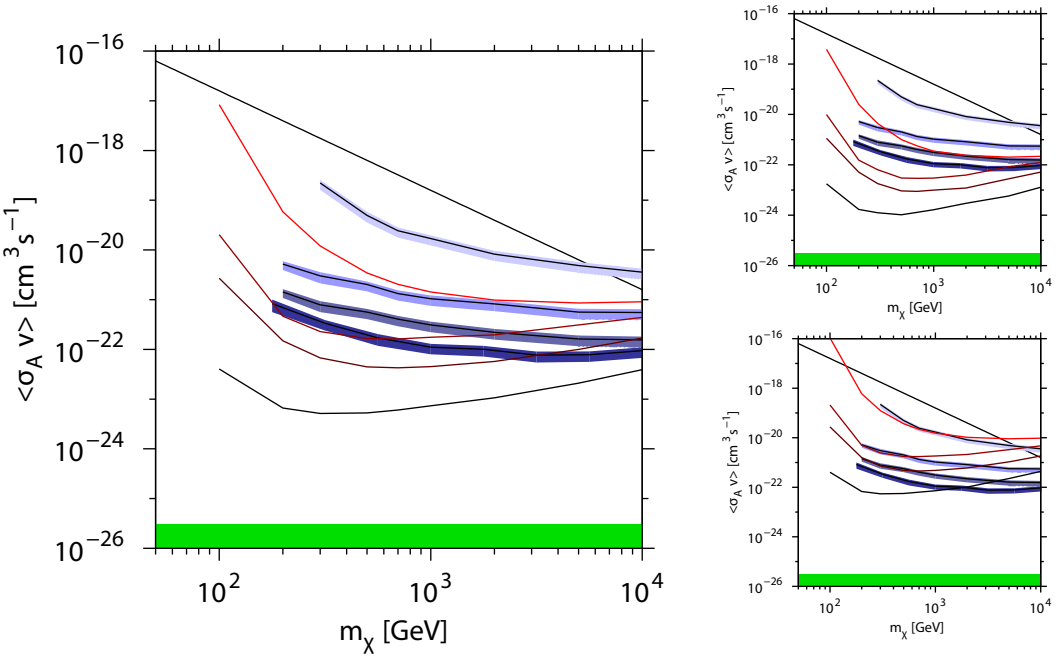

Figure 45: Left: Sensitivity to the self annihilation cross section assuming the Einasto or NFW halo profile (section 2.4.4). Black lines with the broad blue bands around them show the sensitivity for IC22 [Ice10a]. The width of the bands represents the uncertainty due to the different halo models. The red lines show the sensitivity derived by this analysis. The lines for the Einasto and NFW halo model are indistinguishable. The lowest sensitivity is achieved for the $b\bar{b}$ channel, followed by the W^+W^-, $\mu\bar{\mu}$ and finally the $\nu\bar{\nu}$ channel with the best sensitivity. Additionally the green area shows the natural scale (section 2.4.2) and the right black line is the upper bound on the self annihilation cross section given by unitarity. Top right: same as left figure, but the sensitivity for this analysis uses the Moore halo model. Bottom right: same as left figure, but the sensitivity for this analysis uses the Kravtsov halo model.

high energy data set is the roughly equal improvement over the complete tested range of E_{cut}. No large improvement for the lowest values of E_{cut} is observed.

For all values of γ and E_{cut} the more sensitive one of the low and high energy data sets is used for the analysis of the signal region. In figure 44 the transition between these two regimes is indicated. As expected the transition is between 3 TeV and 10 TeV.

7.4 Sensitivity for Dark Matter Annihilations in the Halo

The sensitivity to the self annihilation cross section of Dark Matter particles in the Galactic halo is determined by calculating the average upper limits (90% confidence level) for each Dark Matter particle mass m_χ, annihilation channel (section 4.1.1) and halo model (Einasto, NFW, Moore, Kravtsov). Here, the optimum search bin size $\Delta\delta = 8°$ and the low energy data set are used.

The derived sensitivity (figure 45) for the Einasto and NFW halo model is at the scale of

$$\begin{aligned} < \sigma_A v > &= 10^{-23}\,\mathrm{cm}^3\,\mathrm{s}^{-1} \text{ for the } \nu\bar{\nu} \text{ annihilation channel,} \\ < \sigma_A v > &= 10^{-22}\,\mathrm{cm}^3\,\mathrm{s}^{-1} \text{ for the } \mu^+\mu^- \text{ annihilation channel,} \\ < \sigma_A v > &= 3 \cdot 10^{-22}\,\mathrm{cm}^3\,\mathrm{s}^{-1} \text{ for the } W^+W^- \text{ annihilation channel,} \\ < \sigma_A v > &= 10^{-21}\,\mathrm{cm}^3\,\mathrm{s}^{-1} \text{ for the } \mathrm{b\bar{b}} \text{ annihilation channel.} \end{aligned} \tag{58}$$

The sensitivity corresponds to the amount of high energetic neutrinos for the different decay channels and depends strongly on m_χ. It improves for larger m_χ up to masses of several hundred GeV. Above, the sensitivity decreases slowly up to the maximum tested mass of 10 TeV. This dependency is independent of the halo model and the annihilation channel.
The sensitivities for the Einasto and NFW halo model are almost identical (they cannot be distinguished in figure 45). In the tested mass range the sensitivity is below the upper bound given by unitarity and thus in the physical region. Compared to the expectation from cosmological observations, the natural scale (section 2.4.2), the sensitivity is still more than two orders of magnitude weaker. A detection of neutrinos from Dark Matter particle annihilations is unlikely as long as no boost factors are considered (section 2.4.5). Compared to the analysis performed with IC22 observing the northern sky (outer Galaxy) [Ice10a] the sensitivity is improved for the whole mass range. In particular, large improvements are achieved for small values of m_χ. The improvement below $m_\chi = 500\,\mathrm{GeV}$ is more than one order of magnitude, while for $m_\chi > 10\,\mathrm{TeV}$ the improvement is marginal in the channels predicting high energetic neutrinos. The analysis of the IC22 data is performed on a data set optimized for high energy neutrino events and consequently more low energetic events are removed. The sensitivity is degraded in this energy range while the sensitivity at large masses gains from being almost background free.
The sensitivities for the Moore and Kravtsov halo model scale with the expected amount of Dark Matter in the line of sight. The highest sensitivity is achieved for the $\nu\bar{\nu}$ channel and the Moore halo profile. It is about $< \sigma_A v >= 10^{-24}\,\mathrm{cm}^3/\mathrm{s}$ and 1.5 orders of magnitude larger than the natural scale. For the halo model by Kravtsov the sensitivity decreases. In this case the sensitivity of the current analysis is roughly at the same scale as for the IC22 analysis.
The sensitivity of this analysis has a stronger dependency on the halo model than the analysis of the IC22 data set due to the different observation region. In the outer Galaxy the predictions from the halo models are similar. In the direction of the Galactic Center the differences are large (figure 9). This model dependency limits the sensitivity to the self annihilation cross section, but even assuming the halo model with the worst sensitivity (Kravtsov) the current analysis is more sensitive than the IC22 analysis for neutrino energy spectra with dominantly low energetic events or small masses. The strong dependency on the halo models also allows to test these models, which is not possible by analyzing neutrino events from the northern hemisphere.

Table 9: Expected and observed neutrino numbers in the signal regions. Additionally, the differences of these two numbers, the sensitivity and the 90% C.L. upper limit for the number of signal neutrinos are given.

	expected	observed	difference	sensitivity	limit
low energy data set, $\Delta\delta = 8°$	$798.8 \cdot 10^3$	$798.8 \cdot 10^3$	23	1152	1168
low energy data set, $\Delta\delta = 2.5°$	$84.51 \cdot 10^3$	$84.28 \cdot 10^3$	-230	373	142
high energy data set, $\Delta\delta = 2.5°$	5.8	6	0.2	5.4	5.7

8 Results

In this chapter the difference between the number of expected and measured neutrinos from the region around the Galactic Center is evaluated. This difference is used to decide, whether a signal from any kind of source is observed. These results are interpreted with respect to the different source hypotheses: Dark Matter particles annihilating in the galactic halo and neutrinos from a point-like source at the Galactic Center.

8.1 Measurement of Neutrinos from the Direction of the Galactic Center

Table 9 lists the numbers of events observed and expected (section 7.2) in the different signal regions. $798.8 \cdot 10^3$, $84.28 \cdot 10^3$ and 6 events are observed in the signal regions with $\Delta\delta = 8°$ for the low energy data set, $\Delta\delta = 2.5°$ for the low energy data set and $\Delta\delta = 2.5°$ for the high energy data set, respectively. These numbers are compared to the expected number of events. These are $798.8 \cdot 10^3$, $84.51 \cdot 10^3$ and 5.8 events, respectively.
When, considering the statistical uncertainties, the observed numbers agree in all three cases with the expected number. The largest difference between measurement and expectation is observed for the low energy data set with the smaller signal region ($\Delta\delta = 2.5°$). In this region 230 events less than expected are observed. This deviation is about -0.8σ and has a high probability of being statistical ($p > 0.8$ taking into account the 3 analyses). No under-fluctuation is observed in the larger signal region ($\Delta\delta = 8°$) of the low energy data set. Here, the signal region is about ten times larger and the result is about independent of the amount of events in the smaller signal region.
The expectation of the number of background events is determined from the experimental distribution in right ascension. Figure 46 shows this expected distribution and the distribution of the measured events for the low energy data set. The figure is similar to figure 43, but, additionally, it includes the on-source region (the central 40°). The recorded number of events in the on-source region fulfills the expectation determined in section 7.2. No significant fluctuations are observed.
All three observations are well explained by purely statistical fluctuations. No deviation from the pure background expectation is observed and limits on the possible contribution of signal neutrinos are determined.
These limits are derived according to Feldman-Cousins [FC98] with a confidence level of 90%. The confidence belts are shown in figure 47. The number of signal neutrinos is limited to be below 1168 ($\Delta\delta = 8°$) and 142 ($\Delta\delta = 2.5°$) for the low energy data set. For the high energy data set ($\Delta\delta = 2.5°$) the number of signal neutrinos is below 5.7. For

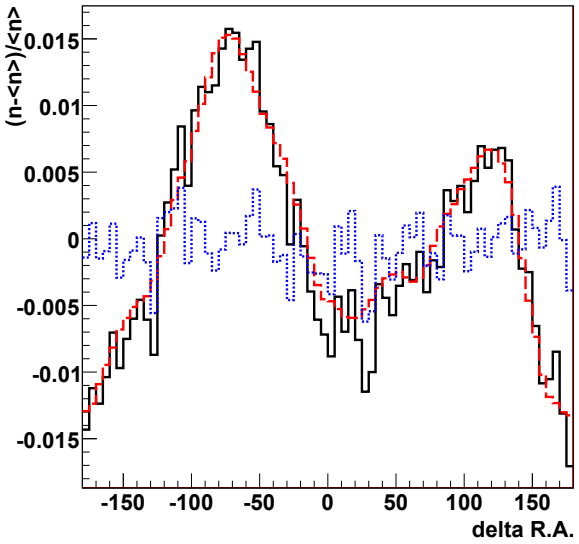

Figure 46: Deviations from a flat distribution in right ascension of the low energy data set. The right ascension is given with respect to the Galactic Center. Shown are the measured distribution (black), the expected distribution (red dashed, section 7.2) and the measured distribution corrected for the expectation (blue dotted). The figure shows the same as figure 43, but additionally including the unblinded central 40°.

comparison, the values are listed in table 9. Because of the small differences between the expected and the observed number of events the difference between the sensitivity and the limits are small except for the small under-fluctuation for the low energy data with the small signal region. The limit is about a factor 2.5 more restrictive than predicted by the sensitivity.

8.2 The Six Events of the High Energy Data Set

The surviving six events of the high energy data set are of special interest (table 10). They pass all applied selections and have a signature like a muon track with the interaction vertex inside the detector. In the following it is verified that these events have the properties expected from the simulations.

Figure 48 to figure 53 show the reconstructed muon track for each of the six events including the interaction vertex. By eye, the results match the recorded hit distribution. All tracks have in common that the first recorded hit is not at the edge of the detector. The events 1 and 3 show a large light deposition at the beginning of the reconstructed track. Event 2 also has a large light deposition, but it is not at the beginning of the track. This increased amount of light indicates a possible cascade either from the neutrino interaction vertex or a large energy loss of a muon. For event 1 and 3 both explanations are unlikely: Less than 0.1 atmospheric neutrinos are expected in the data set and the probability to have two randomly positioned cascades both at the beginning of the track is also small.

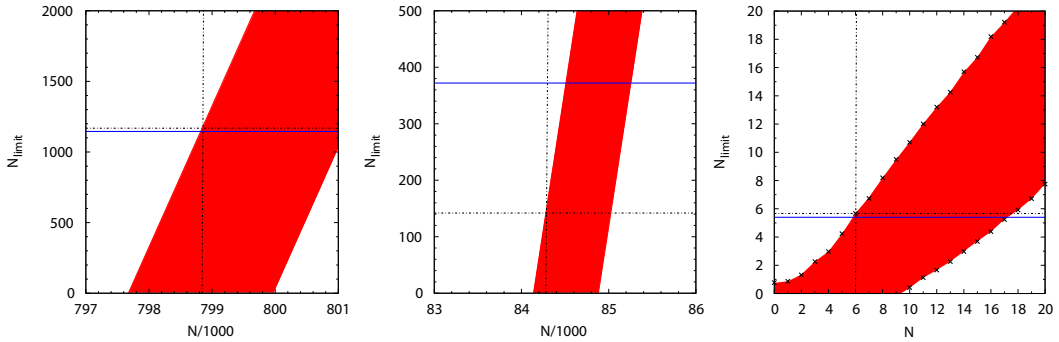

Figure 47: 90% confidence level Feldman-Cousins confidence belts for the limits on the neutrino number in the source region. Left: low energy data set and the $\Delta\delta = 8°$ signal region; middle: low energy data set and the $\Delta\delta = 2.5°$ signal region; right: high energy data set and the $\Delta\delta = 2.5°$ signal region. The x-axis shows the number of events N in the search bin, the y-axis the 90% limit on the number of signal events N_{limit}. The red shaded areas are the confidence belts. The blue dotted lines show the sensitivity. The vertical black lines (dot-dashed) are the observed numbers of events in each search bin. The horizontal black lines (dot-dashed) are the corresponding limits. Values are listed in table 9. In the right figure crosses mark the calculated points.

Table 10: Characteristics of the six events. Angles are in radian.

Nr.	Run No.	Event No.	Azimuth	Zenith	Date
1	111125	4702386	3.18	1.06	6. June
2	111340	35628460	3.24	1.05	20. July
3	111377	19056269	3.31	1.10	28. July
4	111582	16725168	0.25	1.09	2. Sep.
5	112433	16279997	5.26	1.06	18. Jan
6	113231	24587750	5.29	1.05	22. Mar.

Event 4 is special because of the two separated late hits. In addition to a muon track, possible explanations are a cascade and two hits from another object outside of the detector, or two late noise hits. A detailed investigation of this event shows that the track is in the middle between the strings for the not observed part, the reconstructed direction fits the two late extra hits as well as the early hits, the arrival time of the late hits fits to the reconstructed track and the reduced log likelihood value is $rlogl = 7.6$ which is a very good value (figure 30). Thus, this event is likely to be caused by a muon track even apart of the missing hits.

Events 5 and 6 appear smaller due to their direction in the detector. They are both close to the azimutal selection of the on-line filter. Both are at about the same position in the detector. The first hits are close to the edge of the instrumented volume and they pass close to the outer strings of the detector (figure 24). These strings should have detected a muon traveling along the reconstructed direction. Therefore, these are also starting events.

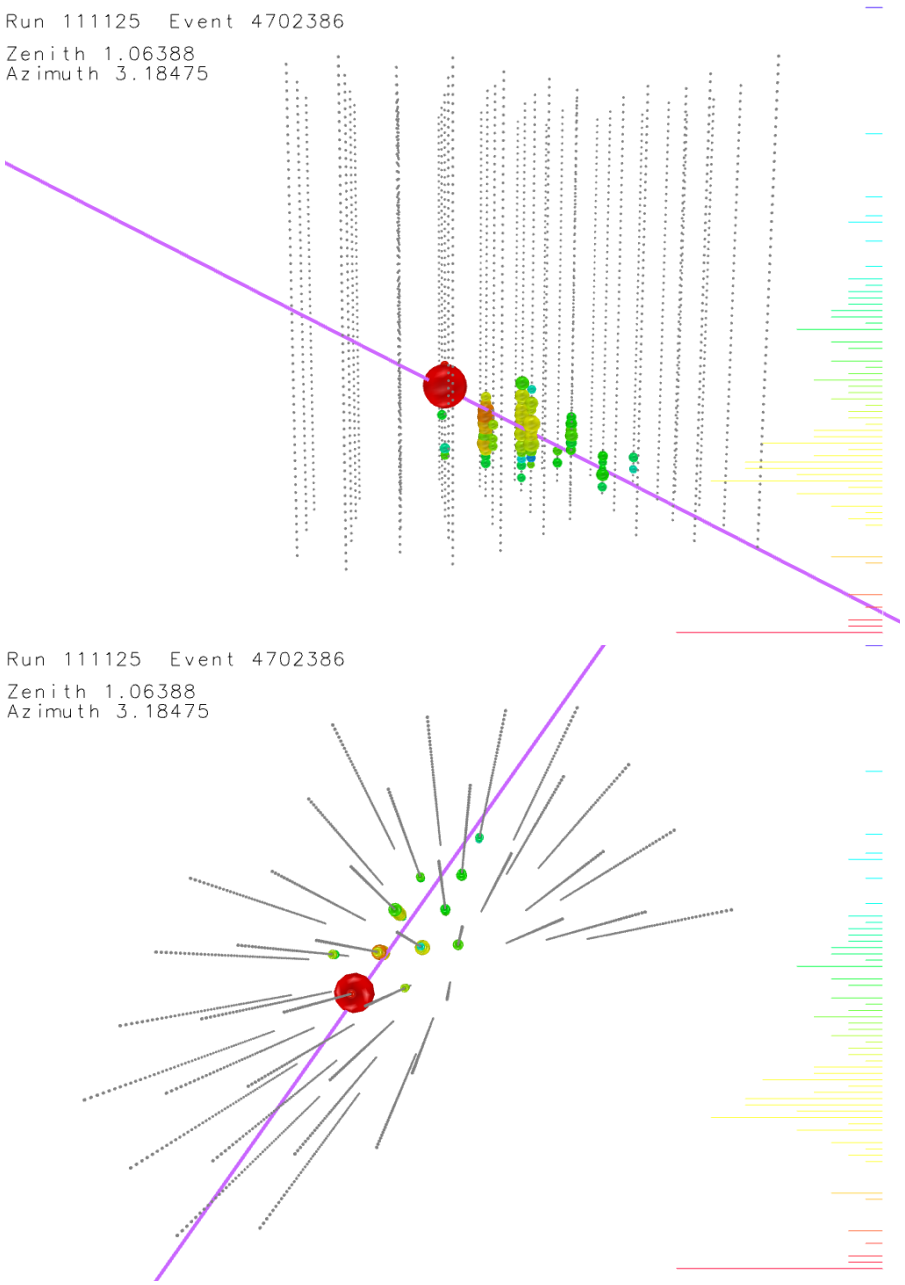

Figure 48: Event displays of event 1 which survived all selections. The gray dots are the positions of the IceCube DOMs. The colored spheres on the DOMs indicate hits: the time is given by the color coding (red to blue) and the charge by the size of each sphere. Additionally, a histogram of the hits over time is shown on the right. The long purple line indicates the reconstructed direction of the event and the purple dot is the reconstructed interaction vertex. In the upper left corner the run number, the event number and the direction of the event are listed. For this event, the purple dot for the start point is inside the sphere for the hits and not visible.

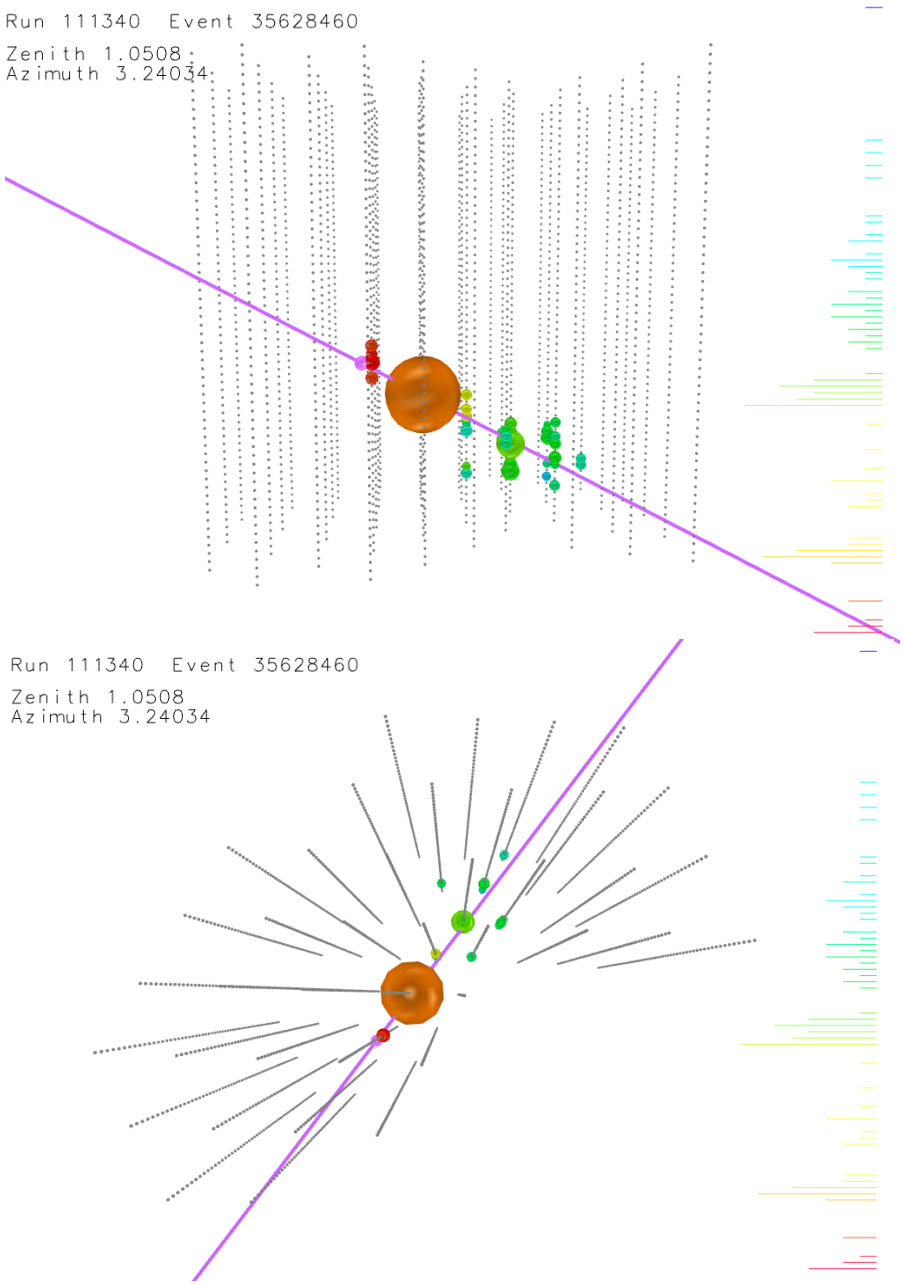

Figure 49: Event displays of event 2 which survived all selections. For a description see figure 48.

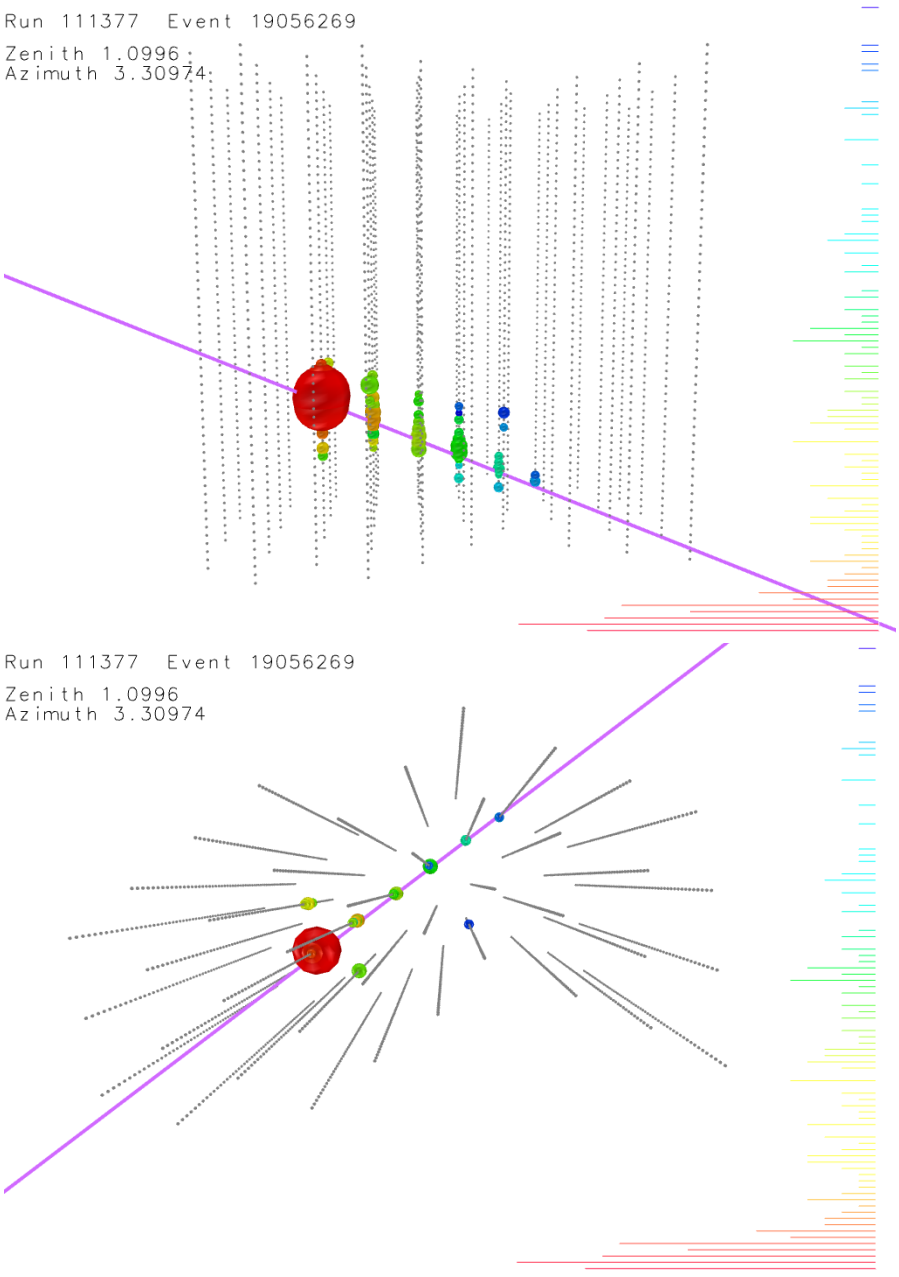

Figure 50: Event displays of event 3 which survived all selections. For a description see figure 48.

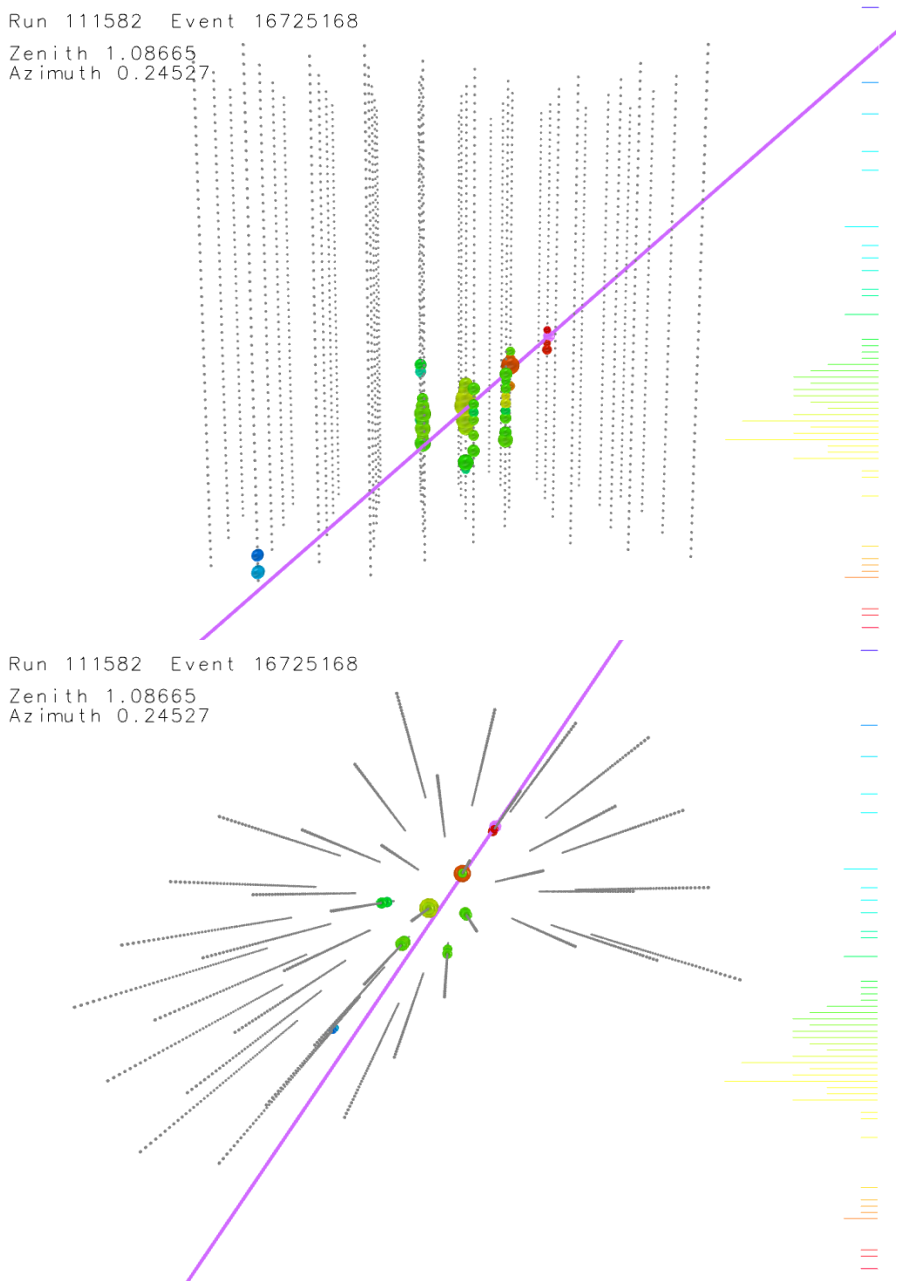

Figure 51: Event displays of event 4 which survived all selections. For a description see figure 48.

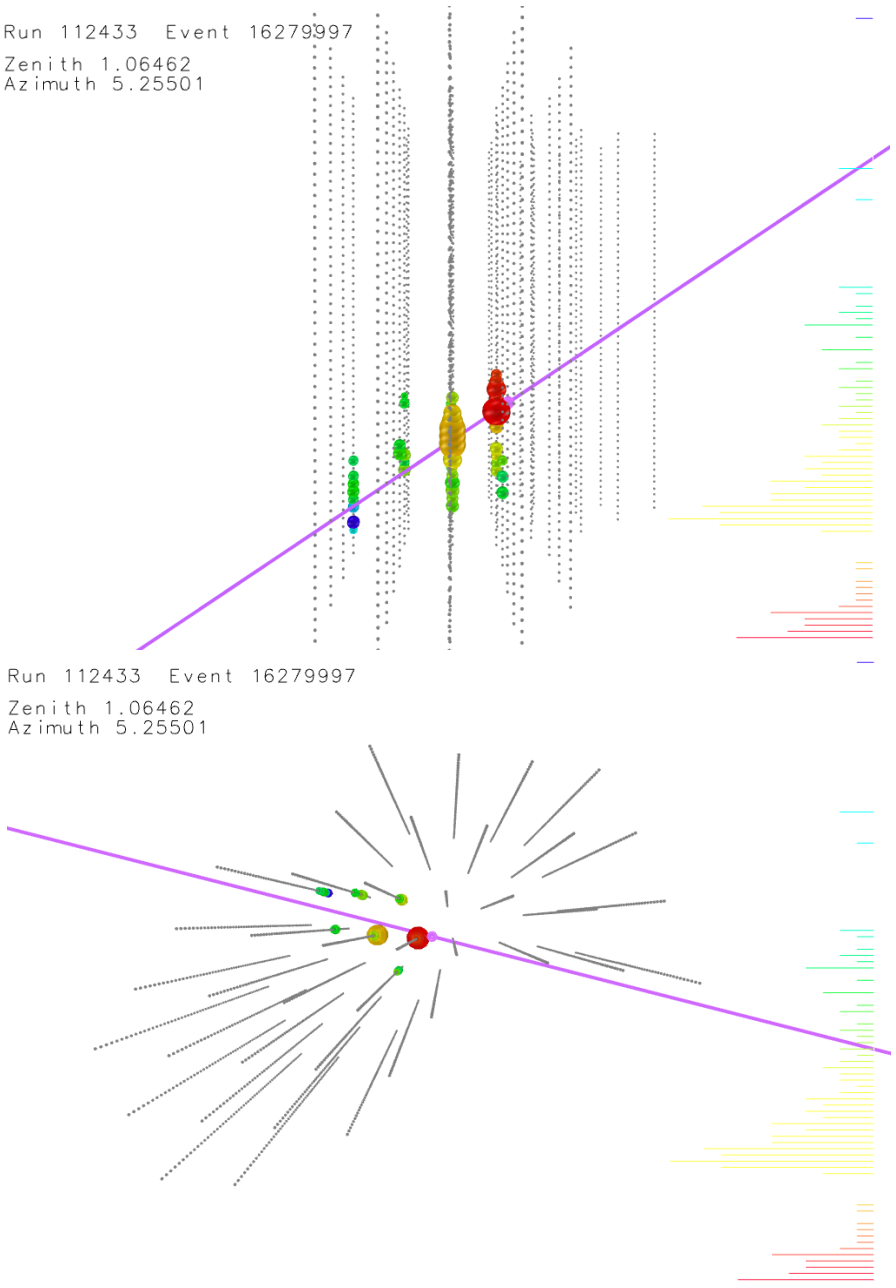

Figure 52: Event displays of event 5 which survived all selections. For a description see figure 48.

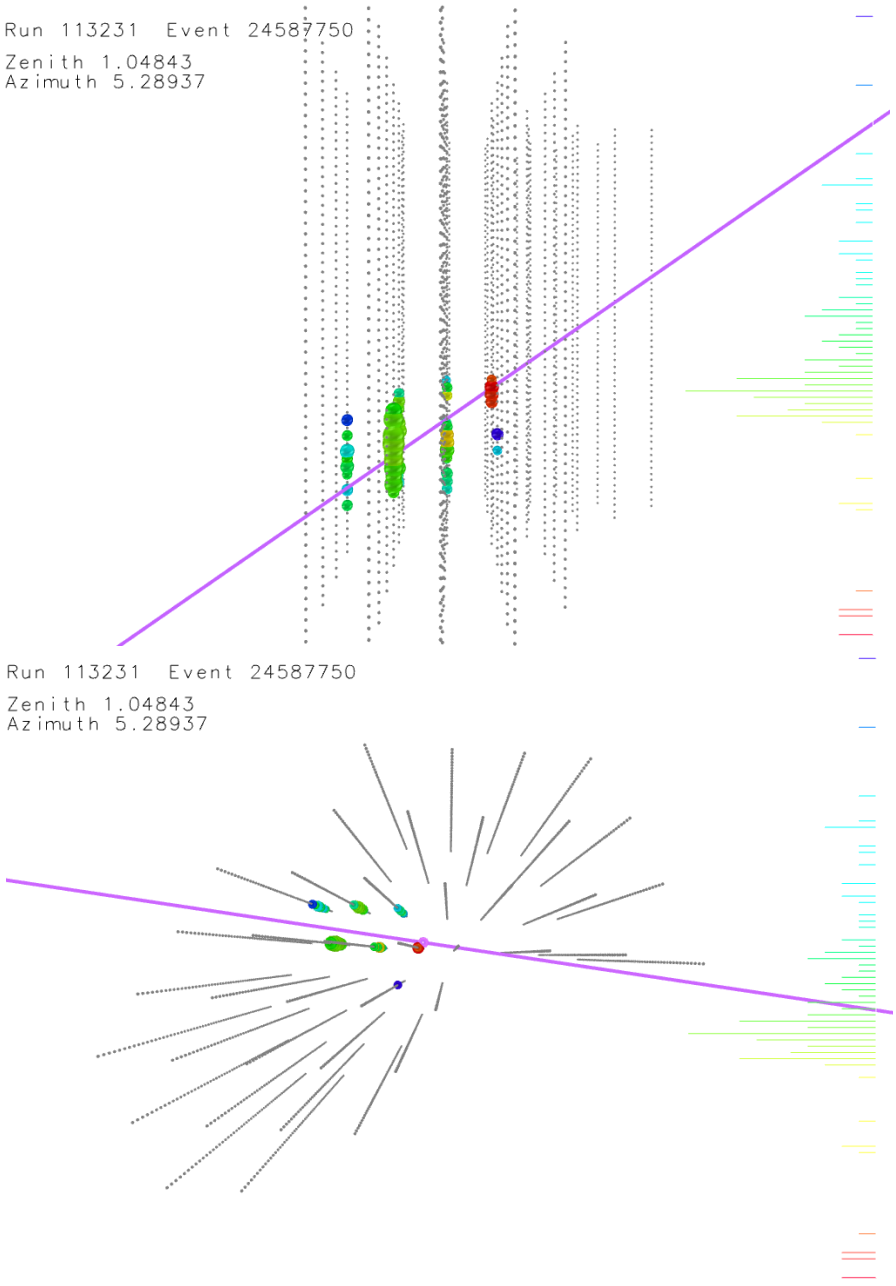

Figure 53: Event displays of event 6 which survived all selections. For a description see figure 48.

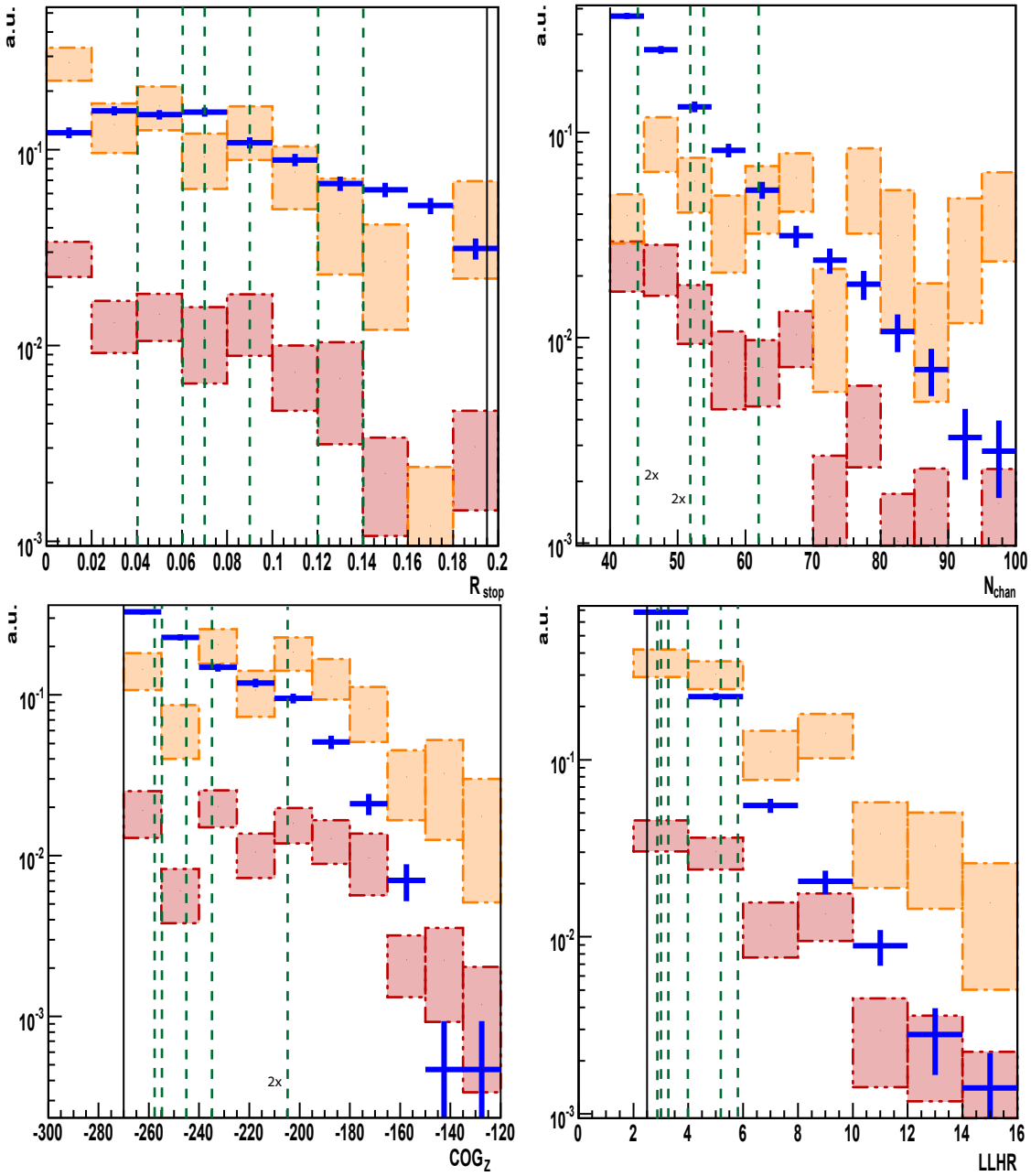

Figure 54: Distributions of the parameters used for the signal identification selections. Top left: R_{stop}; top right: N_{chan}, bottom left: COG_Z; bottom right: LLHR. The blue line shows events from the off-source region. The orange areas (dot-dot-dashed) are a neutrino signal with an E^{-2} energy spectrum and a cut-off at 10 TeV. The red (dot-dashed) areas are the distributions expected from atmospheric neutrinos, scaled to to the amount expected relative to the off-source data. The boxes show the statistical fluctuations (1σ). The vertical green dashed lines indicate the values for the six events in the signal region and the vertical black line indicates the cut values of the signal identification selection.

Table 11: Parameters of the six events. The selection parameters are given and the position relative to the Galactic Center: in declination Δ_{dec}) and right ascension Δ_{ra} and the total angular distance Δ.

Nr.	N_{chan}	R_{stop}	R_{start}	$LLHR$	COG_Z	rlogl	Δ_{dec}	Δ_{ra}	Δ
1	62	0.06	0.43	3.3	$-255\,\mathrm{m}$	7.5	$-1.4°$	$0.1°$	$1.2°$
2	44	0.07	0.38	4.0	$-205\,\mathrm{m}$	7.6	$-2.2°$	$0.9°$	$2.1°$
3	54	0.09	0.32	3.0	$-206\,\mathrm{m}$	7.0	$-1.0°$	$-1.9°$	$2.1°$
4	44	0.04	0.26	5.2	$-235\,\mathrm{m}$	7.6	$-0.6°$	$-1.2°$	$1.3°$
5	52	0.12	0.54	2.9	$-246\,\mathrm{m}$	7.4	$1.5°$	$0.1°$	$1.3°$
6	52	0.14	0.55	5.8	$-257\,\mathrm{m}$	7.8	$1.9°$	$1.0°$	$1.9°$

In addition, the observed values for the selection parameters (N_{chan}, R_{stop}, LLHR and COG_Z) are given in table 11 and shown in figure 54. They do not lie close to the selection value boundaries (table 6). Therefore, these events would remain in the data set even for more restrictive selections. All four parameters show no large deviation from the expected distributions shown in figure 37. The distribution of R_{stop} is flat as expected for background only. For N_{chan}, LLHR and COG_Z figure 54 shows an exponential decrease of background events with increasing values of the selection parameters. Therefore, the the observed values accumulate close to the cut value.

In addition to the selection parameters, also the fraction of the distance which the muon travels in the detector before the reconstructed interaction vertex R_{start} (section 52), is given in table 11. In the cleaning (section 6.3.1) events with $R_{\mathrm{start}} > 0.1$ are selected. The values of the six events are all larger than 0.25 indicating that only events which appear as starting are selected.

The six events remaining after the selections are all muon tracks which seem to start inside of the detector volume and leave it. This is exactly the signature for a neutrino induced event, which this analysis aims for. It shows that identifying these events is possible. Only due to the large background it is not possible to decide whether they are caused by an atmospheric muon or a neutrino.

8.3 Limits on Neutrinos from the Dark Matter Halo

The search for Dark Matter annihilations in the galactic halo are performed with the low energy data set and the large signal region ($\Delta\delta = 8°$). No excess is observed (table 9) and limits on the self annihilation cross section are derived.

8.3.1 Limits on Dark Matter Annihilation

The calculation is based on equation 20 for the number of expected neutrino events. It is differential in area, time, energy and observation direction. The integration over all parameters including the detector properties and filter passing rates yields the amount of expected signal events

$$N = f_i(m_\chi) J_{2,\Delta\Omega} < \sigma_A v > \ . \tag{59}$$

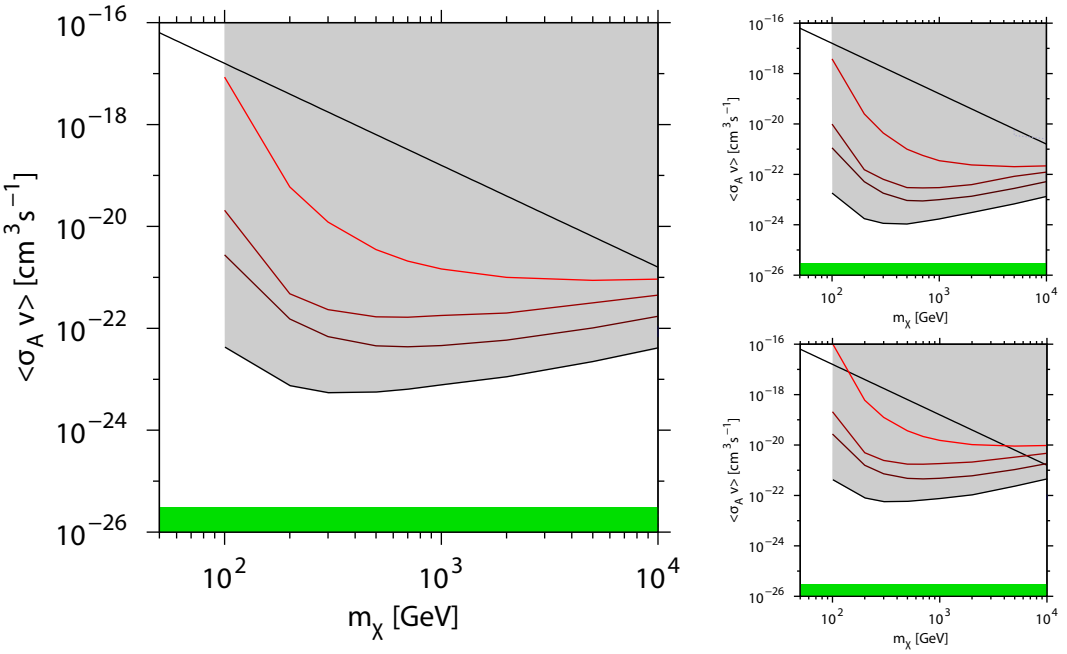

Figure 55: Left: Limits on the self annihilation cross section assuming the Einasto or NFW halo profile (section 2.4.4). The red lines are the limits derived in this analysis. The difference between the two halo models is not visible. The uppermost red line is for the $b\bar{b}$ channel (soft), followed by the W^+W^- (hard), $\mu^+\mu^-$ (super-hard) and finally the $\nu\bar{\nu}$ (line) channel. Additionally, the green area shows the natural scale (section 2.4.2) and the straight black line is the unitarity upper bound on the self annihilation cross section. Top right: same as left figure, but for the Moore halo model. Bottom right: same as left figure, but for the Kravtsov halo model. The sensitivities are not shown since they are almost identical with the limits.

The number of events is directly proportional to the mean of the self annihilation cross section times the velocity $< \sigma_A v >$ and proportional to the line of sight integral averaged over the observation region $J_{2,\Delta\Omega}$. $f_i(m_\chi)$ is a proportionality constant for a given Dark Matter particle mass m_χ and annihilation channel $i = b\bar{b}$, W^+W^-, $\mu^+\mu^-$, $\nu\bar{\nu}$. The value of f is determined by Monte Carlo simulations of signal events.

The halo models introduced in section 2.4.4 predict fixed values for $J_{2,\Delta\Omega}$ (equation 21). These are about 900 for the Moore halo model, about 240 for the NFW and Einasto halo models and about 23 for the Kravtsov halo model. These values take the differences in the relative detection efficiency of the detector into account. Events from directions close to the boundary of the signal region can be mis-reconstructed to a direction outside of the region. Due to the steeply falling density distributions this loss is larger than the gain from events accidentally mis-reconstructed into the signal region. The given values take both effects into account and therefore differ from a pure geometric calculation averaging equation 21.

Figure 55 shows ant table 12 lists the resulting self annihilation cross section limits in the tested mass range from 100 GeV to 10 TeV for all four decay channels ($b\bar{b}$, W^+W^-, $\mu^+\mu^-$, $\nu\bar{\nu}$). Due to the small difference between the measured numbers of neutrinos and

Table 12: 90% confidence level upper limits on the self annihilation cross section $< \sigma_A v >$ for the tested channels and the NFW halo profile.

channel	$< \sigma_A v >$
$b\bar{b}$	$\approx 10^{-21} cm^3 s^{-1}$
W^+W^-	$\approx 3 \cdot 10^{-22} cm^3 s^{-1}$
$\mu^+\mu^-$	$\approx 10^{-22} cm^3 s^{-1}$
$\nu\bar{\nu}$	$\approx 10^{-23} cm^3 s^{-1}$

the expected numbers (table 9), the values of the limits are almost identical to the values of the sensitivity (figure 45). The strongest constraints are achieved for the decay channels with the largest amount of high energetic particles.

The $b\bar{b}$-channel corresponds to the energy spectrum with the lowest amount of high energetic neutrinos. It predicts the neutrino event distribution for which IceCube has the lowest average sensitivity. Thus, the derived limits exclude larger cross sections assuming that all annihilations produce Standard Model particles. In case of the Einasto or NFW model cross sections larger than about $< \sigma_A v >= 10^{-21} cm^3 s^{-1}$ are excluded for masses larger than 500 GeV. Below, the limit is less restrictive. Realistic scenarios predict that Dark Matter particles produce more high energetic neutrinos, which results in stronger constraints on the annihilation cross section. The highest possible neutrino energies are produced for the direct annihilation into neutrinos. The limit is about $10^{-23} cm^3 s^{-1}$. All limits for annihilations into other Standard Model particles and their combinations are in between these two channels.

The annihilation channel into $\mu^+\mu^-$ results in the best limit if the direct production of neutrinos is suppressed. The limit is about $< \sigma_A v >= 10^{-22} cm^3 s^{-1}$. This is about one order of magnitude worse than for the direct neutrino production.

For the Moore and Kravtsov halo model the results differ by the factor given at the beginning of this chapter for the averaged line of sight integral $J_{\Delta\Omega}$. Large uncertainties for different halo models become visible: the limits can improve or worsen up to one order of magnitude. This dependency on the halo model and the amount of Dark Matter in the central region of the Galaxy enables a measurement. Figure 56 shows the 90% confidence limit on the averaged line of sight integral. The self annihilation cross section is assumed to be of the natural scale of $< \sigma_A v >= 3 \cdot 10^{-26} cm^3 s^{-1}$ (section 2.4.2). The difference between the limit and the predicted value of the line of sight integral is the same as for the self annihilation cross section and the natural scale in figure 55.

The achieved limits are more than one order of magnitude away from the values predicted by one of the halo models for the natural scale. This difference matches the observed difference between the natural scale for the self annihilation cross section and the derived limits for it. The limit derived in this way is independent of the halo model and could be compared to other predictions.

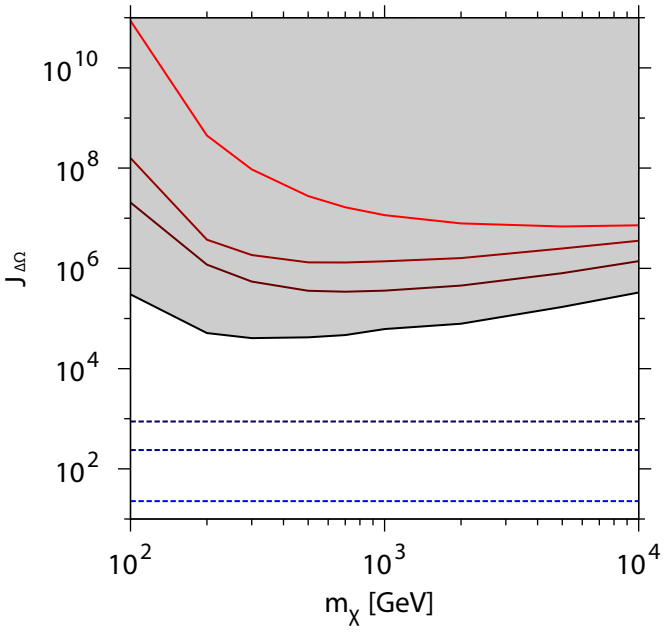

Figure 56: Limits on the averaged line of sight integral over the Dark Matter density $J_{\Delta\Omega}(\psi)$ (equation 21) assuming a value of $< \sigma_A v >= 3{\cdot}10^{-26} cm^3 s^{-1}$ (natural scale) for the self annihilation cross section. The red (solid) lines are the limits derived in this analysis. The worst limit is achieved for the $b\bar{b}$ channel (soft), followed by the W^+W^- (hard), $\mu\bar{\mu}$ (super-hard) and finally the $\nu\bar{\nu}$ (line) channel with the best limit. The blue (dotted) lines show the values for the different halo models (top to bottom): Moore, NFW or Einasto, Kravtsov.

8.3.2 Limits on Dark Matter Decay

From the results for the Dark Matter annihilation also limits for unstable Dark Matter particle candidates are inferred. A lower limit on the life time τ is determined. Integration of equation 19 yields the expected number of neutrino events:

$$N = g_i(m_\chi)\frac{J_{1,\Delta\Omega}}{\tau} \; . \tag{60}$$

The number of events is proportional to the inverse life time $1/\tau$ and the line of sight integral averaged over the observation region $J_{1,\Delta\Omega}$. $g_i(m_\chi)$ is a proportionality constant for a given Dark Matter particle mass m_χ and decay channel $i = b\bar{b}$, W^+W^-, $\mu^+\mu^-$, $\nu\bar{\nu}$. The value of g is determined by Monte Carlo simulations of signal events. Unlike the annihilation of Dark Matter, the number of neutrino events depends only linearly on the Dark Matter density. For the NFW halo profile $J_{1,\Delta\Omega}$ is 12.8.
Figure 57 shows the derived limits on the life time. At large Dark Matter masses the limits are at the order of 10^{25} s and worsen rapidly towards smaller masses. As observed for the annihilation, the most restrictive limit is achieved when assuming the direct decay into neutrinos. The decay into $\mu^+\mu^-$ results in the best limit if the direct production of neutrinos is suppressed.

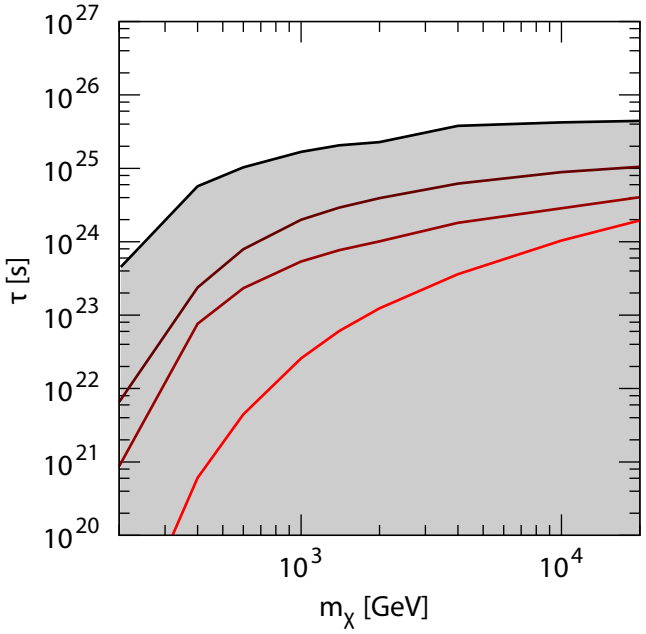

Figure 57: Limits (90% C.L.) on the life time assuming the Einasto or NFW halo profile (section 2.4.4). The difference between the two halo models is not visible. The red lines are the limits for the $b\bar{b}$ channel (soft), followed by the W^+W^- (hard), $\mu^+\mu^-$ (super-hard) and the $\nu\bar{\nu}$ (line) channel (bottom to top) derived in this analysis.

8.3.3 Limits on the Dark Matter Halo by other Experiments

Additionally to IceCube, also other experiments are sensitive to Dark Matter annihilations in the Galactic Halo (section 2.4.5). This section compares the limits obtained in this analysis to other measurements: first the results for the self annihilation and then for the decay of Dark Matter are presented.

A direct comparison is only possible for other neutrino detectors. They also limit the flux of upward going muons. Figure 58 (left) shows a comparison of the results achieved by IMB [IMB87], Baksan [B$^+$06], MACRO [Mon99], Kamiokande [O$^+$89] and Super-K [Sup04]. The limits obtained by Super-Kamiokande (Super-K) and the MACRO detector are similar and more restrictive than those obtained earlier by the other experiments. In [HNY09] the limit on the neutrino flux from Super-Kamiokande is converted into a limit on the self annihilation cross section. The limits are shown in figure 58 (right) together with the limits from the IC22 analysis observing the northern hemisphere [Ice10b] and the limits obtained by this analysis. The comparison is done for the NFW halo model and only for those channels which are tested in all three analyses.

The difference between the limits derived by the IC22 analysis and the current analysis is similar to the difference of the sensitivities (section 7.4). For all Dark Matter masses this analysis is more restrictive (independent of the annihilation channel) than the IC22 analysis. The largest improvement is achieved at several 100 GeV. For higher energies the improvement is smaller. The limits obtained by Super-Kamiokande are in between the two different IceCube limits. They depend less on the mass of the Dark Matter particle and

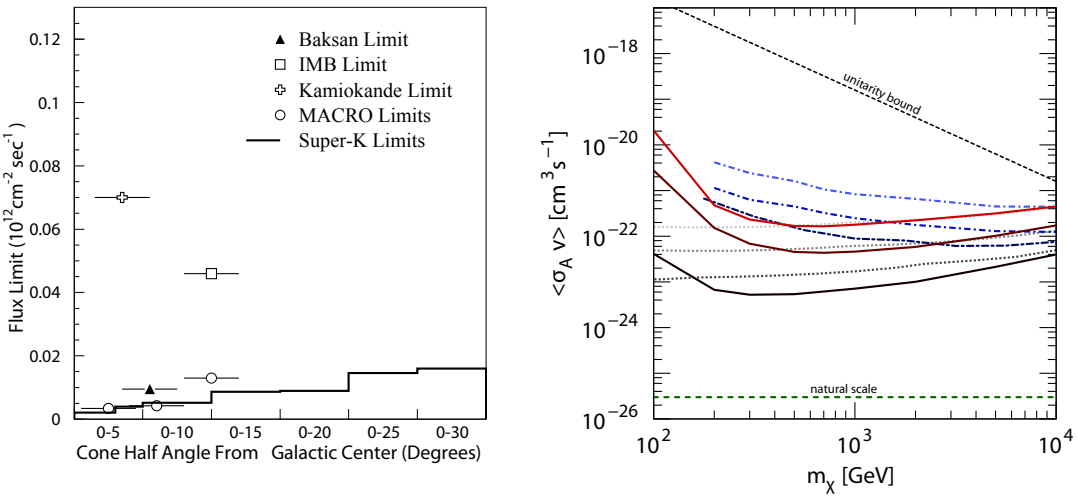

Figure 58: Left: 90% confidence level limits on the upward muon flux averaged for different opening angles by different experiments. Figure from [Sup04]. Right: IceCube limits for the NFW halo profile on the self annihilation cross section with IC22 observing the northern hemisphere [Ice10b] (three blue dot-dashed lines) and with IC40 observing the Galactic Center (three red lines). Additionally, the limits obtained by Super-Kamiokande are shown [HNY09] [Sup04] (three dotted lines). In all cases 90% confidence level limits for the W^+W^-, $\mu^+\mu^-$ and $\nu\bar{\nu}$ annihilation channel (top to bottom) are shown. The unitary bound is shown by the black short dashed line and the natural scale by the green dashed line.

become more restrictive than IceCube below about 200 GeV. The similar values for the limits of IceCube and Super-Kamiokande are explained by the different size of the detectors (IC40 is about four orders of magnitude larger than Super-Kamiokande) and Super-K has a smaller amount of background events (about six orders of magnitude). Therefore, the capacities of the detectors are similar and the differences of the limits depend on details of the analyses. At the lowest energies the neutrinos are not efficiently detected with IceCube and the limits are weaker while Super-Kamiokande has a nearly constant sensitivity at these energies due to a less energy dependent detection technique.

The limits derived from neutrinos are less restrictive than the limits from γ-rays or electrons and positrons (section 2.4.5). Depending on the decay channel the difference varies between one order of magnitude and two orders of magnitude (figure 59). The γ-ray limits always depend on the modeling of the other sources within the field of view and are thus affected by different systematics. The independence of the neutrino observation from assumptions for foreground sources and cosmological properties results in robust limits. In case of an observation of Dark Matter annihilations by one particle type, the confirmation by other detection channels and particularly the neutrino channel would be important.

The limit set by the observation of the CMB is independent of many of the uncertainties due to the Dark Matter distribution and other sources. It depends on the model for the evolution of the Universe.

Similar to the limits on the self annihilation cross section in figure 59, figure 60 also compares the limits on the life time to these obtained by other experiments. The results are similar to the limits from Super-Kamiokande. The limits from Fermi LAT are about

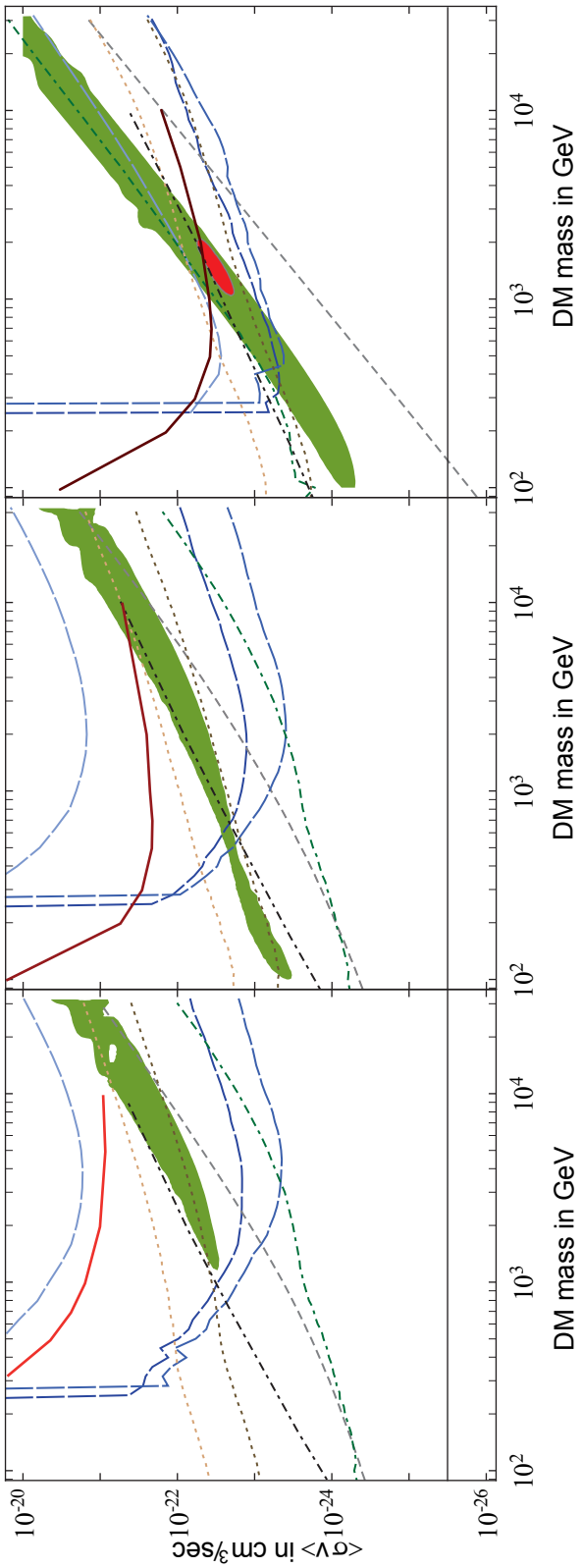

Figure 59: Upper limits (3σ) from various experiments on the self annihilation cross section assuming an NFW or Einasto halo profile. Left: annihilation into $b\bar{b}$; middle: annihilation into W^+W^-; right: annihilation into $\mu^+\mu^-$. (compare to figure 10 and explanations in section 2.4.5). The red to dark red solid lines are the limits (90% C.L.) from this analysis. Blue (long dashed) limits are derived by HESS observations of the Galactic Center (GC), Galactic Center Ridge (GR) and dwarf spheroidal galaxies. The green (dot dash dashed) limit is set by FERMI assuming final state radiation of photons and the brown (dotted) lines assuming inverse compton photons (diffusive volume $L = 1$ kpc is the bright curve and 4kpc is the dark curve)). The gray (dashed) curve refers to the GC-radio bound by observations of the central black hole. The black (dot dashed) limit is set by WMAP observations of the CMB. The green region denotes the values favored by the PAMELA excess and the red region is favored also including the FERMI $e^{\pm}$ excess. Figures modified from [PS09].

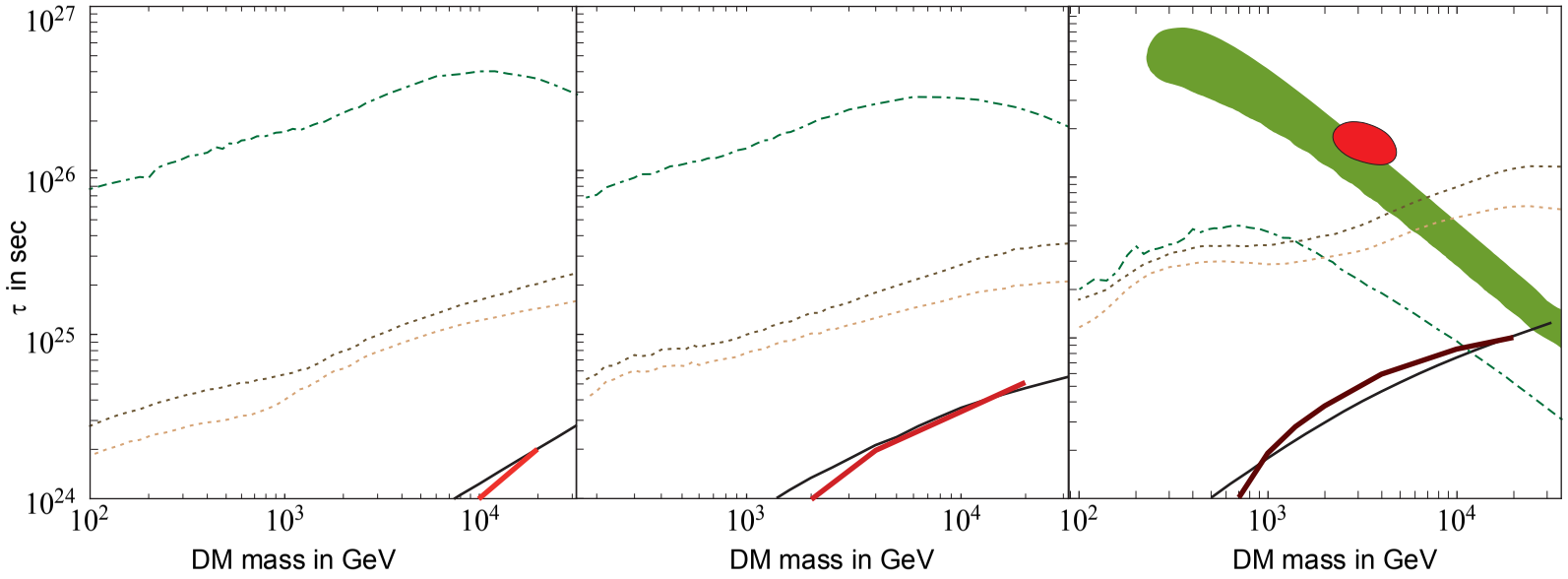

Figure 60: Lower limits (3σ) from various experiments on the lifetime assuming an NFW halo profile. Left: decay into $b\bar{b}$; middle: decay into W^+W^-; right: decay into $\mu^+\mu^-$. (Compare to figure 11 and explanations in section 2.4.5.) The light red to dark red solid lines are the limits (90% C.L.) from this analysis. The green (dot dash dashed) limit is set by FERMI assuming final state radiation of photons and the brown (dotted) lines assuming inverse compton photons (diffusive volume $L = 1\,\mathrm{kpc}$ is the bright curve and $2\,\mathrm{kpc}$ is the dark curve)). The solid black lines are 90% C.L. limits by Super-Kamiokande. The black (solid) line is the limit set by Super-Kamiokande (90% C.L.). The values favored by the PAMELA excess lie in the green region and the red region is favored including the FERMI $e^{\pm}$ excess. Figures modified from [PS09].

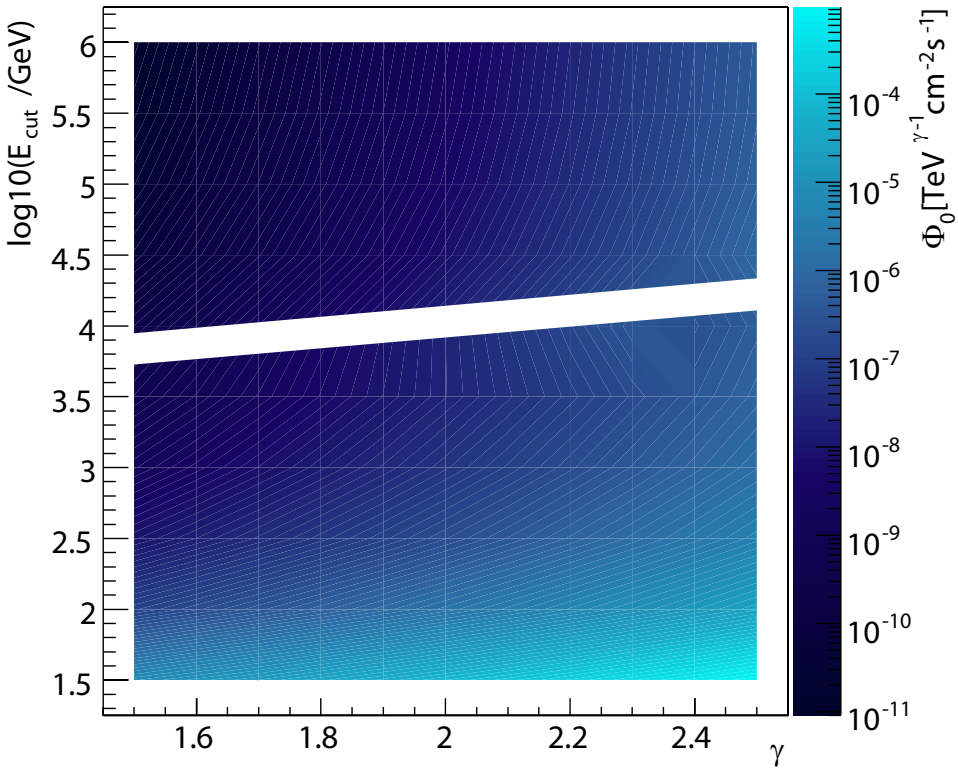

Figure 61: Limit on a neutrino flux from a point-like source for various spectral indices of the energy spectrum γ and cut-off energies E_{cut} (equation 61). The white band marks the transition between the used data sets: below the low energy data set is used, above the high energy data set. The units on the z-axis depend on γ.

one or two orders of magnitude more restrictive assuming photons from inverse Compton scattering or final state radiation, respectively. This behavior is slightly different in case of a decay into muons. Here, the limit from final state radiation is less restrictive at large Dark Matter masses. The parameter region favored by the PAMELA and HESS results is not reached by this analysis.

8.4 Limits on a Flux from a Point-Like Source

The search for neutrinos from a point-like source at the position of the Galactic Center is performed partly with the low energy data set and partly with the high energy data set for the small signal region ($\Delta\delta = 2.5°$). The more sensitive data set is chosen as explained in section 7.3. The transition occurs approximately at cut-off energies of $log10(E_{\text{cut}}/GeV) = 3.5 - 4$: above this the high energy data set is used. In both regions no excess is observed and limits on the self annihilation cross section are derived.
The calculation is based on equation 12 for the number of neutrino events N. It is differential in area, time and energy. The integration over all parameters including the detector properties and filter passing rates yields the amount of expected signal events

$$N = f(\gamma, E_{\text{cut}})\Phi_0 \; . \tag{61}$$

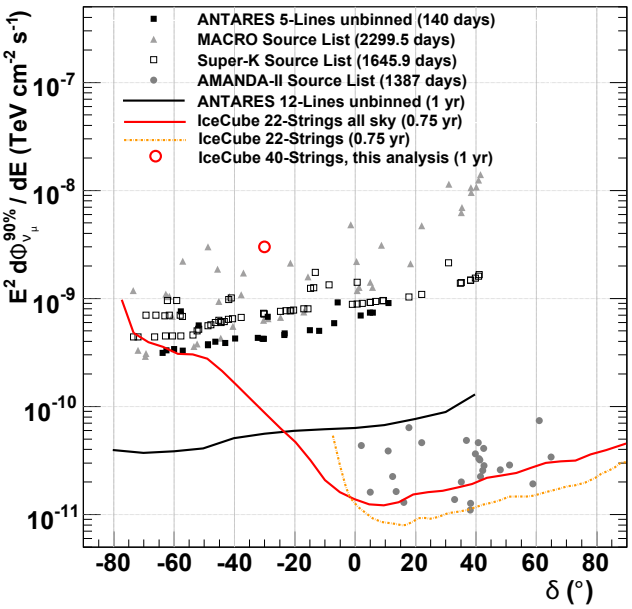

Figure 62: Limits (90% C.L.) on the muon neutrino flux by various analses. A energy spectrum with $\gamma = 2$ and no energy cut-off is used: only MACRO uses $\gamma = 2.1$ and for this analysis the result with a energy cut-off at 1 PeV is shown. The ANTARES results are from [Tos09](the 5-Lines result are limits and the 12-Lines is the sensitivity). The MACRO results are from [MAC01]. The Super-Kamiokande results are from [Sup08]. The AMANDA-II results are from [Ice09e] and the IC22 results are from [Ice09c] [Ice09b]. Figure modified from [Tos09].

The number of events is directly proportional to the flux normalization Φ_0. $f(\gamma, E_{\text{cut}})$ is a proportionality constant. It depends on the power law index of the energy spectrum γ and the cut-off energy E_{cut}. The value of f is determined by Monte Carlo simulations of signal events.

The derived upper limits are shown in figure 61. They depend strongly on the power law index γ and the energy cut-off E_{cut}. For a fixed spectral index the limit improves with increasing energy cut-off. The size of the improvement is several orders of magnitude and it depends on the power law index γ. Particularly for small power law indices large improvements are achieved. A comparison at a given cut-off energy is not meaningful due to the different units of $\Phi_0[TeV^{\gamma}]$.

The here derived limits are the first measurements from IceCube observing the southern hemisphere at neutrino energies below 1 PeV. In [Ice09b] limits (90% C.L.) are derived for various sources assuming a power law energy spectrum with $\gamma = 2$ and no cut-off. The limits lie between $E^2dN/dE \approx 1.5 \cdot 10^{-11}\,\text{TeV/cm}^2\text{/s}$ and $E^2dN/dE \approx 5.6 \cdot 10^{-10}\,\text{TeV/cm}^2\text{/s}$ depending on the declination (figure 62). This is compared with the limit from this analysis using the same spectral index and the highest possible energy cut-off ($E_{\text{cut}} = 1\,\text{PeV}$). With a value of $E^2dN/dE \approx 3 \cdot 10^{-9}\,\text{TeV/cm}^2\text{/s}$ the limit is about one order of magnitude less restrictive. This comparison is only meaningful for an assumed energy spectrum without cut-off. If the cut-off energy is well below 1 PeV only the current analysis is sensitive to the signal.

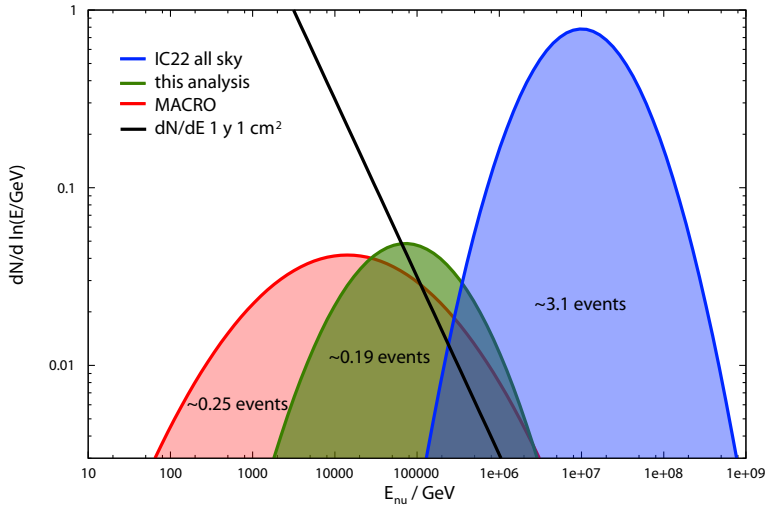

Figure 63: Energy distribution of the events in the data sets used to derive the limits shown in figure 62 for this analysis (high energy data set), IC22 all sky [Ice09c] and MACRO [MAC01]. All distributions are scaled to a flux of $E^2 dN/dE = 10^{-10}\,\mathrm{TeV/cm^2/s}$.

8.5 Measurements of the Neutrino Flux by other Experiments

The neutrino flux from the direction of the Galactic Center was also measured by MACRO [MAC01], Super-Kamiokande [Sup09][Sup08] and ANTARES [Tos09]. These three detectors have the advantage to observe the Galactic Center with the Earth as shield against muons.

Figure 62 shows the different limits in dependence of the direction of the observation. The limit derived in this analysis is less restrictive than all other limits, but competitive to the ones from MACRO due to their large spread. The limits for the Galactic Center by MACRO ($6.5 \cdot 10^{-10} TeV/cm^2/s$), Super-Kamiokande ($7.3 \cdot 10^{-10} TeV/cm^2/s$) and ANTARES 5-Lines ($4 \cdot 10^{-10} TeV/cm^2/s$) are a factor of two to three more restrictive.

For ANTARES 12-Lines the sensitivity is also shown in figure 62. This configuration will be about one order of magnitude more restrictive than the limits set up to now [Tos09].

For the interpretation of these limits always the minimum detection energy has to be considered. For the direction of the Galactic Center these are some GeV for MACRO, about 1.6 GeV for Super-Kamiokande, about 10 TeV for ANTARES and approximately 1 PeV for the shown IceCube analyses. In this analysis the lower energy threshold is at about 100 GeV. This is even below the ANTARES threshold. Thus, energy spectra with cut-off energies between 100 GeV and 10 TeV are not limited by ANTARES measurements, but by the current analysis.

The dominant contribution of expected signal events in Super-K and MACRO is below $\sim$ 50 TeV and is at about $\sim$ 100 TeV for this analysis. Figure 63 shows the expected energy distribution of the events in the high energy data set for this analysis, the standard IceCube analysis and MACRO, all scaled to the same flux. In the energy range between about 20 TeV and 300 TeV the data set for this analysis contains more events than the

other data sets. Thus, this analysis is best for sources emitting the dominant component of the neutrino flux in this energy range.
The result shows that IC40 cannot compete with former searches for a neutrino flux from the direction of the Galactic Center in the here tested energy range. The main reason is the huge amount of background in the current analysis. The detector configuration of IC40 prevented the efficient removal of this background. However, it is encouraging that a search for neutrinos from the Southern Hemisphere is possible with IceCube and that the limits set by MACRO, Super-Kamiokande and ANTARES are in reach. In the future, the complete IceCube detector including DeepCore will strongly improve the IceCube results. This is discussed in the following chapter 9.

9 Outlook to the Full IceCube Detector with DeepCore

The here presented analysis uses the IceCube detector in its 40 string configuration. It was in operation from April 2008 till May 2009. Thanks to the ongoing construction IceCube consists to date of 79 strings and the construction will be completed in February 2011 with 86 strings in the ice (section 3.2). 15 of these strings form the DeepCore sub-detector (section 3.2.2). IC79 and the final IC86 detector have a substantially higher sensitivity for neutrinos from the direction of the Galactic Center because of various achievements (for details see [Ice10b]):

- the larger detector,
- the DeepCore sub-detector being significantly more efficient for low energetic events,
- the higher quantum efficiency of the added photomultipliers,
- the change from HLC (section 3.2.5) to a less restrictive pulse cleaning (SLC),
- an operational veto.

These improvements are discussed in the following in details.
The volume of the full IceCube detector is about twice as large as the volume of the IC40 detector used in this analysis. This increases the amount of recorded signal and background events roughly by a factor of two. Additionally, the detector is nearly symmetric in the azimuth direction (figure 14); there will be no thinner or thicker directions as for IC40. An azimuth selection is not necessary. This doubles the amount of signal and background events. Considering only these changes, the sensitivity for signal is expected to improve by a factor of four.
The DeepCore sub-detector creates a more densely instrumented volume in the center of IceCube and enhances the sensitivity for low energetic events. It increases the amount of recorded pulses for all muons passing through it. With this enhanced number of pulses the detector triggers more low energetic events, which might have failed the trigger conditions without the extra DOMs. For events fulfilling the trigger conditions anyway, the additional pulses substantially improve the reconstruction due to more available information and the selection efficiency. This is particularly important for the analysis of neutrino events below 1 PeV from the southern sky. These events are identified by the interaction vertex inside of the detector. Therefore, the neutrino needs to traverse a section of the detector before being seen. It is particularly important to record many pulses in the remaining sensitive volume.
The higher quantum efficiency of the additional photomultipliers is similar to having more DOMs in the ice: more pulses are recorded.
The HLC cleaning discussed in section 3.2.5 has been replaced in IC59 by the so called Soft Local Coincidence (SLC). Unlike the HLC cleaning, the SLC cleaning keeps all hits. For the hits which do not fulfill the local coincidence requirement only time and amplitude are kept. Most of the additionally recorded hits are caused by noise and only a small fraction originates from Cherenkov light. Thus, a newly developed cleaning is applied to remove these noise pulses. This cleaning is based on a causality criterion with respect to the HLC pulses. Isolated pulses, which might originate from a muon track, are kept. This increases

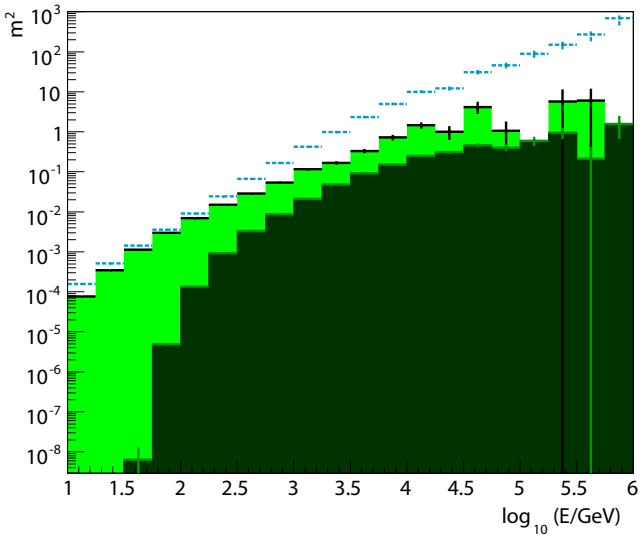

Figure 64: Effective Area after the on-line filter for IC86 (light green area) as proposed in [Ice10b] and for this analysis (dark green area). For IC86 the effective area is averaged over the southern hemisphere. For this analysis it is the effective area towards the Galactic Center. Additionally the blue dashed line shows the effective area for IC86 at trigger level.

the chance to observe a part of the muon track particularly in the Dust Layer or if it is passing in between strings. As discussed in section 6.3.3 the HLC cleaning of the recorded pulses increases the amount of muons mimicking a neutrino interaction vertex inside of the detector. The additional pulses which pass the SLC cleaning reduce the number of these background events.
Additionally, a new on-line filter for starting events is tested with the current IC79 detector in parallel with a modified version of the Starting-Downgoing-Filter. The version of the Starting-Downgoing filter has a relaxed top veto to record also pulses above the Dust Layer. It focuses on the direction of the Galactic Center.

9.1 The new Veto Algorithm

The new veto aims at neutrinos interacting in the DeepCore volume [Wie09]. Due to the smaller volume the focus is on energies below 100 GeV. The filter is based on an algorithm called 'velocity veto'. For each HLC hit not in DeepCore a velocity v_i is calculated

$$v_i = \frac{|<\vec{x}>_{\mathrm{DC}} - \vec{x}_i|}{<t>_{\mathrm{DC}} - t_i} \tag{62}$$

$<\vec{x}>_{\mathrm{DC}}$ and $<t>_{\mathrm{DC}}$ are the mean position and time of all hits recorded inside DeepCore. $\vec{x}_i$ and t_i are position and time of the non DeepCore hits. v_i is the velocity required to move from the DOM with this pulse to the average DeepCore position $<\vec{x}>_{\mathrm{DC}}$. If v_i is about the speed of light, then the non-DeepCore hit is likely to originate from the same source as the hits in DeepCore (a relativistic particle is assumed). In this case the event is assumed to be not starting and is discarded.

Figure 64 shows the effective area for the IC86 detector on trigger level and after the velocity veto as on-line filter in comparison to this analysis. The velocity veto reduces the amount of background by three orders of magnitude. This performance is similar to that of the Starting-Downgoing-Filter (table 7). Therefore, a comparison based on the neutrino effective areas is possible.

The effective area at trigger level increases with the neutrino energy. In comparison to this analysis, no cut-off appears for the velocity veto at low energies due to a modified trigger condition. It uses a SMT-3 for the DeepCore strings instead of the SMT-8 trigger for IceCube (section 3.2.6). Both are only based on HLC pulses.

The loss of signal events by the velocity veto as on-line filter is minimal for about 100 GeV. At smaller energy (10 GeV) the loss is only 50%. The lowest energetic events are triggered in the DeepCore part. For higher energies a larger fraction of signal events is lost. At neutrino energies of 10 TeV already more than 90% of the neutrino events are removed. This loss appears because the filter concentrates on the DeepCore volume. At these energies neutrino events are usually not starting inside the detector and most signal muons also enter the detector from outside. They are not required to be located in the DeepCore region and thus they are often discarded. This on-line filter is optimal for neutrino energies between several 10 GeV and about 500 GeV. It has the potential to improve an analysis like the here presented in the lower energy regime.

Figure 64 also shows the effective area after application of the on-line filter which is used in this analysis. The area is smaller than for IC86 over the shown energy range. The increase of the effective area with IC86 is particularly large at the lowest energies due to the improved capabilities.

9.2 Sensitivity of the full IceCube Detector

After the on-line filters, the reconstruction of the interaction vertex (section 5.1.2) and the likelihood ratio LLHR (section 6.3.4) developed in this analysis are used for a further filtering, the so-called ν-selection. Table 13 shows the signal and background passing rates for the combination of the velocity veto and the ν-selection compared to this analysis. For IC86 the about a factor 10 larger effective area for the signal is considered. The listed values are derived from simulations. They are not on a final analysis level and further improvements may enhance the sensitivity.

With IC86 the sensitivity (given by $\mathrm{Sig}/\sqrt{\mathrm{BG}}$) is improved by more than 2 orders of magnitude in the low energy range (compare table 13, lines 3 and 7). This improvement is based on the higher trigger rate of DeepCore and the effective background rejection by the ν-selection. For energy spectra with more high energetic neutrinos the improvement is smaller (table 13, lines 4 and 9). Here, the sensitivity is improved by a factor of three when using the combination of velocity veto and ν-selection. Here, the velocity veto is not optimal, because it is designed for low energetic events. The Galactic Center on-line filter is used for an estimate. This on-line filter is already more than one order of magnitude more sensitive than the on-line filter used in this analysis (table 13, lines 2 and 11) and a factor of six more sensitive than the high energy data set in this analysis. For the upcoming analyses the sensitivity of Galactic Center data set will increase further with the application of a ν-selection. An improvement similar to the ν-selection for the DeepCore

Table 13: Passing signal and background fractions after the on-line filter and for the low and high energy data set of this analysis and estimated passing rates for IC86. The amount of signal at trigger level is set to 1 for this analysis and about a factor of 10 more signal is recorded by the IC86 triggers (see text). Sig/$\sqrt{\text{BG}}$ is in arbitrary units. The 'low E spectrum' labeled values are for energy spectra with no events with an energy above 10 TeV). For energy spectra with events above this energy the values labeled 'high E spectrum' are valid.

		Sig	BG	Sig/$\sqrt{\text{BG}}$
this analysis				
1	trigger	1	-	
2	on-line filter	$\approx 10\%$	$\approx 2\,\text{Hz}$	0.07
3	low energy data set	$\approx 8\%$	$\approx 0.7\,\text{Hz}$	0.1
4	high energy data set	$\approx 1\%$	$\approx 6 \cdot 10^{-4}\,\text{Hz}$	0.4
IC86 DeepCore Filter and SMT3				
5	trigger	10	-	
6	velocity veto (low E spectrum)	$\sim 40\%$	$\sim 7\,\text{Hz}$	~ 1.5
7	ν-selection (low E spectrum)	$\sim 10\%$	$\sim 0.01\,\text{Hz}$	~ 11
8	velocity veto (high E spectrum)	$\sim 10\%$	$\sim 7\,\text{Hz}$	~ 0.5
9	ν-selection (high E spectrum)	$\sim 1\%$	$\sim 0.01\,\text{Hz}$	~ 1
IC86 Galactic Center Filter and SMT8				
10	trigger	10	-	
11	GC on-line filer	$\sim 50\%$	$\sim 4\,\text{Hz}$	~ 2.5

data set of a factor about four is expected. This results in an improvement of a about factor of 30 for the GC on-line filter combined with a ν-selection.
Accordingly, IC86 is expected to improve the sensitivity of this analysis for Dark Matter annihilations or decays by more than two orders of magnitude. For point-like sources a similar improvement is expected. For energy spectra with cut-off energies below 10 TeV this improvement is based on the DeepCore filter and for energy spectra with higher energies it is based on the Galactic Center filter.

10 Summary and Conclusions

The field of astroparticle physics contributes to today's understanding of particle physics and astronomy. Observations of cosmic rays and γ-rays are the main contributors to today's knowledge. However, the sources of the cosmic rays remain unknown. The origin of the cosmic rays is usually explained by sources accelerating charged particles (bottom-up models) or by the decay or annihilation of heavy particles (top-down models). Both scenarios can be tested with neutrinos.

For the acceleration scenario the most promising mechanism is Fermi-acceleration of charged particles. If these charged particles are hadrons, neutrinos are produced as secondaries. If instead leptons are accelerated, no neutrinos are expected. Measuring neutrinos would therefore give a clear indication of the type of the accelerated particles. Various sources in the universe are expected to accelerate these particles. At the highest energies these sources are expected to be extragalactic. At (neutrino) energies in the TeV range the sources can also be galactic objects. One group of candidates are known γ-ray sources. Three candidates are observed by γ-rays within less than 2° from the direction of the Galactic Center.

In the decay or annihilation scenario heavy relic particles are the origin of the cosmic radiation and neutrinos. In the universe many evidences for Dark Matter are found. Up to now, the properties of the Dark Matter particles are almost unknown. No particle of the Standard Model of particle physics fulfills all requirements. Candidates are predicted by many extensions of the Standard Model. Rotation curves of galaxies predict an accumulation of Dark Matter in the Galactic halo. The Dark Matter density peaks at the Galactic Center and decreases towards the outer regions. A flux of neutrinos is produced by annihilations or decays of the Dark Matter particles. This flux depends on the halo model and the decay or annihilation products. The Dark Matter particle mass is expected below 10 TeV.

The IceCube telescope located at the geographic South Pole is designed to detect neutrinos. It instruments a volume of $1\,\mathrm{km}^3$ with photomultiplier tubes to detect Cherenkov light. This light is produced by leptons created in charged current interactions of neutrinos. Each lepton flavor produces a unique signature in the detector. Muons create a long path and are reconstructed with an angular resolution at the order of 1°. For this analysis the IceCube detector with 40 strings is used. The measured events date from between April 2008 and May 2009. In the future the DeepCore enhancement with its denser instrumentation can be used to increase the sensitivity for events below 10 TeV.

Usually, in IceCube analyses the Earth is used as shield against the background of atmospheric muon events. This restricts the field of view to the Northern hemisphere. At high energies (PeV scale) the background fades away and an observation of the Southern sky is possible, too. At lower energies neutrino induced events from the Southern sky can be identified if the interaction vertex is demonstrably within the detector volume. For the reconstruction and identification of the interaction vertex new algorithms are developed in this thesis.

The reconstruction algorithm is based on the hit pattern to determine the interaction vertex of the neutrino. It projects the position of a DOM with a recorded pulse onto a previously reconstructed muon track. The most up-stream position is used as reconstructed position of the interaction vertex. Its precision depends on the accuracy of the

reconstructed track. In addition, the so-called P_{hit}-P_{noHit} likelihood function is implemented. It is based on the probability for a pulse in a certain DOM from a given track. Using this likelihood function a possible interaction vertex and stop point of the muon track in the detector are determined. Additionally, the ratio of the P_{hit}-P_{noHit} likelihood values assuming a track with and without the interaction vertex within the detector can be used to distinguish between these types of muon tracks.

These algorithms are used for a search for neutrinos from the direction of the Galactic Center ($\approx -29°$ declination). The analysis uses an on-source and an off-source region. The amount of events recorded in the on-source region located around the Galactic Center is compared to the background expectation derived from the off-source region. This procedure decouples a possible excess of neutrinos from the simulations and the uncertainties therein. Only the conversion into the signal flux depend on the simulation procedure.

The simulations are done in a collaboration wide effort using a modularized software framework. Events produced by neutrinos and cosmic rays are generated separately. Afterwards the same algorithms are used to propagate the muons through the ice and to simulate the Cherenkov photons and the detector response. This procedure allows to cross check the neutrino simulation by a comparison of the background simulation to the measured background data. The background passing rate of the selections used in this analysis differs by about 5% between the measured and simulated background data. The simulation is reliable, but this systematic uncertainty has to be included.

The measured events underwent a cleaning procedure and the event building. Afterwards, events for this analysis are selected by the Starting-Downgoing-Filter. This filter keeps events from the declination range of the Galactic Center which have no hits in the upper most 30 layers of DOMs. The events passing the filter are transferred to the North via satellite. The properties of the muons are reconstructed and many other characteristic quantities are determined. This is done in an unified approach together with events for other analyses. The reconstruction is done in a multi step procedure: first initial algorithms are applied, afterwards different likelihood fits are used. In addition to this general processing, the position of a possible interaction vertex and parameters indicating, whether the vertex is in the detector or not, are determined by the algorithms described above.

The recorded data is filtered in two steps. In the first step quality selections are applied to ensure a good directional reconstruction. The selections are rather loose and remove only a small amount of signal events. An angular resolution of about 2.6° is achieved. The following filtering step reduces the amount of background events (high energy data set). It selects higher energetic events which are likely to have a interaction vertex inside the detector. With this selection about 6 background events are expected in the on-source region. These events mimic events with an interaction vertex inside the detector. They are indistinguishable from neutrino events.

This separation is possible only for high energy events. At energies below about 10 TeV the muons produce only a small amount of light. Due to the HLC cleaning and the Dust Layer in the ice the few pulses caused by these muons are easily lost. This effect is enhanced for the observation direction toward the Galactic Center. Thus, more low energy cosmic ray muon induced events can pass the outer layers of IceCube undetected, and cause a neutrino like event. The sensitivity for low energy neutrinos cannot be improved by enforced selections. In addition to the high energy data set, the data set without

the second filtering step is used (low energy data set). In this case more than $70 \cdot 10^3$ background events are expected in the on-source region.
The size of the signal region is optimized separately for a neutrino flux from a point-like source or annihilating Dark Matter in the direction of the Galactic Center to achieve the best sensitivity. From the high energy and low energy data set always the more sensitive one is used. For point-like sources a signal region with an half opening angle of $\Delta\delta = 2.5°$ is used with the low energy data set for sources which produce only neutrinos below $\sim 10\,\mathrm{TeV}$ and the high energy data set above. For the annihilation of Dark Matter always the low energy data set is used with an half opening angle of $\Delta\delta = 8°$.
In all three combinations of signal region size and data set no excess of neutrinos is measured in the direction of the Galactic Center. Correspondingly, an upper limit on the number of possible signal events is determined.
In the signal region of the high energy data set six events remain, as expected from background. These events show all characteristics which an event induced by a neutrino should have. Some of these have an increased number of hits close to the first hit. Thus, they are indistinguishable from neutrino events. The identification of events with a potential interaction vertex in the detector volume is successful.
The derived limits on the number of neutrinos are converted into limits on the flux from a point-like source. The limits set on a flux from a point-like source at the position of the Galactic Center depend on the power law index γ and the energy cut-off E_{cut}. For comparisons with other analyses the limit (90% C.L.) set for $dN/dE \propto E^{\gamma} \cdot exp(-E/E_{\mathrm{cut}})$ with $\gamma = 2$ and $E_{\mathrm{cut}} = 100\,\mathrm{TeV}$ is a reasonable indicator:

$$E^2 \frac{dN}{dE dA dt} < 3 \cdot 10^{-9} \frac{\mathrm{TeV}}{\mathrm{cm^2 s}} \,. \tag{63}$$

This is about a factor three above the currently best limit set for $dN/dE \propto E^{-2}$ by ANTARES. However, the lower energy threshold for this analysis is below the threshold of the ANTARES result. Energy spectra with cut-off energies between 100 GeV and 10 TeV are not constrained by the ANTARES result. In this energy range the best limit is set by MACRO. It is still a factor of two stronger than the limit obtained in this work.
The derived limits on the Dark Matter self annihilation cross section or the Dark Matter life time depend on the assumed particle mass and the decay or annihilation channel. The limits for the annihilation cross section are between $10^{-23}\,\mathrm{cm^3 s^{-1}}$ and $10^{-21}\,\mathrm{cm^3 s^{-1}}$. This is in the physically allowed region but well above the natural scale expected from cosmology. Compared to the previously most restrictive limits by neutrino measurements (Super-Kamiokande), an improvement is achieved. In case of unstable Dark Matter the life time is limited to be larger than $10^{23}\,\mathrm{s}$ to $10^{25}\,\mathrm{s}$ depending on mass and decay products. These limits are similar to the limits obtained by Super-Kamiokande.
The regions in the parameter space excluded by this analysis are all already excluded by observations of photons by Fermi or HESS but these comparisons hold only for certain assumptions on the production and the properties at the source.
The search for neutrinos from the Galactic Center region will be improved by the now almost completed IceCube and DeepCore detector. The sensitivity is expected to increase more than two orders of magnitude due to additional instrumentation and new reconstruction techniques.

Acknowledgment

This thesis would not have been possible without the support of many people. I am grateful for this support.

Especially, I would like to express my gratitude to Prof. Dr. Christopher Wiebusch. He inspired me and gave me the opportunity to research in his group. Additionally, he always was a source of knowledge, new ideas and alternative approaches.

I would like to thank Prof. Dr. Marek Kowalski, who agreed to review this thesis as second referee.

I am indebted to Paolo Desiati and David Boersma. They did a fantastic job giving me a good start in the IceCube collaboration and answered all the questions a beginner might have. The work I began with you in Madison is the base of my later work and this analysis.

I am thankful for the support of Carsten Rott. Together, we introduced the search for Dark Matter from the Galactic Halo to the IceCube Collaboration and did the first analysis. Thanks for the successful time in Columbus.

I am grateful for the numerous discussions about this analysis and other topics with my colleagues of the IceCube group in Aachen. These discussions were inspiring and helpful. Special credits go to Sebastian Euler who shared the office with me. Three year I could rely on your knowledge, support and friendship. Also thanks to Christian Vogt, Jan Kovermann and Henrike Wissing, my first colleagues in Aachen.

Gratitude also goes to all my colleagues of the IceCube collaboration. In particular, I thank the WIMP and the point-source working group and Allan Hallgren, Chang Hyon Ha, Anna Franckowiak and Kael Hanson for their critical review and comments on my analysis.

The coffee breaks were a time for discussions with my colleagues from the institute. Not all of the discussions were focused on scientific or technical topics, but they gave new insights and ideas. I am grateful to all people who shared the numerous coffee breaks with me. Here, also a special thanks to people of the IT support.

I would also like to thank the RWTH Aachen for supporting my thesis with a grant.

Last but not least, I am deeply grateful to my friends and family. In particular, the 'Doppelkopf Runde' and 'Die Kletterer' always managed to drag me out of my office in the evening. I am thankful for the unbreakable support of Verena and my parents. They had to go through all ups and downs which occur during three years of research with me.

A HLC correction

The HLC cleaning procedure, which is described in section 3.2.5, is applied to each measured event. During this procedure isolated hits are removed from the data stream. Here, a hit with no hit in a neighboring DOM is called isolated. This affects the probability for observing a hit in a DOM and is taken into account for the calculation of the P_{hit}-P_{noHit}-likelihood. Therefore, the hit probability after this cleaning procedure can not be calculated locally for a single DOM, but also depends on the hit probability of the neighboring DOMs.
These correlations are taken into account in the calculation of the probability P_{string} for the hit pattern on a complete string. This probability is then used for the likelihood calculation instead of the probabilities of all individual DOMs:

$$L = \prod_{s} P_{\text{string}}(s) \; . \tag{64}$$

Here, the product includes all available strings (the index s is omitted in the following notations).
In a single event a DOM may have a hit, or not, after the cleaning procedure. Table 14 (line 1 and 2) shows as an example a section of a string with hits after the HLC cleaning. The DOMs with a hit and their direct neighbors have passed the cleaning procedure without changes (marked in line 3 of table 14). For the remaining DOMs the cleaning procedure may have removed a hit.
For the DOMs with unchanged hits no additional calculation is necessary. The probability for these DOMs to observe a physics or noise hit after the cleaning procedure is identical to the probability before the procedure. The determination of these probabilities is described in section 5.3 and an example is shown in figure 22. The probability for a hit is denoted P_{H} and the probability to have no hit is $P_{\text{nH}} = 1 - P_{\text{H}}$. The DOMs using these probabilities are marked in table 14 in row 4 and 5.
For DOMs with possibly removed hits the probability is calculated for groups of DOMs. Each group consists of all neighboring DOMs with possible changes. This probability is denoted P_{N}. N is the number of included DOMs. In Table 14 these DOMs are marked in line 6.

Table 14: Example section of a string to illustrate the calculation of the probability for a hit pattern on the string. The first line holds the DOM number, the second line indicates whether it has at least one hit (1) or not (0) after the cleaning procedure. In the third line all DOMs where it is known that no hits have been removed in the cleaning are marked (x). The used probability for these is indicated in line four and five. The last line indicates the DOMs with possibly removed hits.

DOM	1	2	3	4	5	6	7	8	9	10	11	12	13	14	15	16	17	18	19	20	21	+
hit	0	1	1	1	0	0	0	0	1	1	0	0	1	1	0	0	0	1	1	0	0	...
HLC	x	x	x	x	x	.	.	x	x	x	x	x	x	x	x	.	x	x	x	x	.	...
P_{H}	.	x	x	x	.	.	.	.	x	x	.	.	x	x	.	.	.	x	x	.	.	...
P_{nH}	x	.	.	.	x	.	.	x	.	.	x	x	.	.	x	.	x	.	.	x	.	...
P_{N}	.	.	.	.	.	x		.	.	.	.	.	.	.	.	x	.	.	.	.	x	...

The probability P_{string} for a pattern of hits on a string (required for equation 64) is the product of the individual probabilities (P_{H}, P_{nH} and P_{N})

$$P_{\text{string}} = \left(\prod_{i \in H} P_{\text{H}}(i)\right) \cdot \left(\prod_{i \in nH} P_{\text{nH}}(i)\right) \cdot \left(\prod_{i \in C} P_{\text{N}}(i)\right) \ . \tag{65}$$

H are the DOMs with hits, nH the DOMs next to DOMs with hits and thus no cleaned hits. C includes the groups of DOMs with possibly cleaned hits. P_{N} is determined by an iterative method. One by one the probabilities for hits in the individual DOMs are included. P_{N} is divided in two parts depending on the last included DOM:

- $p_0(n)$: the probability for **no** cleaned hit in DOM n (the last included DOM) multiplied with the probability for all DOMs before
- $p_1(n)$: the probability that a hit has been cleaned in the last DOM (n) multiplied with the probability for all DOMs before

Thus, $P_n = p_0(n) + p_1(n)$. Iteratively adding DOM $n+1$ to $p_0(n)$ and $p_1(n)$ results in

$$\begin{aligned} p_0(n+1) &= p_0(n) \cdot P_{\text{nH}}(n+1) + p_1(n) \cdot P_{\text{nH}}(n+1) \ , \\ p_1(n+1) &= p_0(n) \cdot P_{\text{H}}(n+1) \ . \end{aligned} \tag{66}$$

Here, it is taken into account that two neighboring DOMs cannot both have hits removed. The start values for this recursion are $p_0(0) = 1$ and $p_1(0) = 0$. The recursion is repeated until $p_0(N)$ and $p_1(N)$ are determined and $P_{\text{N}}(i) = p_0(N) + p_1(N)$ is inserted in equation 65.
With these equations the probability for a hit pattern on a string is described by the probabilities for a hit in a certain DOM before the HLC cleaning is applied. The probability for this hit pattern is used in the P_{hit}-P_{noHit} likelihood to correct for the cleaning.

B Angular Reconstruction

The presented analysis uses the direction reconstructed by the SPE Fit 32 Iterations (section 6.3.1). In chapter 5 other likelihood functions for the reconstruction of the direction are discussed. In the following, the performance of the discussed algorithms is compared:

1. the SPE-32 Fit (section 6.3.1),
2. the MPE Fit (section 5.2.2),
3. the combination of the P_{hit}-P_{noHit} likelihood (section 5.3) with the SPE likelihood (section 5.2.1),
4. the combination of the P_{hit}-P_{noHit} likelihood (section 5.3) with the MPE likelihood (section 5.2.2).

The first two methods are used as it is described in section 6.3.1. The likelihood algorithms using the P_{hit}-P_{noHit} likelihood are seeded with the reconstructed values of the SPE-32 Fit. Additionally, the start position determined by the StartStopPoint reconstruction (section 5.1.2) is used as seed for the interaction vertex which is required by the P_{hit}-P_{noHit} likelihood. All reconstructions have six free parameters: the direction (2 parameters), the position (3 parameters) and the event time.
The test is performed with simulated neutrinos of the high energy data set (section 6.4). The criterion for a good reconstruction is the angular difference between the reconstructed direction and the direction generated in the simulation.
Figure 65 shows the angular difference between the reconstructed direction and the simulated direction for three different energy spectra and all four likelihood reconstructions. Independent of the energy spectrum and the likelihood all distributions are similar. They have a peak at zero or nearby and a medium angular resolution of better than 3°. Only for the energy spectrum without energy cut-off larger differences are observed between the MPE and SPE likelihood. This analysis aims at energy spectra with cut-off and thus the choice of the reconstruction method has no major impact on the result.
In the following subsections the performance of the P_{hit}-P_{noHit} likelihood and the comparison between the MPE and SPE likelihood are discussed in more detail.

B.1 Comparison of MPE and SPE likelihood

The performance of the MPE and SPE likelihood function depends on the energy (figure 65). With the energy cut-off at 10 TeV both likelihood fits result in a similar distribution of the angular differences. Both distributions of the angular reconstruction error peak between 1° and 2°.
The average angular resolutions of the MPE and SPE algorithms improve when no energy cut-off is used. For the MPE likelihood the peak shifts to an reconstruction error of less than 1°. For the SPE likelihood the peak remains between 1° and 2°. At the cut-off energy of 100 TeV an intermediate precision is observed.
The different energy dependence of the two likelihood fits is caused by the dependence of the MPE fit on all hits in a DOM. At lower energies only few DOMs are expected to record more than one hit from a single muon. Here, the MPE likelihood fit cannot

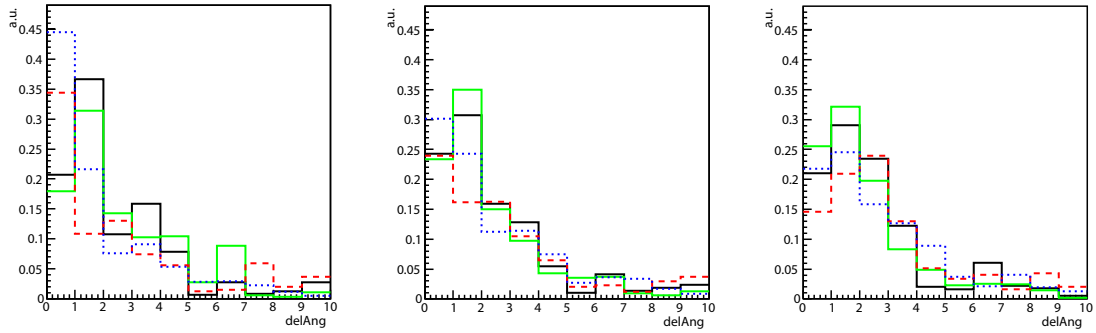

Figure 65: Angular difference between the reconstructed direction and the simulated direction of the neutrino for different likelihood functions and energy spectra. The figures use a $d\Phi/dE \propto E^{-2} \cdot exp(-E/E_{\mathrm{cut}}$ energy spectrum without cut-off ($E_{\mathrm{cut}} = \mathrm{inf}$), with $E_{\mathrm{cut}} = 100\,\mathrm{TeV}$ and with $E_{\mathrm{cut}} = 10\,\mathrm{TeV}$ (from left to right). The black (solid) line uses the SPE Fit 32 Iterations, the green (solid) line uses the $\mathrm{P_{hit}}$-$\mathrm{P_{noHit}}$ likelihood in combination with the SPE likelihood assuming a starting track, the red (dashed) line uses the $\mathrm{P_{hit}}$-$\mathrm{P_{noHit}}$ likelihood in combination with the MPE likelihood assuming a starting track, and the blue (dotted) line uses the MPE Fit.

achieve an improvement compared to the SPE likelihood fit. Noise hits can degrade the reconstruction precision. At the highest energies more late hits are caused by the muon and the noise is no dominant contribution. Here, the reconstruction profits from the late hits.

B.2 Performance of the $\mathbf{P_{hit}}$-$\mathbf{P_{noHit}}$ likelihood

In addition the precision of the angular reconstruction of newly developed $\mathrm{P_{hit}}$-$\mathrm{P_{noHit}}$ likelihood fit is tested. Using only this likelihood function results in relatively poor angular reconstruction: the angular resolutions is several degree worse than for the SPE or MPE likelihood fit. The time information used by the SPE and MPE fit is more accurate than the spatial resolution: compare the time resolution $ct \approx 0.5\,\mathrm{m}$ to the distance between DOMs or strings 17 m or 125 m, respectively.

Instead of using the $\mathrm{P_{hit}}$-$\mathrm{P_{noHit}}$ likelihood fit as a stand-alone method, it is used to improve the results of the SPE or MPE likelihood reconstruction in a fit with a combined likelihood. Combining the $\mathrm{P_{hit}}$-$\mathrm{P_{noHit}}$ likelihood, a hit pattern sensitive factor, with the time dependent likelihood can improve the angular resolution and enables the sensitivity to the possible interaction vertex or stop point. Including new information into the fit also can foster new mis-interpretations or mis-reconstructions.

Figure 65 shows a similar distribution of the angular difference for the fits with the $\mathrm{P_{hit}}$-$\mathrm{P_{noHit}}$ likelihood and the corresponding fits without the $\mathrm{P_{hit}}$-$\mathrm{P_{noHit}}$ likelihood. This confirms the expectation that the angular reconstruction is dominated by the timing information. For the energy spectra with a cut-off energy the combination of the SPE likelihood and $\mathrm{P_{hit}}$-$\mathrm{P_{noHit}}$ likelihood results in an improved reconstruction precision. For the energy spectrum without energy cut-off the angular resolution is worse than using only the SPE fit. This degradation is caused by the neglected energy dependence of the hit probability in the used $\mathrm{P_{hit}}$-$\mathrm{P_{noHit}}$ implementation.

The angular reconstruction of the MPE likelihood is on average better than for the combination of the MPE likelihood and the P_{hit}-P_{noHit} likelihood (independent on the energy spectrum). This can be explained by correlations between the MPE likelihood and the P_{hit}-P_{noHit} likelihood. The number of hits in a DOM is correlated with the probability to observe a hit in this DOM. Thus, the combination of the likelihood functions assigns a too large weight to the spatial distribution of the hits.
The applied tests show that the combination of the P_{hit}-P_{noHit} likelihood with the SPE likelihood can improve the angular reconstruction by about 0.3° for low energetic events. For high energetic events an update of the algorithm is required.
The combination of the P_{hit}-P_{noHit} likelihood and the SPE likelihood is not used in this analysis even though it has a slightly better angular resolution. The main reason is the computation time. The P_{hit}-P_{noHit} likelihood uses the information of all DOMs (about 2400) while the SPE likelihood uses only the DOMs with a hit (at the order of 20). This increase of about two orders of magnitude in the number of DOMs results in a factor of about 10 in the computation time. Thus it is not possible to run the combined fit on millions of events as it would be necessary for the low energy data set.
Additionally the SPE likelihood fit is tested better than the combination with the P_{hit}-P_{noHit} likelihood. It is used for several IC40 and IC20 analyses and many cross checks are performed.

References

[A+87a] E. Alexeyev et al., *Possible detection of a Neutrino Signal on 23 February 1987 at the Baksan Underground Scintillation Telescope of the Institute of Nuclear Research*, **45**, 589 (1987).

[A+87b] E. Alexeyev et al., *Status of the Baksan Experiment on the Search for Neutrino Bursts from Stellar Collapses*, Proceedings of the 20th International Cosmic Ray Conference, Moscow **6**, 277 (1987).

[A+07] A. Abdo et al., *TeV Gamma-Ray Sources from a Survey of the Galactic Plane with Milagro*, Astrophys. J. Lett. **664**, 91–94 (2007).

[A+09] O. Adriani et al., *Observation of an anomalous positron abundance in the cosmic radiation*, Phys. Rev. Lett. **102**(051101) (2009).

[ACD01] T. Appelquist, H.-C. Cheng and B. Dobrescu, *Bounds on Universal Extra Dimensions*, Phys. Rev. **D 64**(035002) (2001).

[AMA91] AMANDA Collaboration, *Observation of Muons Using the Polar Ice Cap as a Cerenkov Detector*, Nature **353**, 331–333 (1991).

[AMA04] AMANDA Collaboration, *Muon Track Reconstruction and Data Selection Techniques in AMANDA*, Nucl. Instrum. Methods **A 524**, 169–194 (2004).

[AMS07] AMS-01 Collaboration, *Cosmic-Ray Positron Fraction Measurement from 1GeV to 30GeV with AMS-01*, Phys. Lett. **B 646**, 145 (2007), astro-ph/0703154.

[And33] C. Anderson, *Cosmic-Ray Positive and Negative Electrons*, Phys. Rev. **44**, 406–416 (1933).

[ANT99] ANTARES Collaboration, *A Deep Sea Telescope for High Energy Neutrinos*, CPPM-P-1999-02, DAPNIA 99-01, IFIC/99-42, SHEF-HEP/99-06 (1999), arXiv:astro-ph/9907432.

[B+88] C. Bratton et al., *Angular Distribution of Events from SN1987A*, Phys. Rev. **D 37**, 3361 (1988).

[B+06] M. Boliev et al., *Results with the Baksan Neutrino Telescope*, Workshop on Exotic Particles with Neutrino Telescopes, Uppsala (2006).

[B+09] V. Barger et al., *Dark Matter and Pulsar Signals for Fermi LAT, PAMELA, ATIC, HESS and WMAP Data*, arXiv:0904.2001 (2009).

[Bai90] Baikal Collaboration, *The BAIKAL Experiment*, Nucl. Phys. **B 14**, 51–60 (1990).

[BEO00] P. Blasi, R. Epstein and A. Olinto, *Ultra-High-Energy Cosmic Rays from Young Neutron Star Winds*, Astro. J. **533**, 123–126 (2000).

[Ber98] E. Bertschinger, *Simulations of Structure Formation in the Universe*, Astro. & Astrophys. **36**, 599–654 (1998).

[BH09] J. Braun and D. Hubert for the IceCube Collaboration, *Searches for WIMP Dark Matter from the Sun with AMANDA*, Proceedings of the 31st ICRC, Lodz, Poland (2009).

[Bor09] Borexino Collaboration, *The Borexino Detector at the Laboratori Nazionali del Gran Sasso*, Nucl. Instrum. Methods **A 600**, 568–593 (2009).

[BP86] S. Bhattacharyya and P. Pal, *Simple Leaky Box Model for Cosmic-Ray Propagation, Models for Production of Antiprotons at Ultrahigh Energies and the Estimations of the Ratios*, Nuovo Cimento C **9**(5), 961–983 (1986).

[BP88] V. Berezinsky and V. Ptuskin, *Radiation Generated in Young type II Supnerova envelopes by Shock-Accelerated Cosmic Rays*, Sov. Astron. Lett. **14**(4), 304–308 (1988).

[BP89] V. Berezinsky and V. Ptuskin, *Radiation from Young SN II Shells Produced by Cosmic Rays Accelerated in Shock Waves*, Astro. & Astrophys. **215**(2), 399–408 (1989).

[BS01] F. Bosch and R. Swaters, *Dwarf Galaxy Rotation Curves and the Core Problem of Dark Matter Halos*, Mon. Not. Roy. Astron. Soc. **325**, 1017 (2001), arXiv:astro-ph/0006048v2.

[Buc09] W. Buchmuller, *Gravitino Dark Matter*, DESY **09-181** (2009), arXiv:0910.1870v2 [hep-ph].

[BV00] V. Berezinsky and A. Vilenkin, *Ultra High Energy Neutrinos from Hidden-Sector Topological Defects*, Phys. Rev. **D 62**(083512) (2000), arXiv:hep-ph/9908257v1.

[C$^+$98] B. Cleveland et al., *Measurement of the Solar Electron Neutrino Flux with the Homestake Chlorine Detector*, Astro. J. **496**, 505–526 (1998).

[C$^+$08] J. Chang et al., *An Excess of Cosmic Ray Electrons at Energies of 300-800 GeV*, Nature **456**, 362 (2008).

[CDM04] CDMS Collaboration, *Installation and Commissioning of the CDMS II Experiment at Soudan*, Nucl. Instrum. Methods **A 520**, 116 (2004).

[CDM09] CDMS Collaboration, *Results from the Final Exposure of the CDMS II Experiment*, arXiv:0912.3592v1 [astro-ph.CO] (2009).

[CGS97] J. Cronin, T. Gaisser and S. Swordy, *Cosmic Rays at the Energy Frontier*, Sci. Amer. **276**, 44 (1997).

[CGZ09] C.-H. Chen, C.-Q. Geng and D. Zhuridov, *Resolving Fermi, PAMELA and ATIC Anomalies in Split Supersymmetry without R-Parity*, arXiv:0905.0652 (2009).

[Cha06] S. Chaty, *The Role of Microquasars in Astroparticle Physics*, (2006).

[Cha09] R. Chaves for the HESS Collaboration, *Extending the H.E.S.S. Galactic Plane Survey*, Proceedings of the 31st ICRC, Lodz (2009).

[Chi04] D. Chirkin, *Fluxes of Atmospheric Leptons at 600 GeV - 60 TeV*, arXiv:hep-ph/0407078v1 (2004).

[CIP09] M. Cirelli, F. Iocco and P. Panci, *Constraints on Dark Matter Annihilations from Reionization and Heating of the Intergalactic Gas*, J. Cos. and Astropart. Phys. **0910**, 009 (2009).

[CM09] X. Calmet and S. Majee, *Effective Theory for Dark Matter and a new Force in the Dark Matter*, arXiv:0905.0956 (2009).

[CR04] D. Chirkin and W. Rhode, *Propagating Leptons though Matter with Muon Monte Carlo (MMC)*, arXiv:hep-ph/0407075v (2004).

[D+04] C. Dickinson et al., *High Sensitivity Measurements of the CMB Power Spectrum with the Extended Very Small Array*, Mon. Not. Roy. Astron. Soc. **353**, 732 (2004), arXiv:astro-ph/0402498v2.

[D+08] J. Dunkley et al., *Five-Year Wilkinson Microwave Anisotropy Probe (WMAP), Observations: Likelihoods and Parameters from the WMAP data*, arXiv:0803.0586v2 (2008).

[Dar05] A. Dar, *The Origin of Cosmic Rays 92-year-old Puzzle solved?*, Nuovo Cimento B **120**, 767 (2005).

[DD09] S. Dado and A. Dar, *Dark Matter Signals in Cosmic Rays?*, arXiv:0903.0165 (2009).

[Duf94] M. Duff, *Kaluza-Klein Theory in Perspective*, Talk delivered at the Oskar Klein Centenary Nobel Symposium, Stockholm (1994), arXiv:hep-th/9410046v1.

[Dum09] J. Dumm for the IceCube Collaboration, *All-Sky Point-Source Search with 40 Strings of IceCube*, Proceedings of the 31th International Cosmic Ray Conference, Lodz (2009).

[Ein36] A. Einstein, *Lens-Like Action of a Star by the Deviation of Light in the Gravitational Field*, Science **84**(2188), 506–507 (1936).

[Ein65] J. Einasto, *Influence of the Atmospheric and Instrumental Dispersion on the Brightness Distribution in a Galaxy*, Trudy Inst. Astrofiz. Alma-Ata **5**(87) (1965).

[ESS09] R. Essig, N. Sehgal and L. Strigari, *Bounds on Cross-Sections and Lifetimes for Dark Matter Annihilation and Decay into Charged Leptons from Gamma-Ray Observations of Dwarf Galaxies*, Phys. Rev. **D 80**(023506) (2009), arXiv:0902.4750v2 [hep-ph].

[Eul] S. Euler, Measurements of Neutrino Oscillations with IceCube, Phd Thesis, in preperation.

[Eul08] S. Euler, *On the Detection of Low Energy Neutrino Events with Full-Sky Acceptance with the IceCube DeepCore Detector*, Rheinisch-Westfälische Technische Hochschule (RWTH) Aachen (2008), Diploma Thesis.

[F+09] Y. Fujita et al., *Is the PAMELA Anomaly caused by the Supernova Explosions near the Earth?*, arXiv:0903.5298 (2009).

[FBS89] M. Fich, L. Blitz and A. Stark, *The Rotation Curve of the Milki Way to* $2R_0$, Astrophys. J. **342**, 272 (1989).

[FC98] G. Feldman and R. Cousin, *Unified Approach to the Classical Statistical Analysis of Small Signals*, Phys. Rev. **D 57**(7) (1998).

[Fer49] E. Fermi, *On the Origin of the Cosmic Radiation*, Phys. Rev. **75**, 1169 (1949).

[Fer09a] Fermi Collaboration, *Photon Data*, http://fermi.gsfc.nasa.gov/cgi-bin/ssc/LAT/WeeklyFiles.cgi (2009).

[Fer09b] Fermi LAT Collaboration, *Measurement of the Cosmic Ray* $e^+ + e^-$ *Spectrum from 20GeV to 1TeV with the Fermi Large Area Telescope*, Phys. Rev. Lett. **102**(181101) (2009), arXiv:0905.0025.

[FKS09] H. Fukuokaand, J. Kubo and D. Suematsu, *Anomaly Induced Dark Matter Decay and PAMELA/ATIC Experiments*, arXiv:0905.2847 (2009).

[Fra07] R. Franke for the IceCube Collaboration, *Point Source Analysis for Cosmic Neutrinos Beyond PeV Energies with AMANDA and IceCube*, Proceedings of the 30th International Cosmic Ray Conference, Merida, Yucatan, Mexico (2007), also in arXiv:0711.0353 [astro-ph], 103-106.

[G+04] P. Gondolo et al., *DarkSUSY: Computing Supersymmetric Dark Matter Properties Numerically*, J. Cos. and Astropart. Phys. **0407**(008) (2004), arXiv:astro-ph/0406204v1.

[G+09] S. Gillessen et al., *Monitoring Stellar Orbits Around the Massive Black Hole in the Galactic Center*, Astrophys. J. **692**, 1075–1109 (2009).

[Gai90] T. Gaisser, *Cosmic Rays and Particle Physics*, Cambridge University Press, 1990.

[Gei] M. Geisler, Monte Carlo Study on the Measurement of Atmospheric Muon Neutrinos with the IceCube Neutrino Observatory, Diploma Thesis, in preperation.

[GK05] A. Gazisov and M. Kowalski, *ANIS: High Energy Neutrino Generator for Neutrino Telescopes*, Computer Phys. Comm. **172**, 203–213 (2005), arXiv:astro-ph/0406439v1.

[Glu] T. Glüsenkamp, On Monopole searches with IceCube including DeepCore, Diploma Thesis, in preperation.

[GO69] J. Gunn and J. Ostriker, *Acceleration of High-Energy Cosmic Rays by Pulsars*, Phys. Rev. Lett. **22**(14), 728–731 (1969).

[Gre66] K. Greisen, *End to the Cosmic-Ray Spectrum?*, Phys. Rev. Lett. **16**, 748–750 (1966).

[Gro06] A. Groß, *Search for High Energy Neutrinos from Generic AGN classes with AMANDA-II*, PhD thesis, Fachbereich Physik, Universitt Dortmund, 2006.

[H+88] K. Hirata et al., *Observation in the Kamiokande-II Detector of the Neutrino Burst from Supernova SN1987A*, Phys. Rev. **D 38**, 448 (1988).

[H+98] D. Heck et al., *CORSIKA: a Monte Carlo Code to Simulate Extensive Air Showers*, Forschungszentrum Karlsruhe GmbH, Karlsruhe (Germany) (1998).

[H+07] G. Hinshaw et al., *Three-Year Wilkinson Microwave Anisotropy Probe (WMAP) Observations: Temperature Analysis*, Astro. J. **170**, 288 (2007), arXiv:astro-ph/0603451v2.

[H+08] G. Hinshaw et al., *Five-Year Wilkinson Microwave Anisotropy Probe (WMAP), Observations: Dataprocessing, Sky Maps and Basic results*, arXiv:0803.0732v2 (2008).

[H+09] H.-B. Hu et al., *On the $e^+ + e^-$ Excesses and the Knee of the Cosmic Ray Spectra - Hints of Cosmic Rays Acceleration at Young Supernova Remnants*, arXiv:0901.1520 (2009).

[HBS09] D. Hooper, P. Blasi and P. Serpico, *Pulsars as the Sources of High Energy Cosmic Ray Positrons*, J. Cos. and Astropart. Phys. **01**(025) (2009).

[HEA97] HEAT Collaboration, *Measurements of the Cosmic-Ray Positron Fraction from 1GeV to 50GeV*, Astrophys. J. **482**, 191 (1997), astro-ph/9703192.

[Hei44] W. Heitler, *Quantum Theory of Radiation*, Oxford University Press, 1944.

[Hes12] V. F. Hess, *Über Beobachtungen der durchdringenden Strahlung bei sieben Freiballonfahrten*, Physikalische Zeitschrift **21**, 22 (1912), 13. Jahrgang.

[HES05a] HESS Collaboration, *A new Population of Very Eigh Energy Gamma-Ray Sources in the Milky Way*, Science **307**, 1938–1942 (2005), arXiv:astro-ph/0504380v1.

[HES05b] HESS Collaboration, *Very High Energy Gamma Rays from the Composite SNR G0.9+0.1*, Astro. & Astrophys. **432**, 25–29 (2005).

[HES06a] HESS Collaboration, *Discovery of Very-High-Energy Gamma-Rays from the Galactic Centre Ridge*, Nature **439**, 695–698 (2006), arXiv:astro-ph/0603021v1.

[HES06b] HESS Collaboration, *HESS Observations of the Galactic Center Region and Their Possible Dark Matter Interpretation*, Phys. Rev. Lett. **97**(221102) (2006), Erratum ibid. 97 (2006) 249901.

[HES06c] HESS Collaboration, *The H.E.S.S. Survey of the Inner Galaxy in Very High-Energy Gamma-Rays*, Astrophys. J. **636**, 777–797 (2006), arXiv:astro-ph/0510397v1.

[HES08] HESS Collaboration, *Observations of the Sagittarius Dwarf Galaxy by the H.E.S.S. Experiment and Search for a Dark Matter Signal*, Astropart. Phys. **29**, 55–62 (2008).

[HES09a] HESS Collaboration, *Localising the VHE Gamma-Ray Source at the Galactic Centre*, arXiv:0911.1912v2 (2009).

[HES09b] HESS Collaboration, *Probing the ATIC Peak in the Cosmic-Ray Electron Spectrum with H.E.S.S*, arXiv:0905.0105 (2009).

[HES10] HESS Collaboration, *HESS J1745-303*, submitted, http://www.mpi-hd.mpg.de/hfm/HESS/pages/home/som/2008/01/ (2010).

[HNN09] K. Hamaguchiand, K. Nakaji and E. Nakamura, *Inverse Problem of Cosmic-Ray Electron/Positron from Dark Matter*, arXiv:0905.1574 (2009).

[HNY09] J. Hisano, K. Nakayama and M. Yang, *Upward Muon Signals at Neutrino Detectors as a Probe of Dark Matter Properties*, Phys. Lett. **B 678**, 101–106 (2009), arXiv:0905.2075v2 [hep-ph].

[HSZ08] D. Hooper, A. Stebbins and K. Zurek, *The PAMELA and ATIC Excesses from a Nearby Clump of Neutralino Dark Matter*, arXiv:0812.3202 (2008).

[Hue] J.-P. Hülß, finiteReco Project, http://code.icecube.wisc.edu/svn/projects/finiteReco/.

[Ice] IceCube Collaboration, Preliminary Design Document, http://www.icecube.wisc.edu/science/publications/pdd/.

[Ice06] IceCube Collaboration, *Optical Properties of Deep Glacial Ice at the South Pole*, J. Geophys. Res. **111**(D13203), 26 (2006).

[Ice07] IceCube Collaboration, *Multiyear Search for a Diffuse Flux of Muon Neutrinos with AMANDA-II*, Phys. Rev. **76**(042008) (2007), erratum ibid 77 (2008) 089904(E), arXiv:0705.1315 [astro-ph].

[Ice09a] IceCube Collaboration, *Determination of the Atmospheric Neutrino Flux and Searches for New Physics with AMANDA-II*, Phys. Rev. **D 79**(102005) (2009), arXiv:0902.0675 [astro-ph.HE].

[Ice09b] IceCube Collaboration, *Extending the Search for Neutrino Point Sources with IceCube above the Horizon*, Phys. Rev. Lett. **103**(221102) (2009), arXiv:0911.2338v2 [astro-ph.HE].

[Ice09c] IceCube Collaboration, *First Neutrino Point-Source Results from the 22 String IceCube Detector*, Astrophys. J. **701**, 47–51 (2009).

[Ice09d] IceCube Collaboration, *The IceCube Data Acquisition System: Signal Capture, Digitization, and Timestamping*, Nucl. Instrum. Methods Phys. Research **601**(3), 294–316 (2009).

[Ice09e] IceCube Collaboration, *Search for Point Sources of High Energy Neutrinos with Final Data from AMANDA-II*, Phys. Rev. **D 79**(062001) (2009), arXiv:0809.1646 [astro-ph].

[Ice09f] IceCube Collaboration, *Table of AMANDA Final Event Sample*, Phys. Rev. **D 79**(062001) (2009), http://www.icecube.wisc.edu/science/data/.

[Ice10a] IceCube Collaboration, Search for Dark Matter from the Galactic Halo with IceCube, to be published, 2010.

[Ice10b] IceCube Collaboration, The Design and Physics Capabilities of IceCube's DeepCore Subarray, to be published, 2010.

[Ien09] R. Iengo, *Sommerfeld Enhancement: general results from field theory diagrams*, **05**, 024 (2009).

[IMB87] IMB Collaboration, *An Upper Limit on the Flux of Extraterrestrial Neutrinos*, Astrophys. J. **315**, 420–424 (1987).

[IMB93] IMB Collaboration, *IMB-3: A Large Water Cerenkov Detector for Nucleon Decay and Neutrino Interactions*, Nucl. Instrum. Methods **A 324**, 363–382 (1993).

[IMY09] M. Ibe, H. Murayama and T. Yanagida, *Breit-Wigner Enhancement of Dark Matter Annihilation*, Phys. Rev. **D 79**(095009) (2009).

[Ino07] S. Inoue, *Astrophysical Origins of the Highest Energy Cosmic Rays*, astro-ph/0701835 (January 2007).

[J+06] W. Jones et al., *A Measurement of the Angular Power Spectrum of the CMB Temperature Anisotropy from the 2003 Flight of Boomerang*, Astro. J. **647**, 823–832 (2006), astro-ph/0507494.

[Jac96] J. Jackson, *Classical Electrodynamics*, New York, USA, 3rd edition, 1996.

[K+98] A. V. Kravtsov et al., *The Cores of Dark Matter-Dominated Galaxies: Theroy versus Observations*, Astrophys. J. **502**(48) (1998), arXiv:astro-ph/9708176.

[K+04] C. Kuo et al., *High Resolution Observations of the CMB Power Spectrum with ACBAR*, Astro. J. **600**, 32–51 (2004), arXiv:astro-ph/0212289.

[K+08] E. Komatsu et al., *Five-Year Wilkinson Microwave Anisotropy Probe (WMAP), Observations: Cosmological Interpretation*, arXiv:0803.0547v2 (2008).

[K+09] E. Komatsu et al., *Five-Year Wilkinson Microwave Anisotropy Probe (WMAP) Observations: Cosmological Interpretation*, Astrophys. J. Lett. **180**, 330–376 (2009), arXiv:0803.0547v2 [astro-ph].

[Kam98] M. Kamionkowski, *Possible Relics from New Physics in the Early Universe: Inflation, the Cosmic Microwave Background, and Particle Dark Matter*, arXiv:astro-ph/9809214v1 (1998).

[KHSA07] A. Kappes, J. Hinton, C. Stegmann and F. Aharonian, *Potential Neutrino Signals from Galactic γ-Ray Sources*, Astrophys. J. **656**, 870–878 (2007).

[KM308] KM3NeT Consortium, *KM3NeT: Conceptual Design of a Deep-Sea Research Infrastructure Incorporating a Very Large Neutrino Telescope in the Mediterranean Sea*, Conceptual Design Report (2008), http://www.km3net.org/CDR/CDR-KM3NeT.pdf.

[Kno09] S. Knops, *Online Selection of Downgoing Starting Low Energy Neutrino Events in IceCube*, Rheinisch-Westfälische Technische Hochschule (RWTH) Aachen (2009), Diploma Thesis.

[KS98] A. Kusenko and M. Shaposhnikov, *Supersymmetric Q-balls as Dark Matter*, Phys. Lett. **B 418**, 46–54 (1998), arXiv:hep-ph/9709492v3.

[KT90] E. Kolb and M. Turner, *The Early Universe*, Addison-Wesley, 1990.

[L$^+$81] J. Learned et al., *DUMAND - An Undersea Neutrino Telescope*, Astro. & Astrophys. **031.034.056** (1981).

[L$^+$07] J. Lundberg et al., *Light Tracking through Ice and Water - Scattering and Absorption in Heterogeneous Media with PHOTONICS*, Nucl. Instrum. Methods **A 581**(3), 619–631 (2007).

[Lid03] A. Liddle, *An Introduction to Modern Cosmology*, Wiley-VCH, second edition edition, 2003, ISBN 0-470-84834-0.

[LM00] J. Learned and K. Mannheim, *Hich-Energy Neutrino Astrophysics*, Annu. Rev. Nucl. Part. Sci. **50**, 679–749 (2000).

[Luc74] L. Lucy, *An Iterative Technique for the Rectification of Observed Distributions*, Astro. J. **70**(6), 745–754 (1974).

[LVD89] LVD Collaboration, *The Large-Volume Detector (LVD) : a Multipurpose Underground Detector at Gran Sasso*, Nucl. Instrum. Methods **A 277**, 11–16 (1989).

[LYZ09] J. Liuand, P. Yin and S. Zhu, *Prospects for Detecting Neutrino Signals from annihilating/decaying Dark Matter to account for the PAMELA and ATIC Results*, arXiv:0812.0964 (2009).

[M$^+$99] B. Moore et al., *Cold Collapse and the Core Catastrophe*, Mon. Not. Roy. Astron. Soc. **310**(1147) (1999), arXiv:astro-ph/9903164.

[M$^+$06] D. Merritt et al., *Empirical Models for Dark Matter Halos. I. Nonparametric Construction of Density Profiles and Comparison with Parametric Models*, arXiv:astro-ph/0509417 (2006).

[MAC99] MACRO Collaboration, *Limits on Dark Matter WIMPs using Upward Going Muons in the MACRO Detector*, Nucl. Instrum. Methods **A 60**(082002) (1999), hep-ex/9812020.

[MAC01] MACRO Collaboration, *Neutrino Astronomy with the MACRO Detector*, Astrophys. J. **546**, 1038–1054 (2001), astro-ph/0002492.

[MAC02] MACRO Collaboration, *The MACRO Detector at Gran Sasso*, Nucl. Instrum. Methods **A 486**, 663–707 (2002).

[MCG09] D. Malyshev, I. Cholis and J. Gelfand, *Pulsars versus Dark Matter Interpretation of ATIC/PAMELA*, arXiv:0903.1310 (2009).

[Mic84] F. Michel, *Cosmic-Ray Acceleration by Pulsars*, Adv. Space Res. **4**(2-3), 387–391 (1984).

[Mir02] I. Mirabel, *Microquasars as Sources of High Energy Phenomena*, (2002).

[Mon99] T. Montaruli for The MACRO Collaboration, *MACRO as a Telescope for Neutrino Astronomy*, 26th ICRC, HE.4.2.03 (1999), arXiv:hep-ex/9905020v1.

[MP09] P. Meade and M. Papucci, *Dark Matter Interpretations of the $e^{\pm}$ Excesses after FERMI*, IFUP-TH/2009-9 (2009), arXiv:0905.0480v1.

[MPF96] M.Persic, P.Salucci and F.Stel, *The Universal Rotation Curve of Spiral Galaxies: I. the Dark Matter Connection*, Mon. Not. Roy. Astron. Soc. **281**(27) (1996), arXiv:astro-ph/9506004v3.

[MS53] H. Motz and L. Schiff, *Cherenkov Radiation in a Dispersive Medium*, Am. J. Phys. **21**, 258–259 (1953).

[MS96] M. Morris and E. Serabyn, *The Galactic Center Enviroment*, Astro. & Astrophys. **34**, 645–701 (1996).

[NEM09] NEMO Collaboration, *Status of NEMO: Results from the NEMO Phase-1 Detector*, Phys. Rev. **B 190**, 109–114 (2009).

[NES05] NESTOR Collaboration, *Operation and Performance of the NESTOR Test Detector*, Nucl. Instrum. Methods **A 552**, 420–439 (2005).

[NFW96] J. Navarro, C. Frenk and S. White, *The Structure of Cold Dark Matter Halos*, Astrophys. J. **462**(563) (1996), arXiv:astro-ph/9508025.

[O$^+$89] Y. Oyama et al., *Experimental Study of Upward-Going Muons in Kamiokande*, Phys. Rev. **D 39**, 1481–1491 (1989).

[Ost02] M. Ostrowski, *Mechanisms and Sites of Ultra High Energy Cosmic Ray Origin*, Astropart. Phys. **18**, 229–236 (2002), astro-ph/0101053.

[OY09] N. Okada and T. Yamada, *The PAMELA and Fermi Signals from Long-Lived Kaluza-Klein Dark Matter*, arXiv:0905.2801 (2009).

[PAM09] PAMELA Collaboration, *An Anomalous Positron Abundance in Cosmic Rays with Energies 1.5-100 GeV*, Nature **458**, 607 (2009).

[Pan96] D. Pandel, *Bestimmung von Wasser- und Detektorparametern und Rekonstruktion von Myonen bis 100 TeV mit dem Baikal-Neutrinoteleskop NT-72*, Humboldt-University in Berlin (1996), Diploma Thesis.

[Par08] Particle Data Group, *Review of Particle Physics*, Phys. Lett. **B 667**, 1 (2008).

[Pie07] Pierre Auger Collaboration, *Correlation of the Highest-Energy Cosmic Rays with Nearby Extragalactic Objects*, Science **318**(5852), 938 (2007).

[Pie08] Pierre Auger Collaboration, *Observation of the Suppression of the Flux of Cosmic Rays above* $4 \cdot 10^{19}$ *eV*, arXiv:0806.4302v1 (2008).

[Por09] T. Porter for the Fermi LAT Collaboration, *Fermi LAT Measurements of the Diffuse Gamma-Ray Emission at Intermediate Galactic Latitudes*, arXiv:0907.0294v1 [astro-ph.HE] (2009).

[PPB08] PPB-BETS Collaboration, *High-Energy Electron Observations by PPB-BETS Flight in Antarctica*, arXiv:0809.0760 (2008).

[PQ77] R. Peccei and H. Quinn, *CP Conservation in the Presence of Pseudoparticles*, Phys. Rev. Lett. **38**, 1440–1443 (1977).

[Pro96] R. Protheroe, *Origin and Propagation of the Highest Rnergy Cosmic Rays*, ADP-AT-96-14 (1996), arXiv:astro-ph/9612212v1.

[Pro98] R. Protheroe, *Acceleration and Interaction of Ultra High Energy Cosmic Rays*, astro-ph/9812055 (1998).

[Pro08] S. Profumo, *Dissecting PAMELA (and ATIC) with Occam's Razor: Existing, well-known Pulsars naturally account for the 'anomalous' Cosmic-Ray Electron and Positron Data*, arXiv:0812.4457 (2008).

[PS09] M. Papucci and A. Strumia, *Robust Implications on Dark Matter from the first FERMI Sky Gamma Map*, arXiv:0912.0742v2 [hep-ph] (2009).

[PT08] K. Ptitsyna and S. Troitsky, *Physical Conditions in Potential Sources of Ultra-High-Energetic Cosmic Rays. I. Updated Hillas Plot and Radiation Loss Constrains*, arXiv:0808.036/v1 [astro-ph] (2008).

[PWC00] P. Price, K. Woschnagg and D. Chirkin, *Age vs. Depth of Glacial Ice at the Southe Pole*, Geophys. Res. Lett. **27**(13), 2129–2144 (2000).

[R$^+$04] A. Readhead et al., *Polarization Observations with the Cosmic Background Imager*, Science **306**, 836–844 (2004), arXiv:astro-ph/0409569v2.

[RB93] J. Rachen and P. Biermann, *Extragalactic Ultra-High Energy Cosmic-Rays - Part One - Contribution from Hot Spots in Fr-II Radio Galaxies*, Astro. & Astrophys. **272**, 161 (1993).

[RU09] M. Regis and P. Ullio, *Testing the Dark Matter Interpretation of the PAMELA Excess through Measurements of the Galactic Diffuse Emission*, arXiv:0904.4645 (2009).

[S+07] D. Spergel et al., *Wilkinson Microwave Anisotropy Probe (WMAP) Three Year Observations: Implications for Cosmology*, Astrophys. J. **170**, 377 (2007).

[S+09] S. Schönert et al., *Vetoing Atmospheric Neutrinos in a High Energy Neutrino Telescope*, Phys. Rev. **D 79**(043009) (2009), arXiv:0812.4308v1 [astro-ph].

[SFW06] V. Springel, C. Frenk and S. White, *The Large-Scale Structure of the Universe*, arXive:astro-ph/0604561v1 (2006).

[SNO00] SNO Collaboration, *The Sudbury Neutrino Observatory*, Nucl. Instrum. Methods **A 449**, 172–207 (2000).

[SNP09] N. Shaviv, E. Nakar and T. Piran, *Natural Explanation for the Anomalous Positron to Electron Ratio with Supernova Remnants as the Sole Cosmic Ray Source*, arXiv:0902.0376 (2009).

[Sta90] T. Stanev, *Astrophysical Sources of High Energy Neutrinos*, Nucl. Phys. **B** (14A), 17–27 (1990).

[Ste90] V. Stenger, *Track fitting for DUMAND-II Octagon Array*, External Report HDC-1-90, University of Hawai'i at Manoa, Manoa, HI, USA (1990).

[STY09] S. Shirai, F. Takahashi and T. Yanagida, *R-Violating Decay of Wino Dark Matter and Electron/Positron Excesses in the PAMELA/Fermi Experiments*, arXiv:0905.0388 (2009).

[Sup03] Super-Kamiokande Collaboration, *The Super-Kamiokande Detector*, Nucl. Instrum. Methods **A 501**, 418–462 (2003).

[Sup04] Super-Kamiokande Collaboration, *Search for Dark Matter WIMPs using Upward Through-going Muons in Super-Kamiokande*, Phys. Rev. **D 70**(083523) (2004), hep-ex/0404025.

[Sup08] Super-Kamiokande Collaboration, *Study of TeV Neutrinos with Upward Showering Muons in Super-Kamiokande*, Astropart. Phys. **29**, 42–54 (2008), arXiv:0711.0053v1 [hep-ex].

[Sup09] Super-Kamiokande Collaboration, *Search for Astrophysical Neutrino Point Sources at Super-Kamiokande*, Astrophys. J. **704**, 503–512 (2009), arXiv:0907.1594.

[Tib09] O. Tibolla et al. for the HESS Collaboration, *HESS J1741-302: a new source discovered in the Galactic Center region*, Am. Inst. of Phys. Conf. Proc. **1112**, 233–237 (2009).

[Til09] S. Tilav et al. for the IceCube Collaboration, *Atmospheric Variations as observed by IceCube*, Proceedings of the 31st ICRC, Lodz, Poland (2009), arXiv:1001.0776v2.

[Tos09] S. Toscano for the ANTARES Collaboration, *Point Source Searches with the ANTARES Neutrino Telescope*, Proceedings of the 31st ICRC conference, Lodz (2009), arXiv:0908.0864v1.

[VER08] VERITAS Collaboration, *VERITAS Observations of Extragalactic Non-Blazars*, Proceedings of 4th Heidelberg International Symposium on High Energy Gamma-Ray Astronomy (2008), arXiv:0810.1913v1 [astro-ph].

[Wie09] C. Wiebusch for the IceCube Collaboration, *Physics Capabilities of the IceCube DeepCore Detector*, Contribution to the 31st International Cosmic Ray Conference, Lodz, Poland (2009), arXiv:0907.2263.

[XEN04] XENON Collaboration, *The XENON Dark Matter Search Experiment*, New Astronomy Rev. **49**, 289–295 (2004), astro-ph/0407575.

[Y$^+$09] Q. Yuan et al., *Clumpiness Enhancement of Charged Cosmic Rays from Dark Matter Annihilation with Sommerfeld Effect*, arXiv:0905.2736 (2009).

[YKS08] H. Yuksel, M. Kistler and T. Stanev, *TeV Gamma Rays from Geminga and the Origin of the GeV Positron Excess*, arXiv:0810.2784 (2008).

[ZC07] J. Zornoza and D. Chirkin for the IceCube Collaboration, *Muon Energy Reconstruction and Atmospheric Neutrino Spectrum unfolding with the IceCube Detector*, Proceedings of the 30st ICRC, Merida, Mexico (2007).

[Zia00] H. Ziaeepour, *A Decaying Ultra Heavy Dark Matter (WIMPZILLA): Review of Recent Progress*, Grav. Cosmol. Suppl. (6), 128–133 (2000), arXiv:astro-ph/0005299v2.

[ZK66] G. Zatsepin and V. Kuz'min, *Upper Limit of the Spectrum of Cosmic Rays*, J. Exp. Theo. Phys. Lett. **4**, 78–80 (1966).